# Magnetic Reconnection in the Age of the Magnetospheric Multiscale Mission

by

#### Blake Alastair Wetherton

A dissertation submitted in partial fulfillment of the requirements for the degree of

Doctor of Philosophy

(Physics)

at the

UNIVERSITY OF WISCONSIN-MADISON

2020

Date of final oral examination: 08/28/2020

The dissertation is approved by the following members of the Final Oral Committee:

Jan Egedal, Professor, Physics Ellen Zweibel, Professor, Astronomy and Physics Stanislav Boldyrev, Professor, Physics

Carl Sovinec, Professor, Engineering Physics

To those who will read it.

#### ACKNOWLEDGMENTS

I would like to thank the Department of Energy and the Krell Institute for their support through the Computational Science Graduate Fellowship (Grant No. DE-FG02-97ER25308), which made graduate school significantly more enjoyable.

I would also like to thank my collaborators in various aspects of this work— foremost my advisor, Jan Egedal, who shared some excellent intuition and had no shortage of ideas for research. Bill Daughton was a great help in learning how to run simulations and pushing some through at the end. Ari Lê was also helpful on the computational side of things, and always had insightful comments on my paper drafts. Peter Montag was a great sounding board in developing the methods of Chapter 4, and helped to solidify much of the interpretation.

#### Contents

							•	٠	٠
C	$\cap$	n	t٠	$\alpha$ 1	nt	ŀC	1	1	1
•	•		u			Lo	ı		1

List of Tables v

List of Figures vi

#### Abstract xiii

- 1 Introduction 1
  - 1.1 Magnetic Reconnection Basics 1
  - 1.2 Historical Models of Magnetic Reconnection 4
  - 1.3 Anisotropic Model of Electron Dynamics in Magnetic Reconnection 11
  - 1.4 The Magnetospheric Multiscale Mission 21
  - 1.5 Outline of Thesis 24
- Validation of Anisotropic Electron Fluid Closure through *in situ*Spacecraft Observations of Magnetic Reconnection 26
  - 2.1 Introduction 26
  - 2.2 Basic Physics Governing Electron Pressure Anisotropy 27
  - 2.3 MMS Observations 30
  - 2.4 Comparison to Simulations 34
  - 2.5 Heating Predictions 36
  - 2.6 Discussion and Conclusions 39
- Anisotropic Electron Fluid Closure Validated by in situ Spacecraft
   Observations in the far Exhaust of Guide-Field Reconnection 40
  - 3.1 Introduction 40
  - 3.2 General Structure of Electric Fields and Plasma Density during Guide-Field Reconnection 44

- 3.3 Evidence of Magnetic Compression 49
- 3.4 Identifying Asymmetric Upstream Populations 55
- 3.5 Perpendicular Heating of Locally Trapped Electrons 60
- 3.6 Discussion and Conclusion 66
- 4 A Drift-Kinetic Method for Obtaining Gradients in Plasma Properties from Single-Point Measurements 69
  - 4.1 Introduction 69
  - 4.2 Apparent Agyrotropy of Simple Distributions that are Gyrotropic in the Guiding Center Frame 72
  - 4.3 Theoretical Basis for Length Scale Characterization 75
  - 4.4 PIC Verification of Length Scale Characterization 81
  - 4.5 Discussion and Conclusion 86
- 5 Conclusion 88
- A MMS Data Interpretation and Coordinate Systems 92
  - A.1 LMN Coordinates 92
  - A.2 Converting MMS Distributions to Field-Aligned Coordinates 93
- **B** Deriving the Boltzmann and CGL Limits 95
- C Intuitive Derivation of Gradients of Magnetized Distributions 98 Bibliography 100

## LIST OF TABLES

3.1	Upstream parameters corresponding to the three upstream	
	populations	56

8

10

#### LIST OF FIGURES

- 1.1 Diagram of Sweet-Parker reconnection. The shaded rectangle is the current carrying (into page) diffusion region of half length *L* and half width δ. The true aspect ratio would be much smaller
  1.2 Diagram of Petschek reconnection. The shaded rectangle is the
- current carrying (into page) diffusion region of half length L and half width  $\delta$ . Black lines represent slow shock fronts. . . .
- 1.3 Structure of the reconnection region for a typical antiparallel event. The ion flow decouples from the magnetic field in the ion diffusion/dissipation region, while the electrons stay frozen-in to the field down to the electron diffusion/dissipation region. The separation of the flows at this scale creates a current pattern that generates a characteristic quadrupolar magnetic field in the out-of-plane direction. Reproduced from Fig. 4 of Ref. [1].
- Illustration of an expanding flux tube. Each side of the distribution is fed by an upstream "half-Maxwellian" distribution. The distribution below the flux tube is representative of a location somewhere inside the tube, where the blue and red portions correspond to passing electrons originating from the corresponding upstream distributions. The green portion of the distribution represents electrons that are trapped by some combination of a magnitude of B that is depressed relative to the field strength at the ends of the flux tube and the parallel electric potential  $\phi_{||}$ . Figure reproduced from Fig. 3 of Ref. [2].

14

1.5	Four cases of the theoretical model distribution with a Maxwellian	
	upstream distribution. The form of the distribution function is	
	intimately related to the shape of the trapped-passing bound-	
	aries (black), which are determined by the parameters $\phi_{  }$ and	
	$B/B_{\infty}$ . Trapped portions of the distribution are shaded. $\phi_{  }$	
	determines the intersection of the trapped-passing boundaries	
	with the $v_{  }$ axis (or the closest approach thereof) and $B/B_{\infty}$	
	determines the opening angle of the trapped-passing bound-	
	aries. Note that in the case of $\phi_{  } < 0$ and $B > B_{\infty}$ , the entire	
	distribution is composed of passing electrons. In these figures,	
	$\phi_{  }=\pm T_e/e$ and $B/B_{\infty}=2^{\pm 1}.$	17
1.6	An illustration of the tetrahedral formation of MMS at the mag-	
	netopause and in the magnetotail. To compensate for the higher	
	density at the magnetopause (and thus smaller kinetic scales),	
	MMS flew in a tighter formation during the magnetopause	
	portion of the mission. Image credit: NASA	22
1.7	An illustration of the instrument suites mounted to MMS. Im-	
	age credit: NASA	23
2.1	a) Sample geometry of magnetic reconnection and the path	
	MMS3 took through the exhaust. Examples of typical trapped	
	and passing particle trajectories are drawn in. b) Magnetic field	
	traces that MMS3 measured along its trajectory. c), d), and	
	e) are the electron distribution functions measured by MMS3	
	at the points marked in a), which correspond to the inflow,	
	the density cavity, and the peak density in the exhaust. Black	
	contours represent the trapped-passing boundaries, and the	
	model distribution is to the right. The dashed theoretical con-	
	tours correspond to the same phase space density in all three	
	distributions	31

2.2	a) Electron parallel and perpendicular temperatures, plotted as	
	functions of the number density. These measurements recorded	
	by MMS3 are compared to Boltzmann, CGL, and the EoS scal-	
	ings. The data plotted correspond to the segment of time	
	marked by the red bars in b) and Fig. 2.1 b). b) Electron density	
	and temperatures measured by MMS3, with density normal-	
	ized to $n_0 = 8 \mathrm{cm}^{-3}$ and temperatures normalized to $T_0 = 34 \mathrm{eV}$ .	
		33
2.3	Density profile of the a) hybrid and b) fully-kinetic simulations.	
	c) Normalized electron density and temperatures from the hy-	
	brid simulation along the cut marked in a). d) Normalized	
	electron density and temperatures from the fully-kinetic mass	
	ratio 100 simulation along the cut marked in b)	36
2.4	Predictions for electron temperature gain across the reconnec-	
	tion layer by the EoS with an adiabatic ion closure. Note the	
	weak scaling relative to that laid out in [3]. This plot was pro-	
	duced assuming $T_{i\infty}/T_{e\infty}=10$ . The X roughly marks the tem-	
	perature gain observed in the $10/31/15$ event, where $B_g=1.75$	
	and $\beta_{er\infty}=0.085$ , while the observational scaling of Ref. [3] is	
	shown as a green dashed line.	38
3.1	a) The so-called direct acceleration potential $e\phi_y/T_e$ , integrating	
	the out-of-plane electric field along field lines whose in-plane	
	projections are shown in black. b) The in-plane electrostatic po-	
	tential $e\phi/T_e$ . c) The combined effect of these two components,	
	the parallel potential $e\phi_{\parallel}/T_e=e(\phi+\phi_y)/T_e$ , with an example	
	of an electron orbit in black. d) The electron density $n_e$ given by	
	the simulation. e) Estimate for the ion density given by Eq. 3.2,	
	based on the profiles of $\phi$ and $B$	45

3.2	Illustration of what the reconnection region could look like on	
	a global scale for Event B. The diagrams on the left roughly	
	correspond to the boxes drawn in the magnetosphere drawing.	
	In Event B, MMS encounters the reconnection outflow farther	
	from the $x$ -line than most kinetic simulations will include. We	
	believe this region is compressed relative to the unperturbed	
	upstream parameters, which occur even farther out. It is no-	
	table that this region is actively compressing during the transit	
	of a passing electron from the upstream distribution to the	
	observed location such that $\partial B/\partial t \neq 0$ . In contrast, Event A	
	occurred within the magnetosphere, and was not compressed	
	relative to the upstream parameters	50
3.3	How the flux tube evolves from its initial uniform state in a	
	typical reconnection scenario versus the effects of the compres-	
	sion on $B$ . In the compressing scenario, we seed the initial	
	profile of $B$ with several local dips, which can globally trap	
	particles in the initial scenario. As the magnetic field is com-	
	pressed, the magnetic field at the local minima rises above the	
	upstream field strength, allowing for particles to be locally, but	
	not globally, trapped	51

3.4	a) and g) Magnetic fields, b) and h) electron number density,	
	c) and i) electron temperatures measured by MMS crossing	
	the reconnecting layer. d) and j) show the variation of electron	
	parallel and perpendicular temperatures with $\tilde{n}/\tilde{B}$ in a region	
	between an electron density cavity (marked by the magenta	
	triangles) and peak (marked by the magenta circles), as well as	
	the predictions of the EoS in the dashed lines. e) and k) show	
	distributions measured in the density cavities, while f) and l)	
	show the distributions at the density peaks. Even in the density	
	cavity, the parallel potential for the $1/21/2016$ event remains	
	positive, which accounts for the increasing nature of the $T_{e\perp}$	
	curve in j)	54
3.5	MMS2 distributions from a) Inflow 1 and b) Inflow 2, as marked	
	in Fig. 3.6a), with the color scale set to emphasize the disconti-	
	nuity at the trapped-passing boundary	55
3.6	MMS2 measurements of a) density and magnetic field strength	
	b) $T_{e\parallel}$ and $T_{e\perp}$ for the three upstream regions in color vs the	
	EoS predictions in black. Magenta sections mark significant	
	departures from the EoS, which can be attributed to locally	
	trapped electrons. c) $\phi_{\parallel\pm}$ , the parallel potential inferred in each	
	direction along the magnetic field in blue and red, and the	
	potential difference between the two in black. d) and e) are	
	MMS2 (left) and the model of the EoS (right) electron distri-	
	bution functions at the points marked in a), which correspond	
	to the first inflow and the density cavity. Model contours and	
	black trapped-passing boundaries are superposed	57

3.7	a) MMS2 measurements of distinct characteristics in $(n^2/B^2,$	
	$T_{e\parallel}$ ) space for the two inflows and the exhaust. Black dashed	
	lines correspond to the prediction of the EoS for each branch,	
	while starred points are MMS2 measurements. b) The same	
	plots for $T_{e\perp}$ , with offsets for each exhaust to separate the data.	
	Magenta regions, as indicated in Fig. 3.6b), do not follow the	
	EoS due to heating by local trapping	60
3.8	Examples of flux tube evolution in a typical reconection sce-	
	nario and the compressing scenario. In the typical scenario, the	
	flux tube expands as it approaches the <i>x</i> -point, allowing for	
	electrons to become magnetically trapped in the global sense.	
	In the compressing case, we consider the initial flux tube to	
	be perturbed to have some portions expanded, again allowing	
	for magnetic trapping. As compression acts on the flux tube,	
	these regions are compressed relative to the upstream ends of	
	the flux tube, but remain local minima in the magnetic field	
	strength. As such, particles that were trapped in the initially	
	expanded regions may remained locally trapped, experiencing	
	perpendicular energization in the compression process	62
3.9	a-c) Electron distributions measured by MMS2 at times A, B,	
	and C marked in Fig. 3.6c), respectively. d) Electron distribu-	
	tion function predicted by Eq. 3.4 with $\Delta \mathcal{E} = 0$ at time C. e-f)	
	Inferred energy gain $\Delta \mathcal{E}/\mathcal{E}$ as a function of pitch angle and	
	energy for times A-C respectively	64
3.10	a-d) Inferred energization $\Delta \mathcal{E}/\mathcal{E}_{\perp}$ as a function of pitch angle	
	and time for various energy bins measured by MMS2. The	
	red and black contours represent the pitch angle at which an	
	electron will reflect in a magnetic field of $62\mathrm{nT}$ and $75\mathrm{nT}$ , re-	
	spectively	66

4.1	$A\mathcal{O}_e/2$ and $\sqrt{Q}$ plotted against the ratio of the Larmor scale to	
	the gradient scale, $\xi$ , for the relevant range	75
4.2	Illustration of how a single spacecraft sampling the electron	
	distribution can be applied for characterizing the gradient in	
	the gyrotropic electron distribution function $\nabla \bar{f}$	76
4.3	Normalized components of $\mathbf{\nabla}_{\!\!\perp} \log n$ for a simulation of antipar-	
	allel reconnection with $n_1/n_2=1.4$ through Eq. 4.23 and a	
	direct finite difference method. The dashed line represents the	
	cut taken in Figure 4.5a)	83
4.4	Normalized components of $\nabla_{\!\!\perp} \log p_{\perp}$ for a simulation of an-	
	tiparallel reconnection with $n_1/n_2=1.4$ through Eq. 4.24 and	
	a direct finite difference method. The color scale is slightly	
	saturated to emphasize the quality of the low amplitude match.	
	The dashed line represents the cut taken in Fig. 4.5a)	84
4.5	Cuts of normalized $N$ components of $\nabla_{\!\!\!\perp} \log n$ for simulations of	
	antiparallel reconnection with $n_1/n_2=1.4,7.8,$ and $16$ through	
	Eq.4.23 and a direct finite difference method	86

#### Abstract

Magnetic reconnection is a process that converts magnetic energy into kinetic energy in a plasma system through a change in topology of the magnetic field lines, and it allows explosive events such as coronal mass ejections and sawtooth crashes in magnetically-confined nuclear fusion experiments to occur. Reconnection mediates the transfer of solar wind plasma into Earth's magnetosphere. To learn more about the process of magnetic reconnection, NASA launched its Magnetospheric Multiscale (MMS) mission in 2015. In this thesis, we consider aspects of magnetic reconnection in relation to MMS observations and goals. We begin by further examining anisotropic equations of state (EoS) previously developed to describe the pressure parallel to and perpendicular to the local magnetic field. We find that the EoS holds near the *x*-line for an MMS event in the guide-field regime, and hybrid simulations (kinetic ions, fluid electrons with the EoS as a closure) are able to properly reproduce the MMS observations. We then apply the EoS to derive scalings of the electron bulk heating in the exhaust with upstream parameters. Afterwords, we examine another MMS event in the guide-field regime, this time much farther from the *x*-line, and show that the EoS also hold here. This event took place in a region of active compression, and we extend the model of the EoS to account for the energy gains from compression, showing that local electron trapping plays a role in additional perpendicular heating of the electrons. Finally, we present a drift-kinetic method that links agyrotropy, the lack of symmetry in the velocity space plane perpendicular to the magnetic field, to gradients in plasma properties. The method can predict gradients in fluid properties of the plasma based on a distribution function measured at a single spatial point, and could add significant utility to MMS observations.

### 1.1 Magnetic Reconnection Basics

Magnetic reconnection is a topological rearrangement of magnetic field lines in a plasma [1, 4]. The process is associated with explosive energy releases across a diverse and far-reaching set of plasma systems. From the scale of laboratory fusion experiments, where sawtooth crashes cause the loss of core confinement in tokamaks[5], to the astrophysical scale, where reconnection may play a role in  $\gamma$ -ray bursts[6], reconnection is ubiquitous. Reconnection is also crucial in our solar system, energizing solar flares and coronal mass ejections from the sun and moderating the interactions of the solar wind and Earth's magnetosphere. Reconnection was first proposed by Dungey [7] in 1953 as a source of high energy astrophysical particles, and it was also linked to solar flares and aurorae. In the past  $\sim 65$ years, many models and observations have refined our understanding of magnetic reconnection, but several crucial aspects of the process are still poorly understood. This is in no small part due to the innately kinetic nature of reconnection in collisionless plasma systems, such as are common in Earth's magnetosphere and the heliosphere.

Reconnection is remarkable, in part, because it is forbidden in ideal magnetohydrodynamics (MHD), the simplest reasonably comprehensive model of plasma behavior. Ideal MHD treats the plasma as a perfectly conducting fluid, then merges the fluid equations with a low-frequency approximation of Maxwell's equations (no displacement current) to model the system. Since the fluid conducts perfectly, in the frame of the fluid's bulk velocity there can be no electric field. This implies the condition that the magnetic flux is "frozen-in" to a fluid element and will convect with the bulk flow. Magnetic field lines are then tied to the fluid, and the magnetic topology is constant, as it cannot be altered by the continuous

deformations of the fluid; but real plasmas are not perfect conductors, and resistive or kinetic effects can allow the frozen-in condition to be broken in a localized sense. These local departures from the ideal MHD model can have profound consequences on the global dynamics.

A first question that reconnection studies look to answer is what is responsible for the breaking of the frozen-in condition for the electron fluid? Several options exist, including resistive effects, pressure tensor divergences, electron inertia, and anomalous resistivity from other kinetic effects. These can be encompassed in a Generalized Ohm's Law of the form

$$\mathbf{E} + \mathbf{v} \times \mathbf{B} = \eta \mathbf{j} + \frac{1}{ne} \left( \mathbf{j} \times \mathbf{B} - \nabla \cdot \mathbf{p}_e \right) + \frac{m_e}{ne^2} \frac{d\mathbf{j}}{dt} \quad , \tag{1.1}$$

where the terms on the right hand side of the equation represent departures from a perfectly conducting fluid. These can break the frozen-in condition, with the exception of the Hall term  $\mathbf{j} \times \mathbf{B}/ne$ , which cannot break the frozen-in condition for the electron fluid.

Analytical and numerical studies have uncovered the importance of other terms on the right hand side of Eq. 4.1. For example, the Geospace Environment Modeling (GEM) challenge has shown that the Hall-term and the related dispersive waves [8] play a key role in fast reconnection when the guide field is small, as will be discussed further in Section 1.2. In the presence of a guide magnetic field, not only the Hall term, but also effects related to the electron pressure tensor  $p_e$  are expected to be important [9], and indeed, they have been found to break the frozen-in law in MMS observations of the magnetotail [10]. In general, the pressure tensor is anisotropic and includes off-diagonal elements, which account for a finite plasma viscosity that can break the frozen-in condition for the electrons [11]. Pressure tensor effects become important at length scale characterized by the electron Larmor radius  $\rho$ . However, due to the complexity of the physics associated with a tensor pressure, much analytical work on magnetic reconnection relies on the simplifying assumption

that the pressure is isotropic and can be described by a scalar function. This is also the case for most numerical fluid simulations, although some theoretical work has included anisotropic pressures  $(p_{\parallel},p_{\perp})$  parallel and perpendicular to the magnetic field.

In studies including anisotropic pressure, the electron inertia term,  $(m_e/(ne^2))d\mathbf{j}/dt$ , can be important [12], including its convective component,  $\mathbf{v}\cdot\nabla$ , which can remain finite even in steady state [5]. This has been observed to be responsible for breaking the frozen-in condition on at the magnetopause in an MMS event [13]. In this case the characteristic length scale for the current profile is comparable to the electron skin depth  $c/\omega_{pe}$ . In many models this term is crucial in obtaining electron momentum balance at the x-line.

One aspect of interest is the reconnection rate, or how quickly flux is dissipated in reconnection. In a 2D context, the out-of-plane electric field at the x-line is also commonly referred to as the reconnection rate, as  $\partial A_y/\partial t=-E_y$ , where  $A_y$  is the flux function in an x-z slab regime. Often, the reconnection rate is reported in normalized form, which is generally quoted as the characteristic Alfvén crossing time divided by the characteristic time for flux dissipation. As will be discussed in Section 1.2, "fast" reconnection has a normalized reconnection rate on the order of  $10^{-1}$ , regardless of the mechanism responsible for breaking the frozen-in condition. This was not true of some early historical models.

Another important question in reconnection is how the magnetic energy gets transferred to other types of energy, and in what partition? Furthermore, can reconnection generate the power law tails of electron and ion distributions at high energies, and if so, how? These questions are all inherently kinetic and are active subjects of research, which now draws from fully-kinetic simulations, analytic theory, spacecraft observations of Earth's magnetosphere, and laboratory experiments. These tools are all available to us now, but when reconnection was first proposed, the

strongest tool available was MHD theory in relatively simple analytic configurations. In the next section, we will discuss the historical development of models of magnetic reconnection.

# 1.2 Historical Models of Magnetic Reconnection

Magnetic reconnection is, as mentioned, forbidden in ideal MHD through the frozen flux theorem. The simplest way to allow for magnetic field lines to break is by adding in some resistivity  $\eta$  to the plasma. If it is uniform, then we can derive the induction equation from Maxwell's equations (in the low frequency limit, dropping the displacement current) and the simple Ohm's law  $\mathbf{E} + \mathbf{v} \times \mathbf{B} = \eta \mathbf{j}$ . This leads to the magnetic induction equation

$$\frac{\partial \mathbf{B}}{\partial t} = \mathbf{\nabla} \times (\mathbf{v} \times \mathbf{B}) + \frac{\eta}{\mu_0} \nabla^2 \mathbf{B}$$
 (1.2)

which is frozen-in but for the resistive term. The magnetic diffusion has a characteristic time scale  $\tau_D = \mu_0 L^2/\eta$ , where L is the characteristic length scale of the gradient. It is useful to compare this to the propagation time of Alfvénic perturbations across the system. This leads to the Lundquist number  $S = \tau_D/\tau_A = \mu_0 v_A L/\eta$ . For a typical magnetized plasma,  $S \gg 1$ , meaning the effect of a uniform resistivity on breaking the frozen-in condition is minimal over the course of an Alfvén crossing time, and resistive diffusion alone cannot begin to describe the fast energy release observed in solar flares.

The first model that gives a meaningful reconnection process (much faster than the uniform resistive diffusion) is the Sweet-Parker model [14, 15]. The Sweet-Parker model gets around the long diffusive time by imagining a long, thin, resistive current layer separating two regions that are frozen-in to opposing fields. Figure 1.1 shows the basic setup of Sweet-

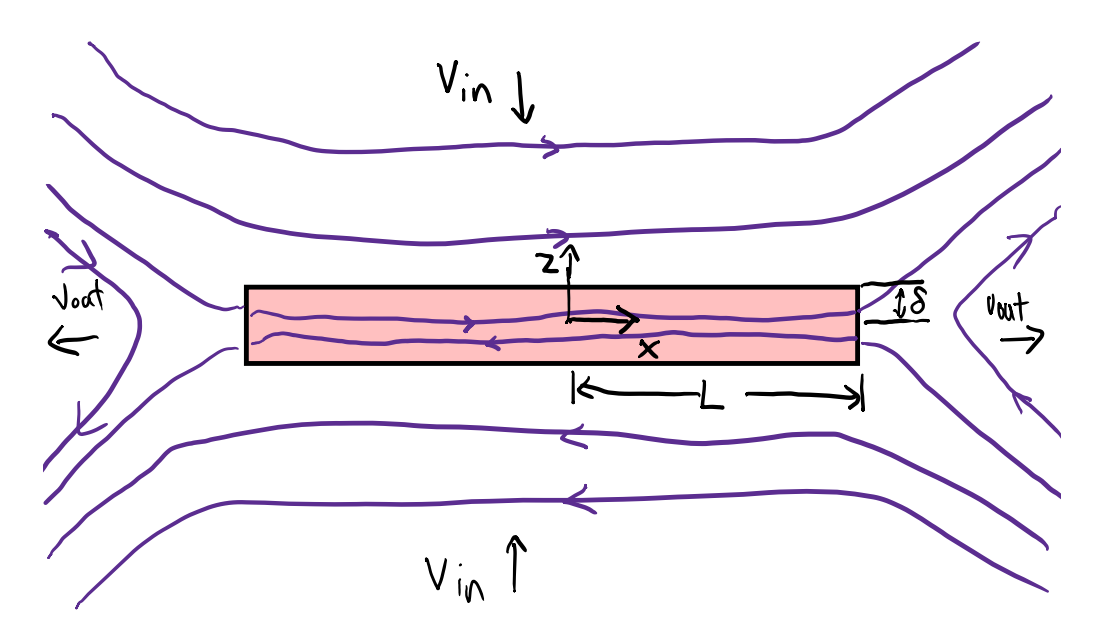


Figure 1.1: Diagram of Sweet-Parker reconnection. The shaded rectangle is the current carrying (into page) diffusion region of half length L and half width  $\delta$ . The true aspect ratio would be much smaller

Parker reconnection. The resistive layer is a rectangular region with half width  $\delta$  and half length L; this region carries a uniform current density j. On either side of the resistive layer, we find oppositely oriented magnetic fields of equal strength with inward flows at a constant velocity. To the left and right of the diffusion region, we find symmetric outflows at a constant speed, leading to a steady-state solution. The Sweet-Parker model also assumes the density in the inflow matches the density in the outflow.

The equations that must be solved in this model are the MHD continuity and momentum equations, along with Maxwell's equations in the MHD limit. First, we apply the integrated form of the continuity equation to the diffusion region.

$$\frac{\partial}{\partial t} n \delta L = 2L v_{\rm in} n - 2\delta v_{\rm out} n = 0 \implies \frac{v_{\rm in}}{v_{\rm out}} = \frac{\delta}{L}$$
 (1.3)

The next condition comes from Ampère's law. By drawing an Amperian loop around the perimeter of the diffusion region, it can be seen that

$$4LB_0 = 4\delta L\mu_0 j \implies j = \frac{B_0}{\mu_0 \delta}.$$
 (1.4)

Faraday's law provides another constraint. In steady-state,

$$\frac{\partial \mathbf{B}}{\partial t} = -\mathbf{\nabla} \times \mathbf{E} = 0. \tag{1.5}$$

The boundary between the diffusion region and upstream applies another condition. Since we do not allow variation in the out-of-plane direction, the curl-free condition on the electric field implies that the out of plane electric field is uniform in space. This means the electric field driving the current in the diffusion region is the same as the electric field driving the inflows via the  $\mathbf{E} \times \mathbf{B}$  drifts. As such,

$$E_{\rm rec} = \eta j = v_{\rm in} B_0. \tag{1.6}$$

We next look at MHD force balance in both in-plane directions. First, we can look at force balance in the z-direction along the line x=0. We neglect the fluid inertial term in the inflow, as we expect the kinetic energy in the bulk inflow to be small compared to the magnetic energy being dissipated. Force balance becomes

$$\frac{\partial}{\partial z}(p + \frac{B^2}{2\mu_0}) = 0 \implies p_{\text{max}} = p_0 + \frac{B_0^2}{2\mu_0}, \tag{1.7}$$

where  $p_0$  is the pressure far upstream and  $p_{\text{max}}$  is the maximum pressure, which is attained at the origin. A similar condition applies along the line z=0, except the magnetic field has been depleted here and we allow for

considerable inertia in the outflow.

$$\frac{\partial}{\partial x}(p + \frac{1}{2}\rho v_x^2) = 0 \implies p_0 + \frac{1}{2}\rho v_{out}^2 = p_{\text{max}}$$
 (1.8)

Combining Equations 1.7 and 1.8, we find that

$$v_{\text{out}} = \frac{B_0}{\sqrt{\mu_0 \rho}} = v_A, \tag{1.9}$$

meaning the outflow velocity is the upstream Alfvén velocity. This allows for the full solution of the problem. By combining the results of Equations 1.3, 1.4, 1.6, 1.9, and the definition of the Lundquist number above, we find

$$\frac{\delta}{L} = \frac{v_{\rm in}}{v_A} = S^{-1/2},$$
 (1.10)

meaning that  $\delta \ll L$  in the typical regime of  $S \gg 1$ , and the Sweet Parker reconnection time is the geometric mean of the diffusive and Alfvén times. While this is not as dismal as the diffusive rate that scales as  $S^{-1}$ , it is still not sufficient to explain the fast evolution of solar flares, coronal mass ejections, and sawtooth reconnection in fusion experiments. For the solar flare problem, the diffusive time scale is on the order of years. For the Sweet-Parker model, that can reduce to months. Reconnection in solar flares takes place on the order of tens of minutes.

The first model to provide truly fast reconnection was the model by Petschek [16], which applies slow shocks to the reconnection region to help speed up the process. The shock fronts allow for a much shorter current layer, meaning a larger opening angle in the exhaust, which eases the continuity constraint.

Petschek's model gives a maximum reconnection rate of

$$\frac{v_{\rm in}}{v_{\rm out}} \approx \frac{\pi}{8 \ln S},$$
 (1.11)

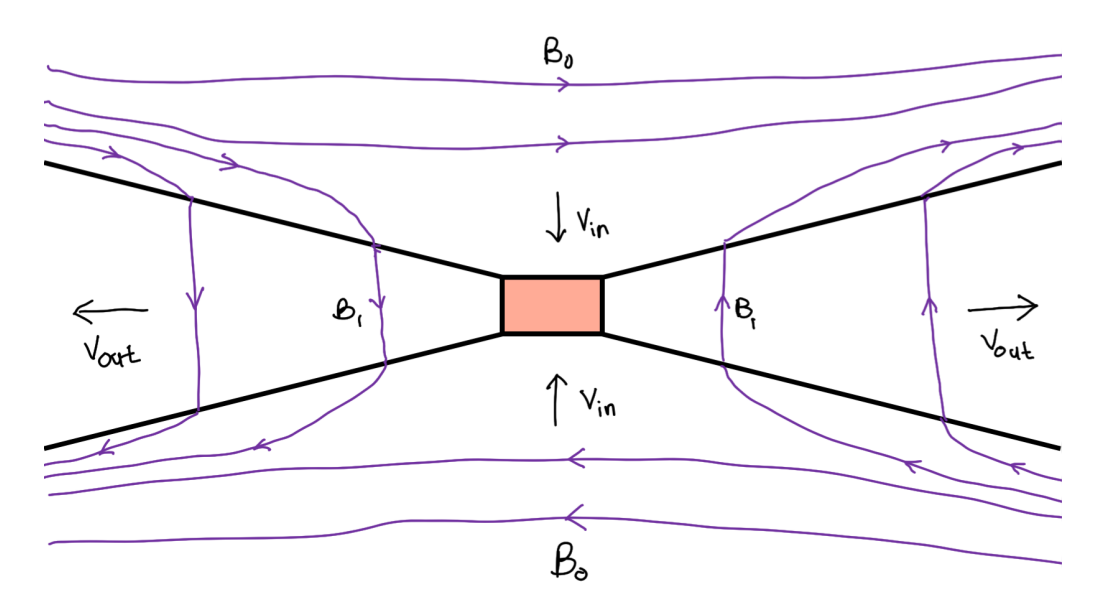


Figure 1.2: Diagram of Petschek reconnection. The shaded rectangle is the current carrying (into page) diffusion region of half length L and half width  $\delta$ . Black lines represent slow shock fronts.

which is nearly independent of Lundquist number, allowing for appreciable reconnection rates in realistic naturally-occurring reconnection conditions with  $S\gg 1$ . This made the Petschek model a promising one for explaining solar flares.

While the Petschek model predicts fast reconnection, the associated shocks are not observed in experiments or simulations of realistic natural reconnection configurations. MHD simulations with localized anomolous resistivity are able to reproduce the Petschek solution, but there is little physical justification for this ever occurring naturally. It is notable, however, that as computational models have advanced in the field, fast reconnection is frequently seen. Fully-kinetic simulations of collisionless (or weakly collisional) magnetic reconnection display uniformly fast reconnection rates, meaning that some physics included in fully-kinetic models but not in standard resistive MHD is responsible for fast reconnection.

The minimum requirements for fast reconnection were the subject of the Geospace Environment Modeling (GEM) Reconnection Challenge, which was completed in 2001 through a synthesized analysis from a number of teams [8]. By simulating a symmetric 2D Harris sheet under a variety of models (including fully-kinetic models [17–19], hybrid models with and without electron mass and off-diagonal pressure elements [19, 20], Hall MHD models with and without electron mass [19, 21–23], and non-Hall MHD models [17, 22]), it was found that if resistive effects were sufficiently small and/or sufficiently localized, all models that included the Hall term in Ohm's law led to nearly-identical fast reconnection rates. The Hall term alone is not capable of breaking the electron frozen-in condition, but it does set a fast reconnection rate regardless of the specific mechanism that actually breaks the electron frozen-in condition.

How does the Hall term allow for fast reconnection? As the width of the current layer drops below the ion kinetic scale (the maximum of  $d_i=c/\omega_{pi}$  and  $\rho_i=v_{thi}/\Omega_{ci}$ ), the ions and electrons decouple. In the sense of Sweet-Parker scalings, this happens when the electron collision length is smaller than the length of the current sheet.

The ions are thought to be unmagnetized at the length scale of the ion skin depth  $c/\omega_{pi}$ , while the electrons are magnetized down to the electron skin depth  $c/\omega_{pe}$ . As such, the reconnecting flux pulls the electrons in closer to the X-line than the ions, creating a separation of flows. The differing electron and ion flow patterns at this scale comprise the so-called Hall currents, which create a characteristic quadrupolar magnetic field structure, as is illustrated in Figure 1.3. Due to the dispersion relation of the reconnecting mode near the X-line, the reconnection rate becomes insensitive to the mechanism that is actually responsible for breaking the frozen-in law [19]. The characteristic Hall magnetic fields have been observed at the magnetopause [24], in the near-Earth region of the magnetotail [25–27], and also in the deep magnetotail [28].

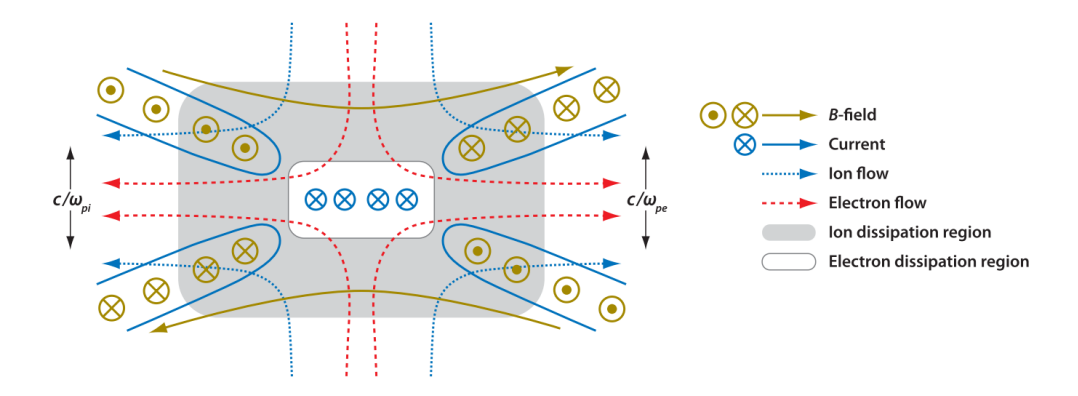


Figure 1.3: Structure of the reconnection region for a typical antiparallel event. The ion flow decouples from the magnetic field in the ion diffusion/dissipation region, while the electrons stay frozen-in to the field down to the electron diffusion/dissipation region. The separation of the flows at this scale creates a current pattern that generates a characteristic quadrupolar magnetic field in the out-of-plane direction. Reproduced from Fig. 4 of Ref. [1].

More recent work in reconnection has shown that fast reconnection can be attained even in MHD regimes through the plasmoid instability [29, 30]. This is an MHD instability associated with long Sweet-Parker current layers that causes the layer to break up into a chain of magnetic islands or "plasmoids" along the layer. This instability can form secondary reconnection layers that will in turn fall victim to the plasmoid instability, leading to fast reconnection in the MHD regime. However, in this scheme, the current layers will eventually reach the kinetic scale, at which point fast reconnection proceeds anyway in a physical system [31].

# 1.3 Anisotropic Model of Electron Dynamics in Magnetic Reconnection

In contrast to solid conductors, plasmas are remarkable in that their electrical conductivity increases with increasing temperature. The hot fusion plasmas that have driven the development of plasma physics as a discipline are very good conductors, preventing magnetic diffusion and allowing the frozen-in condition to apply almost everywhere. Although collisions are infrequent enough to keep the magnetic field well frozen-in, fusion plasmas still tend to have collision times that are much shorter than typical dynamical times, such that the electron distributions are isotropic and nearly Maxwellian. Even relatively small collision frequencies can significantly alter the kinetic structure of reconnection [32]. This is not the case in many space plasmas, which have much longer collision times thanks to their reduced density. In fact, an electron in the solar wind will typically travel an order unity fraction of the distance from the sun to the Earth  $(\sim 1 \text{ AU})$  before experiencing a collision. For dynamic systems like Earth's magnetosphere, which are small in comparison to the collision length, this makes the plasma truly collisionless, and the electron distribution function need not maintain isotropy. This section will cover the anisotropic electron model that will be used extensively in this thesis, largely following Ref. [2].

In a truly collisionless plasma system, the kinetic equation is Hamiltonian, and therefore Liouville's theorem [33] applies, meaning the distribution function is constant along characteristic trajectories. This allows for a model to connect the distribution function at a certain location to some upstream distribution through the characteristic particle trajectories. To do this, it is most useful to move to a reduced model that incorporates some common assumptions about the plasma; in this case, the drift kinetic model is an appropriate level of reduction. Drift kinetics assumes that the particles are well-magnetized, and we can ignore the fast gyroorbit about

the magnetic field lines. Consequently, this encodes the conservation of the first adiabatic invariant magnetic moment  $\mu=mv_{\perp}^2/2B$ , and reduces the perpendicular dynamics to those of the drift velocity. For the electrons, the drift kinetic equation is

$$\frac{\partial \bar{f}}{\partial t} + (\mathbf{v}_{||} + \mathbf{v}_{D}) \cdot \nabla \bar{f} + \left[ \mu \frac{\partial B}{\partial t} - e \left( \mathbf{v}_{||} + \mathbf{v}_{D} \right) \cdot \mathbf{E} \right] \frac{\partial \bar{f}}{\partial \mathcal{E}} = 0, \quad (1.12)$$

where  $\mathcal{E}=m(v_{||}^2+v_{\perp}^2)/2$  is the kinetic energy of the electron,  $\bar{f}$  is the gyroaveraged distribution function, and

$$\mathbf{v}_{D} = \frac{\mathbf{E} \times \mathbf{B}}{B^{2}} - \frac{mv_{\perp}^{2}}{2eB}\mathbf{b} \times \nabla B - \frac{mv_{\parallel}^{2}}{eB}\mathbf{b} \times \kappa$$
 (1.13)

is the guiding center drift, with the unit vector  $\mathbf{b} = \mathbf{B}/B$  aligned with the magnetic field and the curvature vector  $\boldsymbol{\kappa} = (\mathbf{b} \cdot \boldsymbol{\nabla})\mathbf{b}$ . The guiding center orbits of electrons are the characteristics of this equation, along which  $\bar{f}$  is constant. Some fraction of the guiding center orbits may be trapped in the magnetic geometry, while other orbits pass along field lines without changing the direction travelled along a field line. The distinction between these two types of orbits will be crucial to describing the dynamics of magnetic reconnection.

Particles trapped in slowly changing fields are fundamentally characterized by their first two adiabatic invariants— the magnetic moment  $\mu=mv_\perp^2/2B$  corresponding to the gyromotion, and the action integral  $J=\oint v_{||}\mathrm{d}l$  corresponding to the bounce motion. With orbits fully characterized by these two quantities [34–37], it follows that the distribution function can be written as  $\bar{f}=g(\mu,J)$ , which can be an arbitrary function matching the appropriate boundary conditions. Generally, when the reconnection region is approached, B decreases. To conserve  $\mu$ ,  $v_\perp$  must also decrease. At the same time, bounce orbit lengths tend to decrease,

which requires  $v_{\parallel}$  to increase to conserve J. As such, in the limit of a fully-trapped distribution, such as existed in an infinite cusp configuration for reconnection experiments on the Versitile Toroidal Facility (VTF) [35, 38], strong anisotropy favoring the parallel temperature develops.

In general reconnection scenarios, the magnetic field strength does not decrease so much near the reconnection region that all electrons become trapped. Early Wind spacecraft measurements of electron distribution functions during reconnection in Earth's magnetotail revealed strongly anisotropic features [28]. The magnetic trapping model used on VTF worked well to describe the distribution of higher energy electrons, but in order to properly match at lower energies, an acceleration potential  $\phi_{\parallel} = \int_x^{\infty} E_{\parallel} \mathrm{d}l$  needed to be invoked [39]. Strictly speaking, this is a pseudopotential, as it includes inductive components of the electric field, though it represents the fields experienced during a particle orbit well. This acceleration potential added additional electric trapping, which is independent of energy. For the Wind event, the acceleration potential was nontrivial and much larger than expected  $e\phi_{\parallel} \simeq 3T_e$ . As such, a proper model for reconnection must account for both electric and magnetic trapping effects while allowing for untrapped "passing" particles.

The model can be divided between trapped and passing cases in a 1D flux tube model. Figure 1.4 shows the basic division of the model, with the flux tube fed by upstream distributions from either side of the parallel direction, and trapped particles existing between them. Under the limit of fast electron transit time for passing particles, the lowest order terms of Eq. 1.12 yield

$$\mathbf{v}_{\parallel} \cdot \mathbf{\nabla} \bar{f}_0 - e \left( \mathbf{v}_{\parallel} \cdot \mathbf{E} \right) \frac{\partial \bar{f}_0}{\partial \mathcal{E}} = 0$$
 (1.14)

By integrating along the characteristic orbit (this is the magnetic field line in the drift-kinetic limit), a solution for passing electrons is obtained.

$$\bar{f}_0(\mathcal{E}_{\parallel}, \mathcal{E}_{\perp}) = \bar{f}_{\infty}(\mathcal{E} - e\phi_{\parallel}^{\pm} - \mu B_{\infty}, \mu B_{\infty})$$
(1.15)

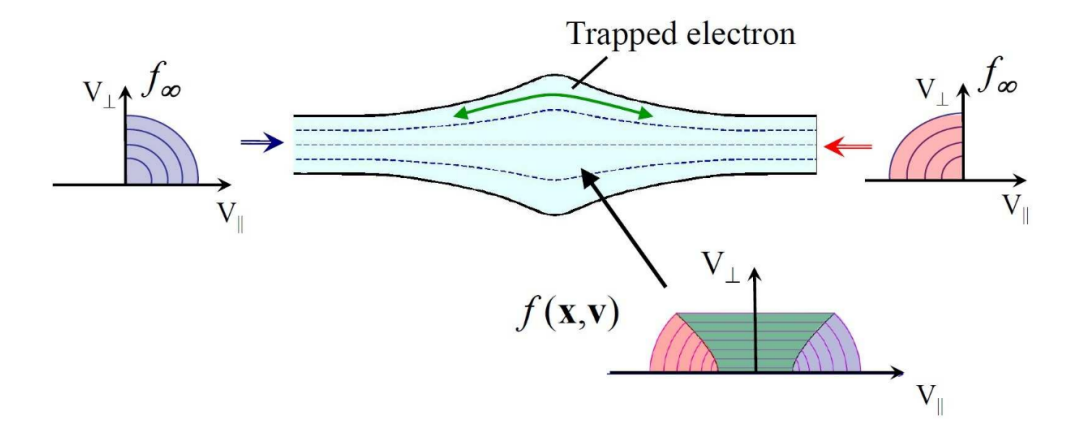


Figure 1.4: Illustration of an expanding flux tube. Each side of the distribution is fed by an upstream "half-Maxwellian" distribution. The distribution below the flux tube is representative of a location somewhere inside the tube, where the blue and red portions correspond to passing electrons originating from the corresponding upstream distributions. The green portion of the distribution represents electrons that are trapped by some combination of a magnitude of B that is depressed relative to the field strength at the ends of the flux tube and the parallel electric potential  $\phi_{||}$ . Figure reproduced from Fig. 3 of Ref. [2].

with  $\phi_{\parallel}^{\pm}=\int_{x}^{\pm\infty}E_{\parallel}\mathrm{d}l$  corresponding to the acceleration potential to either end of the flux tube. The boundary between trapped and passing particles is defined by  $\mathcal{E}-e\phi_{\parallel}^{\pm}-\mu B_{\infty}=0$ , meaning that a marginally trapped electron will deplete its energy exactly at the end of the flux tube.

Trapped electrons are confined long enough that no terms are negligible in Eq. 1.12; however, as mentioned earlier, the trapped trajectories are fully defined by their adiabatic invariants, and as such  $\bar{f}_0 = g(\mu, J)$  for the trapped portion of phase space. As such, it is only needed to find a  $g(\mu, J)$  that satisfies the boundary conditions at the ends of the flux tube for marginally trapped particles, i.e.  $g(\mu, J) = \bar{f}_{\infty} \left( \mathcal{E}_{\parallel \infty}(\mu, J), \mathcal{E}_{\perp \infty}(\mu, J) \right)$  corresponding to the energies at which the trapped electrons entered the flux tube.

By conservation of the magnetic moment,  $\mathcal{E}_{\perp\infty}(\mu,J)=\mu B_{\infty}$ . Exact calculation of  $\mathcal{E}_{\parallel\infty}$  requires knowledge of the electric and magnetic geometry; however, to become trapped, the particle must have a flux tube transit time at least comparable to the development time of the electric and magnetic wells, which develop slowly compared to the thermal transit of the flux tube. As such, it is useful to approximate the electrons as having no parallel energy at the ends of the flux tube. This leads to the trapped solution

$$\bar{f}_0(\mathcal{E}_{\parallel}, \mathcal{E}_{\perp}) = \bar{f}_{\infty}(\mathcal{E}_{\parallel \infty}, \mathcal{E}_{\perp \infty}) = \bar{f}_{\infty}(0, \mu B_{\infty})$$
 (1.16)

Combining the trapped and passing populations, we arrive at the full description of the distribution function

$$\bar{f}(\mathcal{E}_{||}, \mathcal{E}_{\perp}) = \begin{cases} \bar{f}_{\infty}(0, \mu B_{\infty}) & \text{trapped} \\ \bar{f}_{\infty}(\mathcal{E} - e\phi_{||} - \mu B_{\infty}, \mu B_{\infty}) & \text{passing.} \end{cases}$$
(1.17)

This model has inputs of the upstream distribution function, the parallel potential  $\phi_{||}$ , and the upstream magnetic field strength. The simplest case models the upstream distribution as an isotropic Maxwellian with density  $n_{\infty}$  and temperature  $T_e$ . With these constraints, there are four distinct regimes based on the sign of the parallel potential  $\phi_{||}$  and the strength of the local magnetic field B relative to the upstream value  $B_{\infty}$ . These parameters determine the shape of the trapped-passing (TP) boundary, which accounts for most of the interesting features of the model. The TP boundary is described by the curve where  $\mathcal{E}_{||\infty} = \mathcal{E} - e\phi_{||} - \mu B_{\infty} = 0$ , where positive values are passing and negative values are trapped. Figure 1.5 shows contours of sample distributions for each case.

Near the x-line in the 2D picture of reconnection, the in plane magnetic field goes to zero, while the guide field tends not to increase by an

appreciable fraction of the reconnecting field. This means that near the current sheet, we will typically expect to see cases where  $B < B_{\infty}$ , and magnetic trapping will play a significant role in the electron dynamics. As it turns out, electrons tend to also be electrically trapped with  $\phi_{||} > 0$ in reconnection inflows, producing two passing populations shifted by the parallel potential and a large trapped region dividing the two passing populations. The trapped-passing boundary is a hyperbola with foci on the  $v_{||}$ -axis. If  $\phi_{||} < 0$ , magnetic trapping still effects particles with pitch angles near 90°, but the two inflows are no longer separated. The trappedpassing boundary is now a half hyperbola with foci on the  $v_{\perp}$ -axis. The case with  $B > B_{\infty}$  is less common in reconnection scenarios, but we will see that it is occasionally relevant in Chapter 3. For the case with  $\phi_{||} > 0$ and  $B > B_{\infty}$ , the trapped region is a bounded semi-ellipse surrounded by the passing region. In the final case,  $\phi_{||}<0$  and  $B>B_{\infty}$  , no trapping is allowed, and the resulting distribution function is purely passing particles shifted by the parallel potential from the upstream.

Since constant contours of the distribution function are horizontal lines in the trapped portions of phase space, the trapped region will always contribute more to  $p_{||}$  than it will to  $p_{\perp}$ . Meanwhile, the passing portions of the distribution reflect the isotropy of the upstream distribution. As such, larger trapped regions imply stronger pressure anisotropy  $p_{||}/p_{\perp}$ , with  $p_{||}/p_{\perp} \geq 1$  for an isotropic upstream distribution. As such, the typical case of both electric and magnetic trapping will produce the most strongly anisotropic distributions, while the case with no trapping will result in completely isotropic distributions.

With an analytic solution to the distribution function for any given the upstream distribution, the parallel potential, and the ratio of the local magnetic field strength to the upstream magnetic field, moments can be taken to gain insight into the fluid properties of the plasma in this model. For simplicity, we tend to model the upstream distribution as either

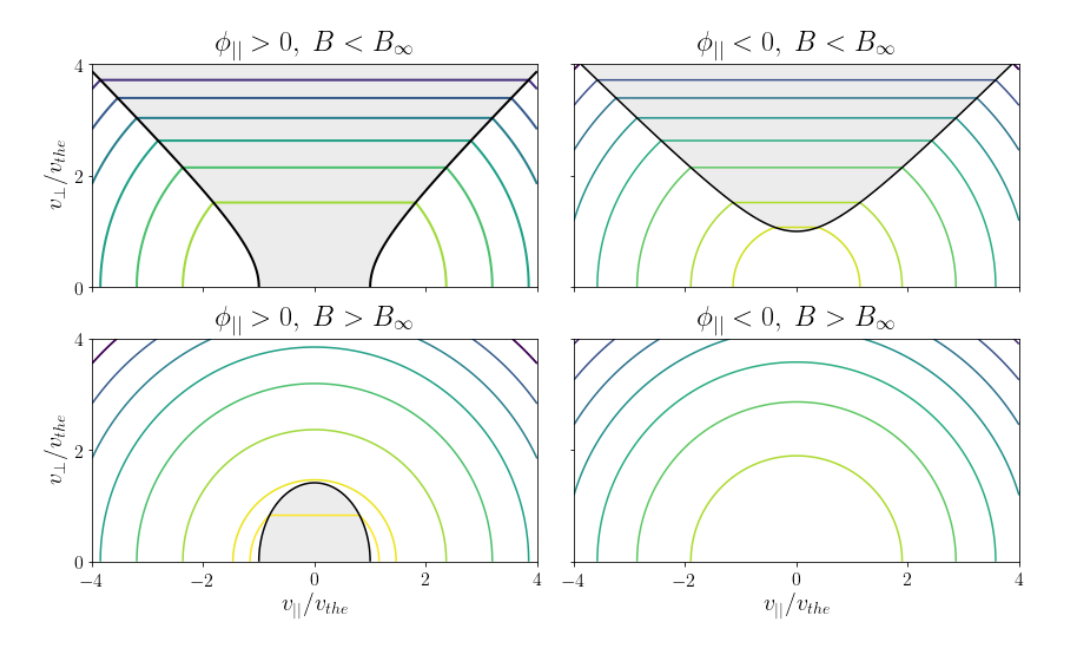


Figure 1.5: Four cases of the theoretical model distribution with a Maxwellian upstream distribution. The form of the distribution function is intimately related to the shape of the trapped-passing boundaries (black), which are determined by the parameters  $\phi_{||}$  and  $B/B_{\infty}$ . Trapped portions of the distribution are shaded.  $\phi_{||}$  determines the intersection of the trapped-passing boundaries with the  $v_{||}$  axis (or the closest approach thereof) and  $B/B_{\infty}$  determines the opening angle of the trapped-passing boundaries. Note that in the case of  $\phi_{||}<0$  and  $B>B_{\infty}$ , the entire distribution is composed of passing electrons. In these figures,  $\phi_{||}=\pm T_e/e$  and  $B/B_{\infty}=2^{\pm 1}$ .

an isotropic Maxwellian, or a bi-Maxwellian with separate parallel and perpendicular temperatures, but this is not a requirement of the model.

For any upstream distribution function that decreases monotonically in both parallel and perpendicular energy, the partial derivative of the phase space density with respect to  $\phi_{||}$  is positive in passing regions and zero in trapped regions. At the TP boundary, increasing  $\phi_{||}$  will expand the trapped region, and trapped electrons at any given  $\mu$  have higher phase space density than passing particles with the same  $\mu$  value. Since there are always portions of phase space which are passing, at a given value of  $B/B_{\infty}$ , every purely even moment of the distribution function is continuous and strictly increasing in  $\phi_{||}$  (the moments that are odd in any of the three orthogonal velocities are zero with the assumed symmetry), and all tend toward 0 and  $\infty$  as  $\phi_{||} \to \mp \infty$ , respectively. As such, there exist bijective mappings  $g_{2k,2l,2m}: \mathbb{R} \to (0,\infty)$  for  $k,l,m \in \mathbb{N}_0$  such that  $g_{2k,2l,2m}(\phi_{||})$  is the moment  $\int v_{||}^{2k} v_{\perp 1}^{2l} v_{\perp 2}^{2m} f d^3v$ . As these mappings are bijective, any purely even moment of the distribution function can in principle be inverted to find the parallel potential. This is most useful with the density.

Solving for the parallel and perpendicular pressures in terms of the local density and magnetic field relative to their upstream values gives equations of state (EoS, these specifically will be referred to as "the EoS") which give insight into the behavior of the plasma and can potentially provide a closure for fluid treatments of the electrons. While analytic forms of the EoS do exist for the isotropic Maxwellian upstream case [40], they involve hypergeometric functions and are costly to compute without providing much intuitive value. In practice, it is easier to do the inversion numerically to calculate equations of state. Through this procedure, the EoS were verified to hold in fully-kinetic simulations of magnetic reconnection [41].

In the context of simulating a fluid species, calculating the EoS through

numerical inversion is expensive, so it may be desirable to have a reduced model that approximates the EoS at lower cost. An approximate fit of the EoS for typical reconnection parameters is given in [41], which interpolates the asymptotic limits of the model. This fit is given by

$$\tilde{p}_{||} = \tilde{n} \frac{2}{2+\alpha} + \frac{\pi \tilde{n}^3}{6\tilde{B}^2} \frac{2\alpha}{2\alpha+1}$$
 (1.18)

$$\tilde{p}_{\perp} = \tilde{n} \frac{1}{1+\alpha} + \tilde{n} \tilde{B} \frac{\alpha}{\alpha+1} \tag{1.19}$$

where for a local quantity Q,  $\tilde{Q}=Q/Q_{\infty}$  with  $Q_{\infty}$  the "upstream" value at the end of the flux tube and  $\alpha=\tilde{n}^3/\tilde{B}^2$ . In the small  $\alpha$  limit,  $\tilde{p}_{||}$  and  $\tilde{p}_{\perp}$  both scale as  $\tilde{n}$ . This is an isotropic isothermal limit, which is the Boltzmann limit of particles working against a potential. In the large  $\alpha$  limit,  $\tilde{p}_{||}$  scales as  $\tilde{n}^3/\tilde{B}^2$  and  $\tilde{p}_{\perp}$  scales as  $\tilde{n}\tilde{B}$ , which corresponds to the double adiabatic Chew-Goldberger-Low (CGL) model [42], which is intended to model trapped particles conserving their first two adiabatic invariants. The EoS incorporates both limits, roughly mediated by the fraction of particles that are trapped.

Eqs. 1.18-1.19 have been implemented as an electron closure in two-fluid simulations of magnetic reconnection [43] in the HiFi multi-fluid modeling framework[44]. Aside from the EoS as the electron closure, the simulations use an adiabatic ion closure and compressible flows. Hyper-resistivity allows for the frozen-in condition to be broken, and the addition of ion viscosity and thermal conductivity provides numerical stability. The simulations were compared to equivalent simulations using an isotropic isothermal electron closure. The anisotropic closure was able to reproduce some aspects of fully-kinetic simulations that the isotropic closure could not. In particular, the extended embedded current layers that mark Regime 3 of Ref. [45] were seen with the anisotropic closure, but not the isotropic one. These extended current layers form where the marginal electron firehose condition is approached, i.e.  $\mu_0(p_{e\perp}-p_{e\parallel})/B^2\sim 1$ . Clearly, this

limit cannot be approached in the context of an isotropic electron closure, as the firehose condition is identically zero.

Likewise, the closure has been successfully implemented [46] in the H3D[47] hybrid framework, which treats the electrons as a fluid and the ions kinetically through the particle-in-cell (PIC) method. Similarly to the two fluid results, the extended current sheet developed with the anisotropic closure, but not with an isotropic isothermal closure. This allows for an intermediate level of modeling that retains full ion kinetic effects, while not requiring the costly resolution of the electron kinetic scale.

Beyond computational considerations, this anisotropic EoS can be applied to better understand the bulk heating of electrons in the magnetic reconnection exhaust. Observational evidence has suggested that the temperature gain in the reconnection exhaust scales as  $\Delta T_e \sim m_i v_A^2$  [3], where the Alfvén speed is based on the reconnecting component of the magnetic field only. A theoretical scaling consistent with the observational data can be derived through the anisotropic EoS in the weak to intermediate guide-field regime [48]. The crucial elements of the analysis are the EoS, force balance across a steady-state reconnection layer, an adiabatic ion closure, and the assumption that the minimal magnetic field point in the exhaust (where density and electron temperatures will be maximal by force balance and the EoS) is regulated by the marginal electron firehose condition. This creates a system of four equations with the same number of unknowns, which can be solved numerically and shown to be consistent with the observational data. The bulk heating of electrons during reconnection is encoded in the dynamics leading to the EoS.

### 1.4 The Magnetospheric Multiscale Mission

NASA launched the Magnetospheric Multiscale (MMS) mission on March 12, 2015, with the goal of studying magnetic reconnection in Earth's magnetosphere in more detail than ever before possible. MMS is composed of four spacecraft that orbit Earth in a tetrahedral formation, each independently measuring electric and magnetic fields and full distribution functions for ions and electrons. The formation was originally set to orbit such that it would pass through the magnetopause to observe dayside reconnection, and has since had its orbit adjusted to observe reconnection in the nightside magnetotail. When passing through a reconnection region, MMS can go into "burst mode," where data is taken at a faster cadence, with electron distributions recorded every 30 ms and ion distributions every 150 ms, allowing for the evolution of the distribution function to be observed in detail as the reconnection layer is crossed [49]. Moreover, the spacecraft separation is typically approximately 10 km for the dayside campaign and  $100 \,\mathrm{km}$  for the tail campaign, as the lower density of the tail lengthens the ion and electron skin depths which correspond to the kinetic scales of reconnection. For the dayside, this represents about  $10 d_e$ , which is smaller than the ion kinetic scale, allowing for some spatial data relating to local gradients. A basic illustration of the MMS formation is shown in Figure 1.6, noting that the tetrahedral side length is adjusted according to the mission phase. It should be noted that the  $\sim 10 \, \mathrm{km}$  spacing of MMS during the dayside campaign is a remarkable technical achievement in itself, and in 2016 the MMS tetrahedron became the tightest formation ever flown by multiple spacecraft.

Generally speaking, the MMS data I will be analyzing in this thesis will come from two of the five SMART instrument suites with which MMS is equipped, the layout of which is shown in Figure 1.7. The FIELDS [50] suite measures electric and magnetic fields. Electric field measurements come from the DC electric field measured by the Electric field Double

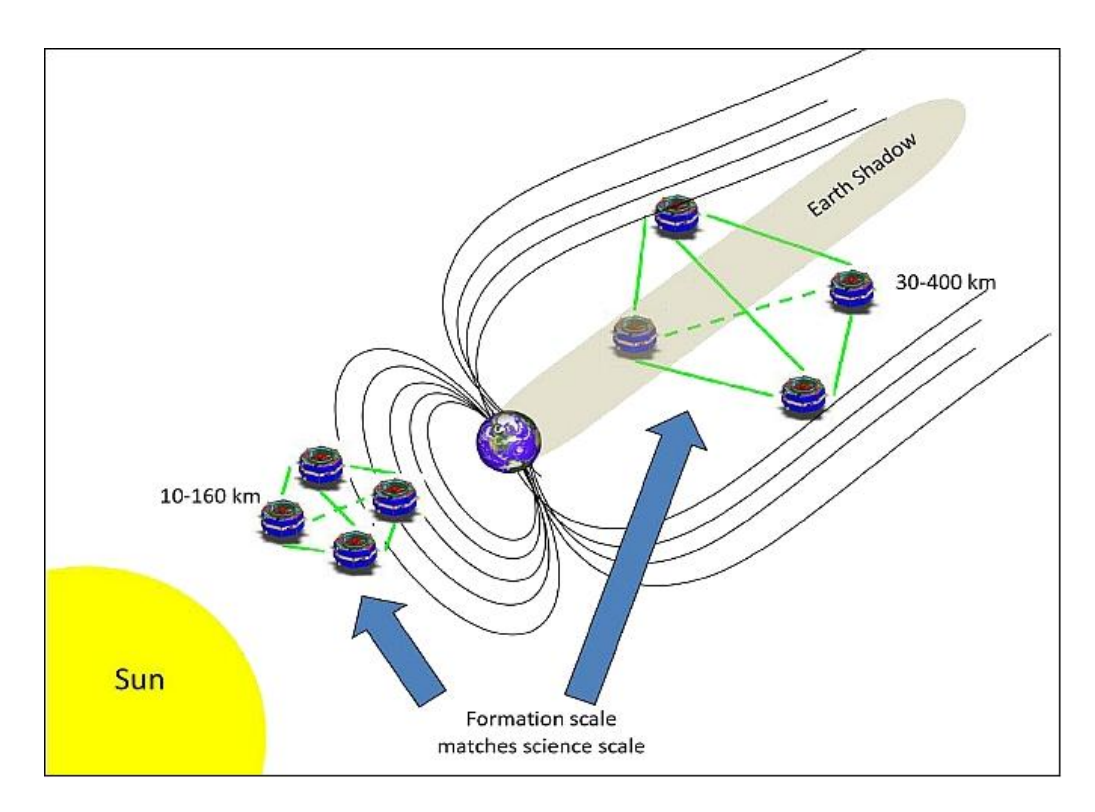


Figure 1.6: An illustration of the tetrahedral formation of MMS at the magnetopause and in the magnetotail. To compensate for the higher density at the magnetopause (and thus smaller kinetic scales), MMS flew in a tighter formation during the magnetopause portion of the mission. Image credit: NASA.

Probe (EDP) instrument. Magnetic field measurements come from the Flux Gate Magnetometer (FGM) instrument, which measures the magnetic flux on three orthogonal axes. Distribution functions come from the Fast Plasma Investigastion (FPI) [49], which consists of four dual electron spectrometers (DES) and four dual ion spectrometers (DIS) per spacecraft. Each can measure the corresponding particle distribution in exponentially spaced energy bins from  $10\,\mathrm{eV}$  to  $30\,\mathrm{keV}$  in an array of  $16\times32$  angular positions offering full  $4\pi$  solid angle coverage. Other data suites exist, such as the Hot Plasma Component Analyzer (HPCA) [51], which can

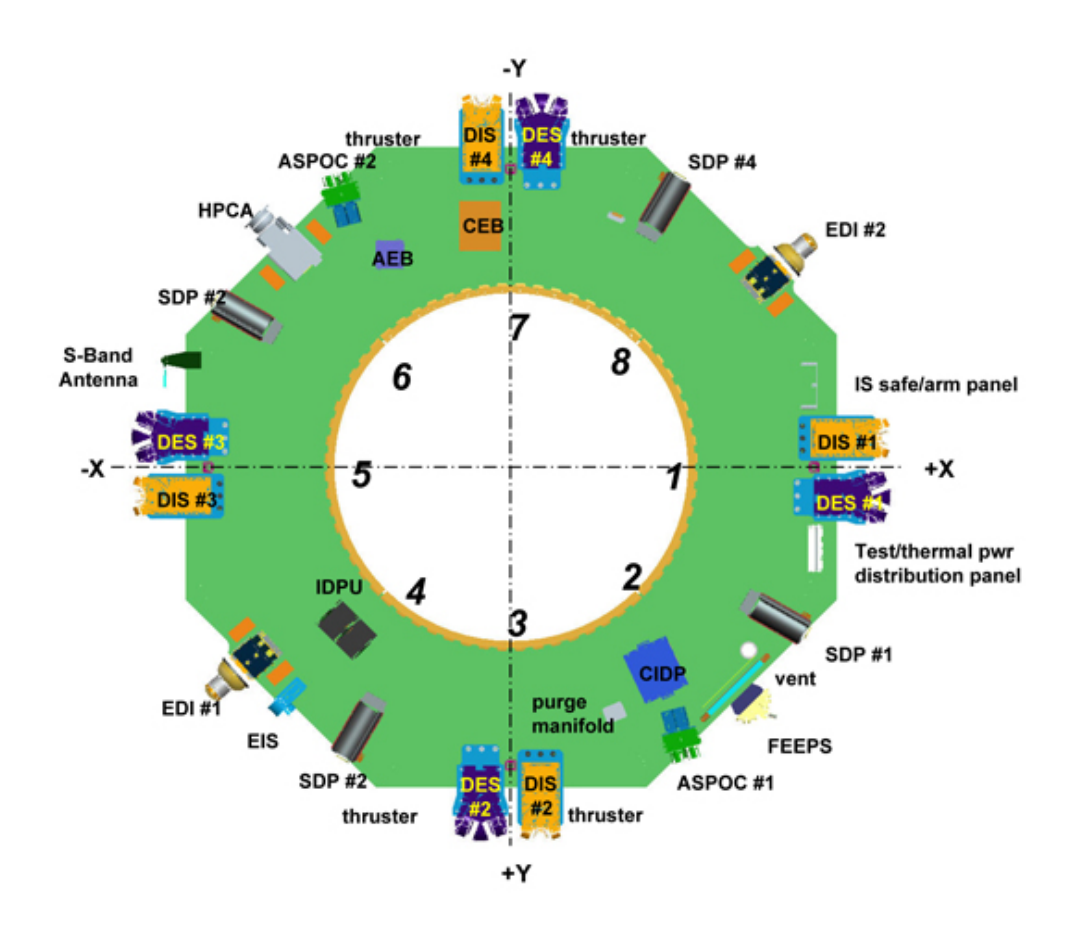


Figure 1.7: An illustration of the instrument suites mounted to MMS. Image credit: NASA.

determine the composition of ions measured, and the Energetic Particle Detector (EPD) [52], which measures ions in the higher energy range of 20-500 keV. While these instrument suites certainly provide information useful to reconnection (and other related space plasma physics), they will not be used in this thesis. More information about how data from MMS is handled and interpreted in this thesis can be found in Appendix A.

This influx of high quality data on naturally occurring magnetic reconnection has inspired many numerical and theoretical studies to explain

what is seen in the data. This thesis will largely fall into that category, though one chapter will focus on a model that can improve the utility of MMS data, and another will focus on a model based on earlier spacecraft observations and kinetic simulations of the magnetotail.

MMS data is driving high-quality research along many avenues. On the dayside, at least 32 MMS crossings through or nearly through the electron diffusion region have been identified [53]. Examples of research using MMS data include explanations for crescent-type distributions observed at the magnetopause [54, 55], studies of Ohm's law at the x-line [10, 13, 56], and observations of extended current layers [57]. Beyond the primary mission of studying magnetic reconnection, MMS has also fueled work on the solar wind turbulence [58, 59] and particle acceleration mechanisms at Earth's bowshock [60].

#### 1.5 Outline of Thesis

This thesis will cover a variety of topics related to current research in magnetic reconnection. Chapters in this thesis will often be inspired by specific reconnection events observed by MMS, and they will include a combination of theory, computation, and analysis of MMS data; Chapter 4 is inspired by the MMS setup, but not by any particular event, though it has the potential to aid in the interpretation of MMS data for many events. Chapter 2 will discuss the validation of an anisotropic electron pressure closure with *in situ* MMS spacecraft data. This includes a comparison between MMS observations of a reconnection region, the predictions of the anisotropic equations of state (EoS), and simulations designed to match the MMS observation. Two simulations will be compared, showing that a hybrid simulation using kinetic ions and an electron fluid following the EoS outperforms a fully-kinetic simulation with the reduced mass ratio  $m_i/m_e=100$ . With the closure validated, a prediction of electron heating

in the exhausts of high guide field reconnection events that relies on the EoS is presented.

Chapter 3 extends the work of Chapter 2 to another set of MMS observations, this time of an asymmetric event. It is shown that the EoS can predict the observed electron pressure when using separate upstream populations corresponding to the two inflows and the exhaust. This event was far downstream of the x-line ( $100d_i$ ), which is farther out than the EoS had been tested before. Furthermore, this event was embedded in a region undergoing magnetic compression, and this requires some corrections to the adiabatic model, which are shown to model the observed perpendicular electron heating on top of the original EoS, with local trapping playing a significant role.

Chapter 4 presents a drift kinetic model for obtaining gradients in plasma properties based on local (single-point) distribution function measurements. This model allows for the first order prediction of perpendicular gradients of arbitrary moments of the electron distribution function of a plasma where the electron dynamics are assumed to be gyrotropic. This model is verified with data from a fully kinetic PIC simulation.

Chapter 5 summarizes and concludes the thesis.

### 2 Validation of Anisotropic Electron Fluid Closure through in situ Spacecraft Observations of Magnetic Reconnection

#### 2.1 Introduction

During magnetic reconnection, a plasma converts magnetic energy into particle kinetic energy through a change in the magnetic topology of the system [7]. This process undergirds many explosive energetic processes across the universe, from sawtooth crashes in tokamaks [5], to coronal mass ejections in the sun [4], even possibly to gamma ray bursts in distant galaxies [6].

Understanding the heating of electrons during reconnection is a fundamental problem [3, 61–63], which is not least because of their complicated kinetic dynamics. While fully-kinetic codes are available for reconnection studies [64–66], systems such as solar flares remain far too large to be numerically tractable. Furthermore, even for smaller systems, fully-kinetic models are often implemented at reduced ion-to-electron mass ratio  $m_i/m_e \ll 1836$ , which can impact the properties of the electron fluid. Simplified fluid closures are thus desired in large part because of the reduction in computational intensity they provide. For a fluid closure to be useful, it must retain the dominant kinetic effects of the system in question while not requiring resolution of the smallest of the disparate scales that arise in plasma physics.

Several closures have been formulated to capture certain aspects of kinetic physics. For example, the Hammett-Perkins closure [67] is derived by matching the linear Landau damping rate and then adding in various kinetic effects important to the system being studied [68–72]. Other closures aim to maintain the Hamiltonian structure of the kinetic equation

[73] or add specific source terms [74]. Some closures incorporate pressure anisotropy, such as the Chew-Goldberger-Low (CGL) [42] model and its extensions [75]. Recently, anisotropic Hammett-Perkins-like closures have been applied to reconnection studies [76, 77].

In this chapter we revisit a closure by Lê et al. [41] (as introduced in Section 1.3, and which we will refer to as "the EoS") derived in the adiabatic limit of fast electron transit time. In this limit of  $v_{the} \to \infty$ , the Hammett-Perkins closure predicts fully isotropic distributions; however, the model by Lê *et al.* retains electron trapping effects moderating their heat fluxes and permitting pressure anisotropy to build. Previously this closure has tested favorably against 2D kinetic simulations, but no observational data with sufficiently high resolution was available to rigorously test the closure against naturally occurring reconnection geometries. Here we apply in situ Magnetospheric Multiscale (MMS) [54] observations to validate the closure. Notably, the model does not include off-diagonal elements of the pressure tensor, which can be important in breaking the frozen in condition [78]; however, on-diagonal anisotropy is sufficient to characterize the electron fluid outside the electron diffusion region. The confirmation of the closure model emphasizes the important role of electron trapping in regulating the anisotropic electron temperatures, providing reviewed insight to the processes most important for electron energization during magnetic reconnection.

## 2.2 Basic Physics Governing Electron Pressure Anisotropy

In collisionless magnetized plasmas such as the solar wind and Earth's magnetosphere, the electron fluid's pressure tensor components parallel and perpendicular to the local magnetic field become decoupled, and the electron distribution function often develops significant anisotropy.

The renowned analysis by Chew, Goldberger, and Low [42] considered well magnetized particles in a collisionless plasma and used a kinetic description to derive the following evolution equations for the parallel and perpendicular pressure components

$$\frac{n^3}{B^2} \frac{\mathrm{d}}{\mathrm{d}t} \left( \frac{p_{||} B^2}{n^3} \right) + \boldsymbol{\nabla} \cdot (q_n \mathbf{b}) - 2q_s \boldsymbol{\nabla} \cdot \mathbf{b} = 0 \quad , \tag{2.1}$$

$$nB\frac{\mathrm{d}}{\mathrm{d}t}\left(\frac{p_{\perp}}{nB}\right) + \boldsymbol{\nabla}\cdot(q_{s}\mathbf{b}) + q_{s}\boldsymbol{\nabla}\cdot\mathbf{b} = 0 \quad . \tag{2.2}$$

Here the parallel heat flux  $\mathbf{q}_{||} = (q_n + 2q_s)\mathbf{b}$ , with  $q_n = \int m w_{||}^3 f \mathrm{d}^3 v$  and  $q_s = 1/2 \int m w_{\perp}^2 w_{||} f \mathrm{d}^3 v$  representing the parallel flux of parallel and perpendicular thermal energies, respectively, where  $\mathbf{w}$  represents the random thermal motion with  $\langle \mathbf{w} \rangle = 0$ . The special case where the heat fluxes  $q_n$  and  $q_s$  vanish is known as the CGL limit, in which it follows that  $p_{||} \propto n^3/B^2$  and  $p_{\perp} \propto nB$  [42].

In general, however, plasmas can support large heat fluxes. In a well-magnetized plasma, the parallel heat flux tends to be much larger than the heat flux across field lines. In a collisional plasma the parallel heat flux is well modeled as  $\mathbf{q}_{||} = (q_n + 2q_s)\mathbf{b} = -\kappa_{||} \nabla_{||} T$  [79]. In the case of a collisionless plasma, as is seen in Earth's magnetosphere, this Braginskii scaling implies an infinitely high heat conduction  $\kappa_{||} \sim v_{th}^2 \tau_{\text{collision}} \to \infty$ . Eqs. 2.1 and 2.2 then yield the Boltzmann limit where the plasma is isothermal along field lines. Derivations of the CGL and Boltzmann scalings can be found in Appendix B.

In reality, even in the collisionless limit, heat conduction remains finite, as it is limited by the finite thermal speed  $v_{th}$ . This effect is captured in Hammett-Perkins-like closures [69], including those recently implemented for collisionless reconnection simulations [77]. Here the CGL limit is approached for perturbations with  $\omega/(k_{||}v_{th})\gg 1$ , whereas the Boltzmann response emerges in the opposite limit,  $\omega/(k_{||}v_{th})\ll 1$ . For a typical reconnec-

tion inflow speed of  $0.1v_A$ , (where the Alfvén velocity is based on only the reconnecting component of the magnetic field  $B_r$ ), we may estimate for the reconnection region dynamic time and length scales that  $2\pi/\omega \simeq d_i/(0.1v_A)$  and  $2\pi/k_{||} \simeq 10d_i\sqrt{B_g^2+B_r^2}/B_r$  (the length of fieldlines assuming the system scale is  $10d_i$  in the direction of the reconnecting field), such that for electrons  $\omega/(k_{||}v_{th,e}) \simeq (v_A/v_{th,e})\sqrt{B_g^2+B_r^2}/B_r = \sqrt{m_e/m_i}/\sqrt{\beta_e}$ . This implies that in magnetospheric reconnection geometries the electron dynamics fall in the regime  $\omega/(k_{||}v_{th,e}) \simeq \sqrt{1/1836}/\sqrt{0.1} \simeq 0.1 \ll 1$ . Thus, Hammett-Perkins-like closures predict that the electron thermal streaming is sufficiently large that the electron fluid should be well represented by the Boltzmann limit.

For a collisionless plasma we find another mechanism, particle trapping (not included in the Hammett-Perkins closure scheme), to be most important for moderating the electron heat fluxes. Conservation of energy and magnetic moment for magnetized particles allows for trapping both by the mirror force and electric pseudopotentials that develop along field lines. In essence, the trapped particles have no heat exchange with the external plasma and the pressure components of the trapped population follow the CGL limit where  $p_{||} \propto n^3/B^2$  and  $p_{\perp} \propto nB$ . The closure of the EoS accurately distinguishes between the passing populations (with infinite heat conduction), and trapped populations (with zero heat conduction), yielding a smooth transition between the Boltzmann and CGL limits based the relative fraction of trapped particles. The theoretical basis for the model is discussed further below, with MMS observations providing examples of the structure of the electron distribution functions underpinning this EoS closure.

#### 2.3 MMS Observations

On October 31, 2015 around 07:16 UT, MMS encountered a reconnection region, as described by Ref. [80]. As illustrated in Fig. 2.1a), MMS passed through the exhaust  $\sim 7-10~d_i$  from the x-point. In this event, reconnection occurred between two colliding reconnection exhaust jets in a compressed current sheet at the center of a magnetic flux rope at Earth's magnetopause and was roughly symmetric with a large guide field,  $B_g \sim 2B_r$ . Fig. 2.1b) shows the magnetic field components and how the guide field dominates. The drift kinetic model of Refs. [2, 81] provided the basis for the EoS and predicts electron distributions of the form

$$f(\mathbf{x}, \mathbf{v}) = \begin{cases} f_{\infty}(0, \mu B_{\infty}) & \text{trapped} \\ f_{\infty}(\mathcal{E} - e\phi_{||} - \mu B_{\infty}, \mu B_{\infty}) & \text{passing} \end{cases}$$
(2.3)

for a potentially anisotropic upstream distribution function  $f_{\infty}(\mathcal{E}_{||},\mathcal{E}_{\perp})$  with upstream magnetic field strength  $B_{\infty}$  and fieldline integrated parallel electric potential  $\phi_{||}$  [34], where  $\mu$  is the adiabatic invariant magnetic moment, and  $\mathcal{E}$  is the electron kinetic energy. MMS observations for this event follow this form of the distribution function for a bi-Maxwellian upstream distribution with  $n_{\infty}=7.1\,\mathrm{cm}^{-3}$ ,  $B_{\infty}=55.5\,\mathrm{nT}$ ,  $T_{e\perp\infty}=32.4\,\mathrm{eV}$ , and  $T_{e||\infty}=1.22\,T_{e\perp\infty}$ .

By calculating the density moment  $n(B,\phi_{||})=\int fd^3v$  of Eq. 2.3, it is clear that  $\phi_{||}$  is important in regulating the density of the electrons [41]. An ambipolar parallel electric field develops across ion scales, and a profile of  $\phi_{||}$  develops to ensure  $n_e \simeq n_i$ , required by the principle of quasineutrality. The relatively large parallel potential  $(e\phi_{||}>T_{e||\infty})$  that forms in the exhaust leads to elongated distributions with enhanced electron density, while  $\phi_{||}<0$  repels electrons and leads to a lower density. This can be seen in Figs. 2.1c), d), and e), corresponding to the inflow, density cavity, and density peak, respectively, where the distribution function measured

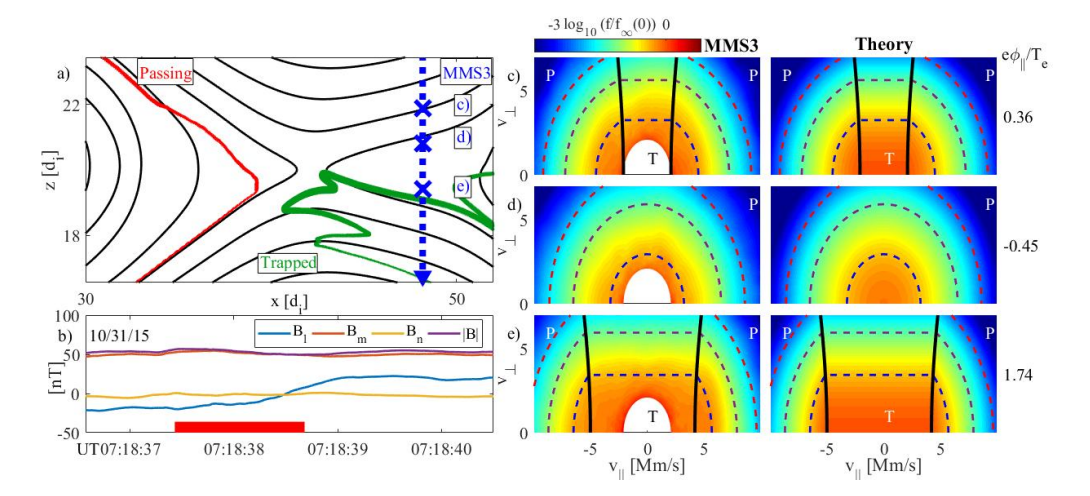


Figure 2.1: a) Sample geometry of magnetic reconnection and the path MMS3 took through the exhaust. Examples of typical trapped and passing particle trajectories are drawn in. b) Magnetic field traces that MMS3 measured along its trajectory. c), d), and e) are the electron distribution functions measured by MMS3 at the points marked in a), which correspond to the inflow, the density cavity, and the peak density in the exhaust. Black contours represent the trapped-passing boundaries, and the model distribution is to the right. The dashed theoretical contours correspond to the same phase space density in all three distributions.

by MMS is overlaid with the theoretical contours. The inflow is weakly anisotropic and contains a small trapped population. The density cavity has a repulsive potential, causing all electrons in the chosen time window to belong to the passing population. In this strong guide field regime, the magnitude of the magnetic field does not change much across the reconnection layer. As such, electrons are primarily trapped by  $\phi_{||}$ , demonstrated by the small opening angle of the trapped-passing boundary.

As is evident from Fig. 2.2b) this event exhibited strong parallel electron heating, especially where the density was enhanced in the reconnection exhaust. It is also notable that  $T_{e||}$  did not drop in the exhaust's density cavity. The observed levels of anisotropic heating can be predicted based

on the model for f in Eq. 2.3. As in Ref. [41], higher order velocity moments of this distribution can be taken to also obtain  $p_{||}$  and  $p_{\perp}$  as functions of  $B/B_{\infty}$  and  $\phi_{||}$ . Notably, for any given value of B,  $n(\phi_{||})$  is invertible, such that  $\phi_{||}(n)$  can be used in the pressure moment equations to yield the equations of state (EoS)  $p_{||}(n,B)$  and  $p_{\perp}(n,B)$ . This is readily done numerically for any reasonable upstream distribution  $f_{\infty}(\mathcal{E}_{||},\mathcal{E}_{\perp})$ .

The parallel and perpendicular ele ctron temperatures measured as MMS3 traverses from the density cavity to the density peak are shown as a function of density in Fig. 2.2a). Scaling predictions for  $T_{e||}$  in the Boltzmann and CGL regimes are overlaid on the plot, as well as the EoS scalings that span the two regimes. It can be seen that the CGL scaling holds in the high density regime, where a stronger parallel potential develops and traps more electrons, simultaneously inhibiting heat conduction along field lines. In the low density regime, the majority of electrons come from passing orbits, which are mostly shifted in energy by  $\phi_{||}$ . This causes the low density regions to approach the familiar Boltzmann limit of constant temperature. The EoS, shown with black dotted lines, are able to successfully span these two regimes and predict the parallel and perpendicular electron temperatures accurately.

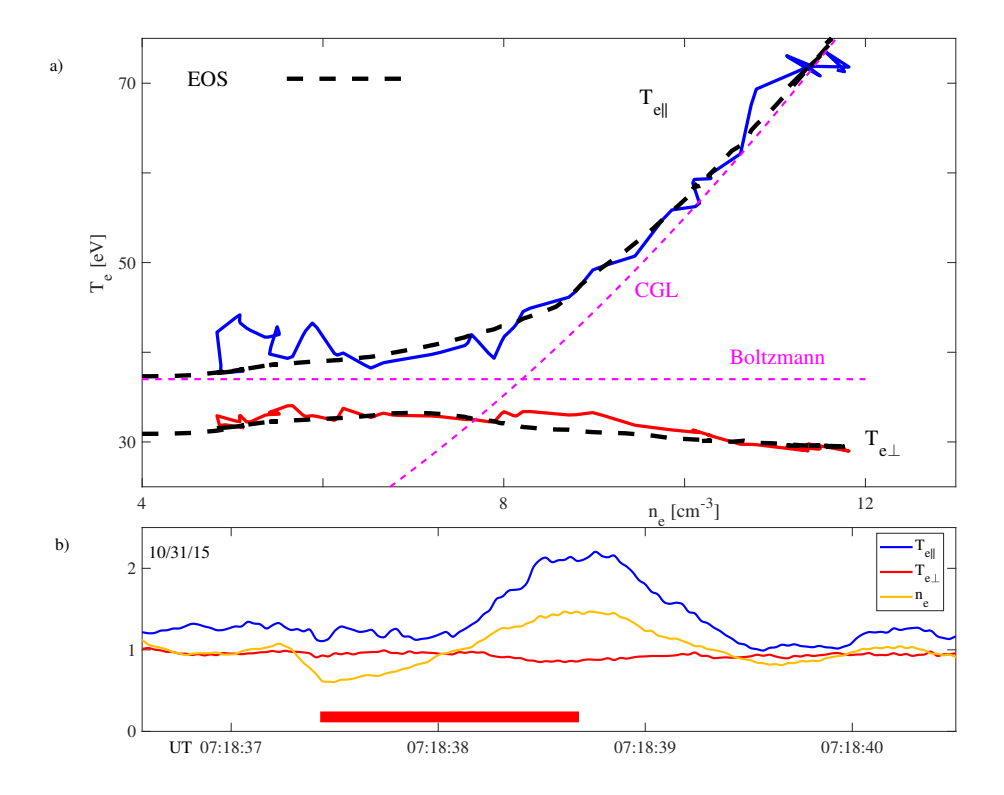


Figure 2.2: a) Electron parallel and perpendicular temperatures, plotted as functions of the number density. These measurements recorded by MMS3 are compared to Boltzmann, CGL, and the EoS scalings. The data plotted correspond to the segment of time marked by the red bars in b) and Fig. 2.1 b). b) Electron density and temperatures measured by MMS3, with density normalized to  $n_0 = 8 \, \mathrm{cm}^{-3}$  and temperatures normalized to  $T_0 = 34 \, \mathrm{eV}$ .

#### 2.4 Comparison to Simulations

The EoS can be applied in simulations, where aspects of the kinetic behavior of the electrons can be captured without introducing disparate time and spatial scales. Previously, fluid simulations using the EoS closure have been shown to reproduce some regimes of kinetic electron dynamics in reconnection [43, 48], while ion kinetic effects can be retained through the use of hybrid (kinetic ion/fluid electron) simulations. To compare with MMS data, we performed an H3D hybrid simulation [47] with an anisotropic electron pressure closure [46] with parameters to match the event presented in this chapter ( $B_g/B_r=1.75$ ,  $\beta_e=0.02$ ,  $T_i/T_e=9.1$ ) with force-free initial conditions. In this simulation, the ions are treated kinetically via the particle-in-cell (PIC) method, and the electrons are modeled as a fluid with pressures determined by an approximate form of the EoS [41], as in [46], with upstream anisotropy  $T_{e||}=1.22~T_{e\perp}$ . The domain is  $2048\times1024$  cells =  $80d_i\times40d_i$  and contains 400 numerical ion particles per cell. An explicit hyperresistivity breaks the frozen-in condition.

The results of this simulation at  $t=80/\Omega_{ci}$  are comparable to the MMS observations. Color contours of electron density can be seen in Fig. 2.3a). The exhaust was identified to be approximately  $3.5~d_i$  wide in Ref. [80]. We identify a cut of the exhaust in the simulation with approximately this width. Fig. 2.3b) shows the electron temperatures and density (normalized to upstream values) along this cut. These results are in good quantitative agreement with MMS observations in Fig. 2.2a).

Fully-kinetic simulations at reduced mass ratio do not reproduce the electron heating as accurately as the hybrid simulation with the EoS. The cut obtained from a VPIC [66] simulation with  $m_i/m_e=100$  and the same upstream parameters is shown in Fig. 2.3c). A significant dip in  $T_{e||}$  is observed within the density cavity. This is in contrast to the hybrid simulation, which breaks from the CGL-like scaling at low values of n. The distinction comes from the large parallel heat flux allowed by the

passing electrons when the electrons stream much faster than the bulk reconnection dynamics. For low mass ratio PIC simulations the electron thermal speed, which scales as  $\sqrt{m_i/m_e}$  relative to the Alfvén speed, does not provide sufficient parallel heat flux to prevent a temperature dip in the density cavity. This follows from the analysis of the Hammett-Perkins closure in Section 2.2, where  $\omega/(k_{||}v_{th,e})\simeq\sqrt{m_e/m_i}/\sqrt{\beta_e}$ ; however, with a reduced mass ratio of 100, we now have  $\omega/(k_{||}v_{th,e})\simeq 1$  which is no longer in the asymptotic limit for the actual physical mass ratio, and even fully passing populations of numerical electrons cannot support the physical heat flux. As such, the massless electron limit of the EoS more accurately models the parallel heat flux of the physical system. Thus, for trapped electron dynamics during reconnection, the limit  $m_i/m_e \to \infty$  is more faithful to the true system dynamics than a fully-kinetic simulation with  $m_i/m_e \sim 100$  while simultaneously being far less computationally intensive.

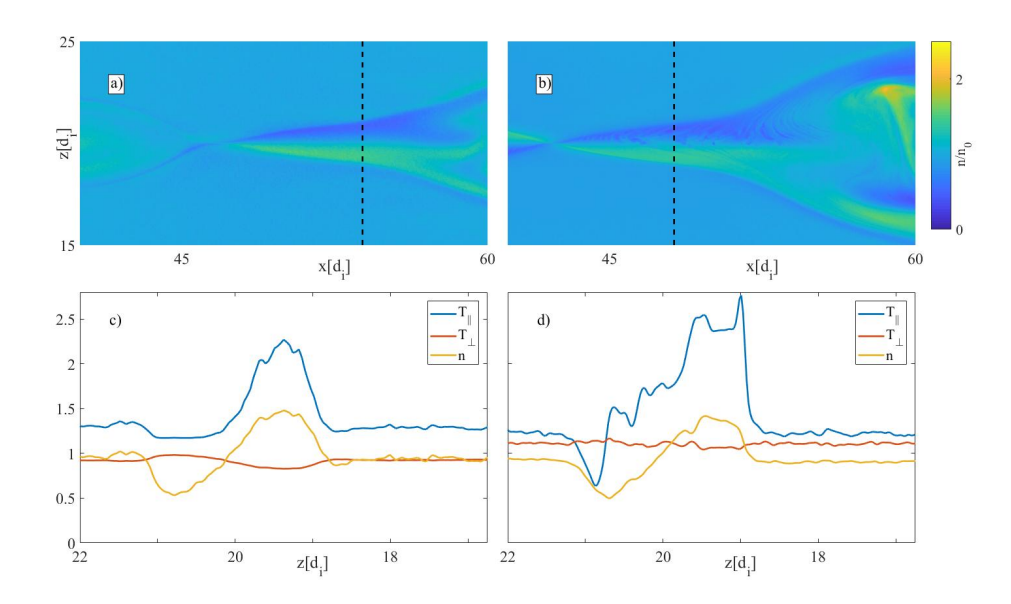


Figure 2.3: Density profile of the a) hybrid and b) fully-kinetic simulations. c) Normalized electron density and temperatures from the hybrid simulation along the cut marked in a). d) Normalized electron density and temperatures from the fully-kinetic mass ratio 100 simulation along the cut marked in b).

#### 2.5 Heating Predictions

The observational results presented above document how the electron heating is controlled by the local values of n and B relative to  $n_{\infty}$  and  $B_{\infty}$  of the external plasma feeding the electrons parallel streaming into the region. Thus, with the EoS the electron heating problem is reduced to the problem of determining representative exhaust values of  $n/n_{\infty}$  and  $B/B_{\infty}$ . This process was previously shown in [48] for a moderate guide field regime and [82] near the x-point in antiparallel reconnection. For moderate to low guide field regimes, the electrons approach the firehose limit where  $p_{e||}-p_{e\perp}\simeq B^2/\mu_0$  providing (with force balance across the

layer) equations that can be applied for determining  $n/n_{\infty}$  and  $B/B_{\infty}$  and thereby estimating the electron heating as a function of the upstream plasma parameters.

In the limit of high guide field, the current sheet typically does not approach the marginal firehose condition, meaning that some other condition must be applied to estimate typical values of  $\tilde{n}$  and  $\tilde{B}$ . Here, we use the ansatz that the overall magnetic field strength should reduce to the strength of the guide field where the temperature peaks. We then solve for the density perturbation through force balance across the layer with adiabatic ions. In the limit that  $\beta_{i\infty}\gg\beta_{e\infty}$ , the inputs for the EoS become

$$\tilde{B} = \frac{B_g}{\sqrt{B_r^2 + B_g^2}} \quad , \qquad \tilde{n} = \left(1 + \frac{1}{\beta_r}\right)^{\frac{1}{\Gamma}} \quad , \tag{2.4}$$

where  $\beta_r$  the ion beta based on the reconnecting field strength. From this,  $\Delta T_e/T_e$  can be defined as  $(\tilde{p}_{e||}+2\tilde{p}_{e\perp})/(3\tilde{n})-1$ . Fig. 2.4 shows the predicted electron heating across the layer versus  $\beta_r$ . This can be compared to observations in [3], which identify  $\Delta T$  to scale as  $m_i v_A{}^2 = B_r^2/n\mu_0$ . For high beta plasmas, we do not expect much heating. On the contrary, in the low-beta regime we asymptotically expect heating to go as

$$\Delta T_e = \frac{\pi}{18} T_e \frac{B_r^2 + B_g^2}{B_q^2} \beta_r^{-\frac{2}{\Gamma}} = \frac{\pi}{18} T_e \frac{B_r^2 + B_g^2}{B_q^2} \beta_r^{-\frac{6}{5}}$$
 (2.5)

based on the approximate form of the EoS found in Eq. 4 of [83].

When normalized relative to the previously assumed scaling of  $m_i v_A^2$ , we see that only a weak beta dependence is retained, making it roughly consistent with a constant over the range of  $\beta$  observed, where guide field strength and electron-ion temperature ratios play a more significant role.

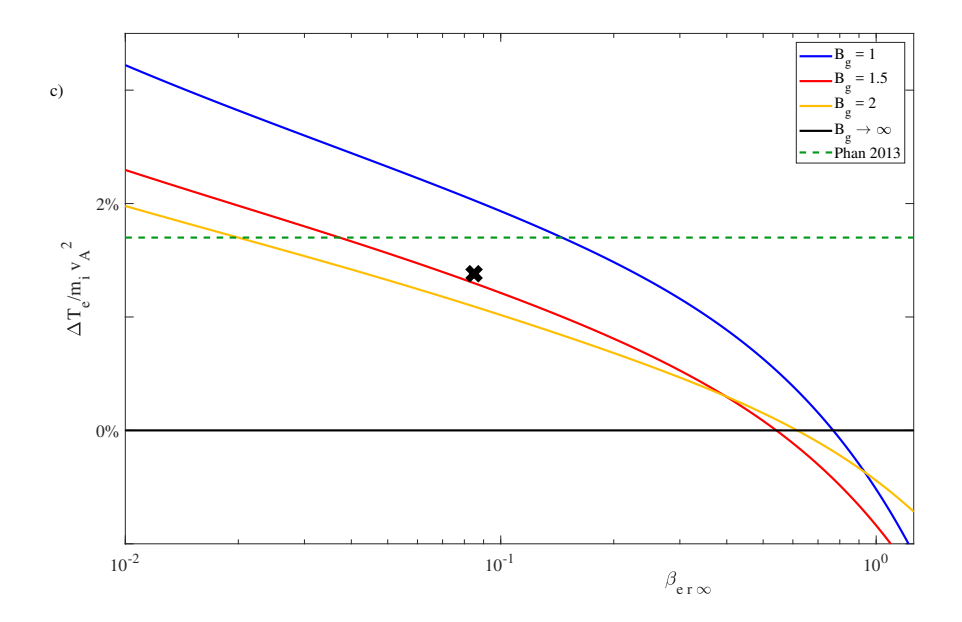


Figure 2.4: Predictions for electron temperature gain across the reconnection layer by the EoS with an adiabatic ion closure. Note the weak scaling relative to that laid out in [3]. This plot was produced assuming  $T_{i\infty}/T_{e\infty}=10$ . The X roughly marks the temperature gain observed in the 10/31/15 event, where  $B_g=1.75$  and  $\beta_{er\infty}=0.085$ , while the observational scaling of Ref. [3] is shown as a green dashed line.

$$\frac{\Delta T_e}{m_i v_A^2} = \frac{\pi}{36} \frac{T_e}{T_i} \frac{B_r^2 + B_g^2}{B_g^2} \beta_r^{\frac{\Gamma - 2}{\Gamma}} = \frac{\pi}{36} \frac{T_e}{T_i} \frac{B_r^2 + B_g^2}{B_g^2} \beta_r^{-\frac{1}{5}}, \quad \text{valid for } T_i \gg T_e \text{ , } B_g/B_r \gtrsim 1.$$
(2.6)

Based on this weak asymptotic scaling and the curves of the full force balance solution in Figure 2.4, we conclude that  $\Delta T_e/(m_i v_A^2) \simeq 0.02$  for  $B_g/B_r \gtrsim 1$  and typical magnetospheric  $\beta_{er\infty} \simeq 10^{-2} - 10^{-1}$ , and as such, this heating scaling is consistent with the observed scaling in [3].

#### 2.6 Discussion and Conclusions

In summary, we have demonstrated the validity of the EoS for guide field reconnection with in situ MMS observations of magnetic reconnection for the first time. Furthermore, we find that an implementation of the EoS as an electron fluid closure for hybrid simulations with PIC ions better reproduces these MMS observations than fully-kinetic PIC simulations at reduced values of  $m_i/m_e$ . This highlights how the closure of the EoS is applicable to numerical simulations, especially pertaining to the problem of electron energization in large scale plasma configurations subject to magnetic reconnection. Finally, we used the EoS to predict how electron heating scales in the exhausts of strong guide field reconnection, finding a result that is consistent with existing observational evidence. Going forward, the EoS can provide further insight into the interpretation of MMS data. For example, by fitting MMS data to the EoS it is possible to infer the upstream conditions, which may not be clear from the data traces provided by MMS. This theme will partially be explored in Chapter 3, where we will see an event whose upstream conditions are nowhere seen in the MMS data trace. The results of this chapter were published in Ref. [84].

## 3 Anisotropic Electron Fluid Closure Validated by *in situ* Spacecraft Observations in the far Exhaust of Guide-Field Reconnection

#### 3.1 Introduction

Magnetic reconnection is the process that changes the magnetic topology of a plasma system [7] and is often associated with a rapid conversion of magnetic energy into kinetic energy in bulk flows, fast particles, and thermal heating. Reconnection fuels energetic events in many plasma systems, including solar flares and coronal mass ejections on the sun [4, 85] and magnetic substorms in Earth's magnetotail [86]. Reconnection is the key process that allows solar wind plasma to enter Earth's magnetosphere [87, 88], chiefly at the dayside magnetopause.

While it is known that reconnection converts magnetic energy into particle kinetic energy, the details of the energy transfer are still only partially understood. In particular, the processes by which electrons gain energy are important, as radiation originating from hot electrons constitutes the best observational evidence of astrophysical magnetic reconnection [1]. Observational work has shown that the electron temperature gain via bulk heating  $\Delta T_e$  in the reconnection exhaust scales proportionally to  $m_i v_A^2$ , where  $v_A$  is the Alfvén speed in the inflow based on only the reconnecting component of the magnetic field [3]. Further work with fully-kinetic simulations suggests that an electron heating mechanism must satisfy several properties, including the experimentally observed scalings with little dependence on the distance from the x-line, and preferential heating in the direction parallel to the local magnetic field [89].

Electron energization occurs both in the electron diffusion region and outside of it [82]. Inside the electron diffusion region, electrons are acceler-

ated during the course of meandering orbits [90, 91]. Several methods for electron energization outside of the electron diffusion region have been proposed, which can broadly be categorized by whether the acceleration is a result of the parallel or perpendicular components of the electric field. Direct acceleration models rely on parallel electric fields (seeded by the reconnecting electric field) to accelerate electrons along field lines. In the guiding center limit, perpendicular electric fields can energize electrons through a nonzero dot product with electron drifts. Fermi-type models [62] rely on the dot product of perpendicular electric fields and the electron curvature drift. The  $\nabla B$  drift can also energize electrons [61], which in the adiabatic limit constitutes betatron heating. Dependence of energization on velocity space also varies between the mechanisms. Direct acceleration via a single x-line provides a relatively constant energy boost, while the mechanisms that energize via perpendicular electric fields can provide energy gains proportional to the initial electron energy, allowing for power-law tails to develop in the electron distribution function. Fermi-type mechanisms primarily energize in the direction parallel to the magnetic field and the heating efficiency decreases significantly in the presence of a guide magnetic field [63]. For comparison to observation, it is also important that Fermi-type models generally consider the heating of particles in closed systems, providing an evaluation of the average heating as magnetic flux loops contract, with no information on temperature variations along the magnetic flux tubes.

In nature, however, reconnection regions are often embedded in larger plasma systems. Given the low mass of the electrons, their thermal speed is (in most cases of interest) much larger than the Alfvénic plasma bulk motion. The heat fluxes of the electrons streaming along magnetic field lines then become essential to the regulation of the electron temperature. In fact, as discussed in Section 2.2, by making a few estimates regarding the geometry of the reconnection region, closures derived from simple

kinetic models [69] show space plasmas with  $\beta_e \gtrsim 100 m_e/m_i \approx 0.05$  have an electron thermal speed large enough to imply that they can support sufficiently strong heat conduction for the plasma to be in an MHD-like regime; in this regime, the electron temperature throughout the reconnection region is uniform and set by the temperature of the ambient plasma. As such, the electron pressure would follow the Boltzmann scaling p = nTwith a fixed temperature  $T = T_{\infty}$ . Guided by spacecraft observation [92] it has been established that the main mechanism for reducing the parallel electron heat flux is trapping of electrons in their rapid motion along magnetic field lines. This trapping can be a consequence of both the magnetic mirror force as well as parallel electric fields. Considering the limit of a vanishing electron mass  $(m_e \rightarrow 0)$  a kinetic model [93] for the electron distribution function was developed, which can account for the variations of the electron distribution function along magnetic field lines, taking the source of electrons streaming in along the magnetic field lines from the plasma ambient to the reconnection region into account.

Given the rather different kinetic response of the electrons parallel and perpendicular to the magnetic field, the electron pressure tensor component aligned with the magnetic field decouples from those perpendicular to the local magnetic field. The kinetic model of Ref. [93] has been shown to hold through kinetic simulations near the x-line [41] and the types of elongated distributions that the model produces have been observed in spacecraft data [37, 92, 94]. Based on the kinetic description a fluid closure model was distilled into equations of state [2, 41] (from here on, referred to as "the EoS") that determine the parallel and perpendicular pressure based on local density and magnetic field strength normalized by the conditions of the upstream plasma populations. Within their realm of validity ( $B_g > 0.2B_{rec}$  [45], and  $\beta_{e\infty} > \sqrt{m_e/m_i}$  [95]) the success of the EoS in describing electron bulk heating in reconnection demonstrates that heat fluxes from the upstream reservoir play an important role in the process.

While the predicted form of the electron distribution functions and the EoS have been verified near the x-line in simulations and with new data [84, 96] from the Magnetospheric Multiscale (MMS) mission [54], so far the model has not been tested in the region far from the x-line.

In this chapter we analyze the MMS event considered by Ref. [97] and demonstrate the applicability of the EoS electron closure model extends far into the exhaust,  $\sim 100d_i$  downstream from the x-line. The implications of this analysis are important because they emphasize the role of nonlocal kinetic effects including electron trapping in regulating the electron energization and heat fluxes at the global scale of magnetospheric reconnection exhausts. The chapter is organized as follows—Section 3.2 begins by revisiting past results on the structure of the reconnection region during guide-field reconnection, including the origin of the quadrupolar density perturbation, which are not widely-known, but are important to understanding the nature of the electron heating process. Section 3.3 presents evidence that the event considered in this chapter is embedded in a region of broad-scale compression, with implications for the scaling of the electron energization. In Section 3.4, we show that the EoS holds for this event far downstream of the x-line for three distinct regions corresponding to the slightly asymmetric inflows and the exhaust. In Section 3.5, we extend the model to include additional perpendicular heating far into the exhaust. Section 3.6 concludes the chapter with a discussion of the results.

# 3.2 General Structure of Electric Fields and Plasma Density during Guide-Field Reconnection

In this section, we review the basic physics underlying the EoS in guide-field regimes of reconnection and demonstrate that the well-known quadrupole density structure is a direct consequence of the in-plane potential and is not tied to the kinetic Alfvén wave— a result that is not widely-appreciated. In Fig. 3.1 we present data from a kinetic simulation for a configuration with  $B_g/B_{rec}=0.8$  implemented at  $m_i/m_e=1836$  for a domain of  $20\times 20d_i$ . This simulation was part of the study presented in Ref. [45], which provides more details on the run.

In estimating the electron heating during guide-field reconnection, it is tempting to assume that the electrons are simply accelerated by the component of the reconnecting electric field aligned with the guide magnetic field [98, 99]. For the present simulation this so-called direct acceleration can be quantified as  $\phi_y = \int_{\mathbf{x}}^{\infty} E_y \mathbf{e}_y \cdot d\mathbf{l}$ , where the integral is computed from a point  $\mathbf{x}$  along the corresponding magnetic field line out to the ambient plasma. As such, in Fig. 3.1a) we calculate  $\phi_y$  by integrating along the direction of the field lines indicated by the arrows all the way to the simulation boundary. Because of the guide field, the path of the integral for points close to two of the four separatrices will include relatively long sections running nearly parallel to the x-line in the out-of-plane direction. Thus, along two of the separatrices we observed  $e\phi_y \simeq 50T_e$ , which is the amount of energization that an electron will gain from the reconnection electric field  $E_y$  when streaming along a magnetic field line through the reconnection region.

This strong energization estimated by  $\phi_y$ , however, is not physical as it would cause charge separation not permitted in a plasma; instead, inplane electric fields develop to quell the electron acceleration. In fact, from

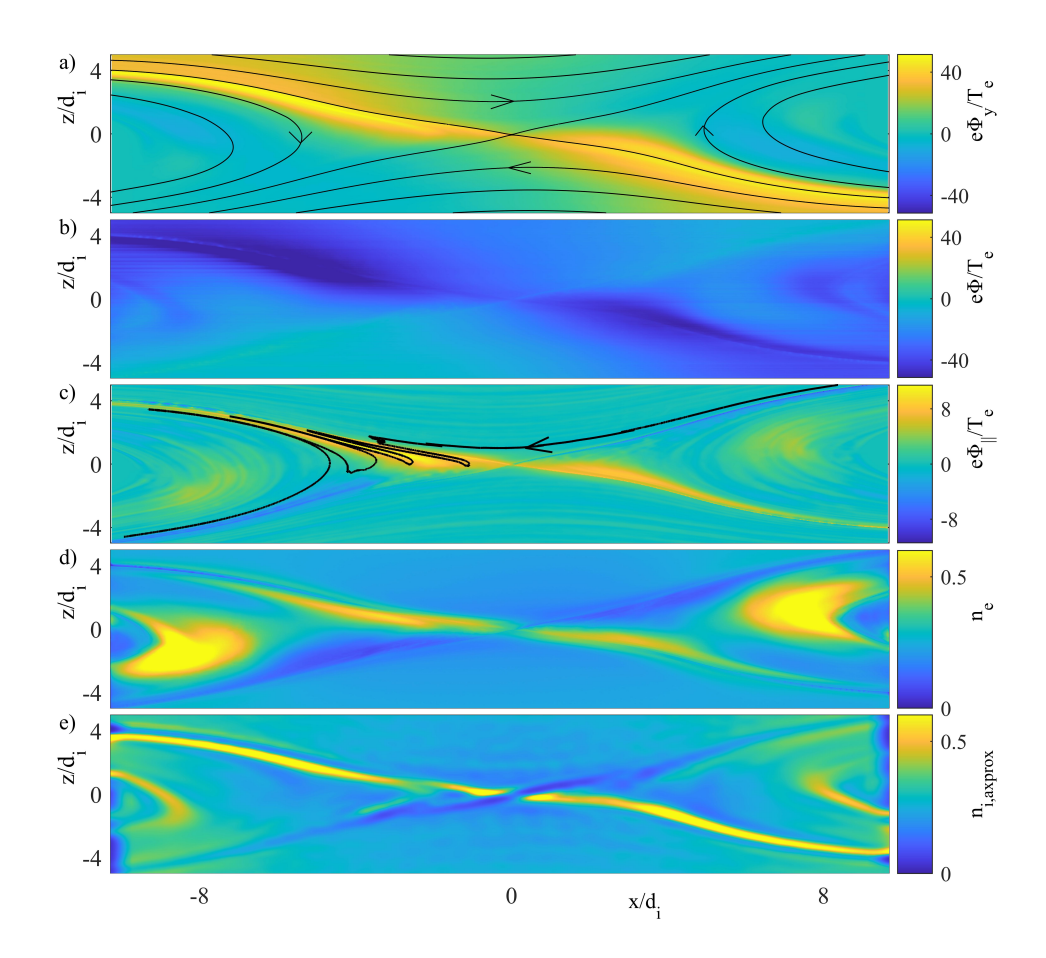


Figure 3.1: a) The so-called direct acceleration potential  $e\phi_y/T_e$ , integrating the out-of-plane electric field along field lines whose in-plane projections are shown in black. b) The in-plane electrostatic potential  $e\phi/T_e$ . c) The combined effect of these two components, the parallel potential  $e\phi_\parallel/T_e = e(\phi+\phi_y)/T_e$ , with an example of an electron orbit in black. d) The electron density  $n_e$  given by the simulation. e) Estimate for the ion density given by Eq. 3.2, based on the profiles of  $\phi$  and B.

the ideal Ohm's law  $\mathbf{E} + \mathbf{v} \times \mathbf{B} = 0$  throughout the bulk of the plasma we have  $\mathbf{E} \cdot \mathbf{B} \simeq 0$ . Thus, the regular in-plane electrostatic potential  $\phi$  in Fig. 3.1b) develops, which to lowest order can be approximated as  $\phi \simeq -\phi_y$ , and prevents significant energization of electrons streaming along the magnetic field lines. In reconnection with a strong guide field  $B_g \gg B_{rec}$ , the in-plane bulk plasma flow is approximately given by  $\mathbf{v} = -\nabla\phi \times \mathbf{e}_y/B_y$ , where  $\phi$  is recognized as the plasma flow function, familiar from theoretical models [100] and measured directly in reconnection experiments [35].

To be more accurate, plasma may include parallel electric fields described by

$$E_{\parallel} = -\frac{\nabla_{\parallel} p_{e\parallel}}{e n_e} \tag{3.1}$$

(note that within the electron diffusion region additional terms become important to balance  $E_{\parallel}$ ). This permits a small difference to develop between  $-\phi$  and  $\phi_y$ . As in Refs. [93, 101], we will denote this difference as the acceleration potential  $\phi_{\parallel} = \phi + \phi_y = \int_{\mathbf{x}}^{\infty} \mathbf{E} \cdot d\mathbf{l}$ , shown in Fig. 3.1c). Strictly speaking, this is not an electrostatic potential, but rather a psuedopotential, as inductive field components are included. If we assume a constant electron temperature by integrating Eq. 3.1, it follows that  $e\phi_{\parallel} \simeq T_e \log(n_e/n_{e0})$ . Indeed, with the density profile in Fig. 3.1d) it is clear that  $n_e$  and  $\phi_{\parallel}$  are correlated. However, the amplitude of  $e\phi_{\parallel}/T_e$  is much larger than the estimate provided by  $\max(\log(n_e/n_{e0})) \simeq 1$ . This is evidence of parallel electron heating, which will be explored below.

In contrast to the electrons, the ions, with their relatively slow thermal motion, do not travel extended distances along the magnetic field lines, and the ion density is therefore largely insensitive to the profile of  $\phi_{\parallel}$ . However, the in plane electric fields characterized by  $-\nabla \phi$  can induce strong ion polarization currents  $\mathbf{J}_p = -(nm_i/B^2)\partial\mathbf{E}_{\perp}/\partial t~(=en\mathbf{v}_p)$ . Combining this with the Lagrangian version of the continuity equation,  $dn/dt+n\nabla\cdot\mathbf{v}_p=0$ , for a fluid element following a magnetic flux-tube into the reconnection region, it follows that  $\log n/n_0=(m_i/B^2)\nabla^2\phi$ . In addition, neglecting

parallel bulk motion, the ions will compress/decompress together with the magnetic field and this effect can be modeled as  $n/n_0 = B/B_0$ . Combining the two effects we obtain an estimate for the ion density as

$$n \simeq n_0 \frac{B}{B_0} \exp\left(\frac{\alpha m_i \nabla^2 \phi}{eB^2}\right) \quad ,$$
 (3.2)

which is displayed in Fig. 3.1e). Here we have included a heuristic factor  $\alpha \simeq 0.5$  as the full ion-polarization response is reduced where the structures of  $\phi$  are below the ion Larmor radius and where the convective time derivative of  $\nabla \phi$  is too fast for the ions to respond. The electron density in Fig. 3.1d) displays enhanced regions in the exhaust left over from the initial Harris sheet population. All other features in  $n_e$  are well accounted for by Eq. 3.2. These features include the density enhancements and cavities observed along the separatrices.

The ion density perturbation described above has implications for the dynamics in the vicinity of the x-line. Again, in guide-field reconnection a strong in-plane potential  $\phi$  develops such that  $\mathbf{E} \cdot \mathbf{B} \simeq 0$ , requiring that  $\phi \simeq -\phi_y$ . In turn, the ions' polarization response causes density perturbations which from Eq. 3.2 can be estimated as  $\Delta n \simeq (nm_i/eB^2)\nabla^2\phi$ . By quasineutrality the electron and ion densities must be equal, and the perturbations in the ion density are matched by identical perturbations in the electron density. In turn by Eq. 3.1 these can then support a parallel electric field on the order of  $E_{\parallel} \simeq \rho_s^2 \nabla_{\parallel} \nabla^2 \phi$ , where  $\rho_s = \sqrt{m_i T_e}/eB$  is the ion sound Larmor radius. This was explored in ground breaking simulations by Kleva et al.[100] and later verified experimentally [102], coupling the reconnection dynamics to the kinetic Alfvén wave [103]. Still, we emphasize that the density perturbation itself (see Eq. 3.2) is independent of  $T_e$  and is therefore independent of the dynamics associated with  $\rho_s$ .

An understanding of how the electron density regulates to match the

ion density is provided by the drift-kinetic model of Refs. [2, 81], which predicts electron distributions of the form

$$f(\mathbf{x}, \mathbf{v}) = \begin{cases} f_{\infty}(0, \mu B_{\infty}) & \text{trapped} \\ f_{\infty}(\mathcal{E} - e\phi_{\parallel} - \mu B_{\infty}, \mu B_{\infty}) & \text{passing} \end{cases} , \tag{3.3}$$

where  $\mu$  is the adiabatic invariant magnetic moment, and  $\mathcal{E}$  is the electron kinetic energy. The model assumes a source  $f_{\infty}(\mathcal{E}_{\parallel},\mathcal{E}_{\perp})$  which is a potentially anisotropic upstream distribution function characterizing the passing electrons streaming into the region from an undisturbed ambient plasma with a magnetic field strength  $B_{\infty}$ . The model is derived in the double adiabatic limit where the electron bounce time is faster than any other time scale associated with the reconnection dynamics. An important part of the model is to distinguish the behaviour of passing electrons (streaming along magnetic field lines), and trapped electrons for which an example is given in Fig. 3.1c). By integrating Eq. 3.3 over velocity space, a relationship  $n_e = n_e(\tilde{B}, \tilde{\phi}_{\parallel})$  is found, such that the electron density is controlled by the normalized quantities  $\tilde{B} = B/B_{\infty}$  and  $\tilde{\phi}_{\parallel} = e\phi_{\parallel}/T_{e\infty}$ . Previous studies [2, 41] have shown how  $n_e = n_e(\tilde{B}, \tilde{\phi}_{\parallel})$  can account for the relationship between  $n_e$  and  $\phi_{\parallel}$  displayed in Figs. 3.1(c,d).

The function  $n_e = n_e(\tilde{B}, \tilde{\phi}_{\parallel})$  is well-behaved and can be inverted to yield  $\tilde{\phi}_{\parallel} = \tilde{\phi}_{\parallel}(\tilde{n}_e, \tilde{B})$ . The electron distribution in Eq. 3.3 may then be recast on the form  $f = f(\tilde{n}_e, \tilde{B})$ , from which the pressure moments can be computed numerically. For a given upstream distribution  $f_{\infty}(\mathcal{E}_{\parallel}, \mathcal{E}_{\perp})$ , a set of Equations of State (the EoS) are then obtained,  $p_{\parallel} = p_{\parallel}(\tilde{n}_e, \tilde{B})$ ,  $p_{\perp} = p_{\perp}(\tilde{n}_e, \tilde{B})$ . As discussed in Ref. [41], in the limit of  $\tilde{n}_e/\tilde{B} \ll 1$  the electrons are mostly passing, yielding a Boltzman scaling such that the electron temperature matches the upstream values. In the opposite limit  $\tilde{n}_e/\tilde{B} \gg 1$  heat fluxes are limited by trapping and the anisotropic temperatures approach the CGL limit with  $T_{e\parallel} \propto \tilde{n}_e^2/\tilde{B}^2$  and  $T_{e\perp} \propto \tilde{B}$ . These effects

are accurately captured by the EoS. Again, using fully kinetic simulations and spacecraft observations, the model has been shown to account for the anisotropic electron heating for guide-field reconnection, considering length scales up to  $10d_i$  from the reconnection region [43, 84, 96].

#### 3.3 Evidence of Magnetic Compression

The main subject of the present chapter is an analysis of the reconnection exhaust encounter observed by MMS on January 21, 2016 at approximately 01:06 UT. We will denote this encounter as Event B, wherein MMS crossed through a reconnection exhaust roughly  $100\ d_i$  downstream of the x-line, as analyzed in Ref. [97]. This event had a guide field of roughly 70% of the reconnecting magnetic field component and the inflows were somewhat asymmetric.

As a point of comparison, we will also consider a reconnection event (Event A) that MMS observed on October 31, 2015 as reported in Ref. [80] and Chapter 2 of this thesis. In this event, MMS traversed a reconnection exhaust about  $10d_i$  downstream of the x-line, and our previous analysis of the event provides confirmation of the applicability of the EoS, accurately accounting for the detailed variations in  $T_{e\parallel}$  and  $T_{e\perp}$  across the exhaust. A representation of some of the details of the two events are shown in Fig. 3.2. Event A was a relatively symmetric event with strong guide field that was unusual in the sense that it occurred within colliding reconnection exhausts at the magnetopause [80, 104], but in the sense of the reconnection dynamics observed, it was fairly typical. Meanwhile, as will be demonstrated below, from the details of Event B it is inferred that the full exhaust and inflow regions were compressed such that the magnetic field strength recorded was larger than that of the far away regions from which parallel streaming electrons are sourced.

The EoS is based on the model of a flux tube convecting into the recon-

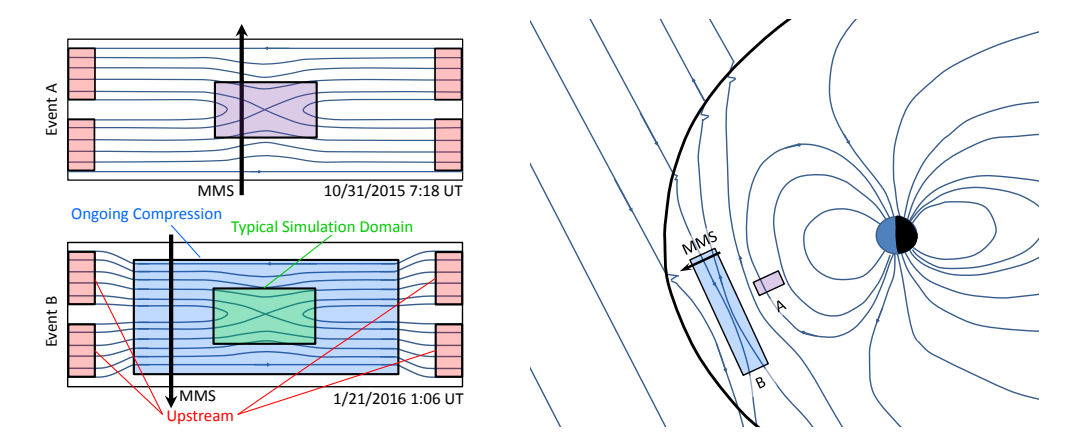
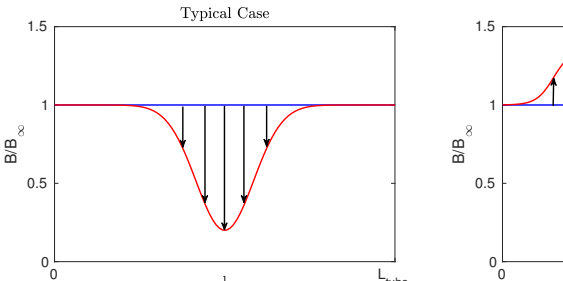


Figure 3.2: Illustration of what the reconnection region could look like on a global scale for Event B. The diagrams on the left roughly correspond to the boxes drawn in the magnetosphere drawing. In Event B, MMS encounters the reconnection outflow farther from the x-line than most kinetic simulations will include. We believe this region is compressed relative to the unperturbed upstream parameters, which occur even farther out. It is notable that this region is actively compressing during the transit of a passing electron from the upstream distribution to the observed location such that  $\partial B/\partial t \neq 0$ . In contrast, Event A occurred within the magnetosphere, and was not compressed relative to the upstream parameters.

necting region. Figure 3.3 shows how the magnetic field strength along a flux tube changes over time in a typical reconnection scenario as compared to a compressing scenario. In a typical reconnection scenario, as a flux tube convects in the reconnection inflow towards the x-line, the magnetic field strength decreases as the reconnecting component of the magnetic field annihilates. As such, an initially uniform magnetic field evolves to include a dip near the x-line, but the ends of the flux tube are generally unaffected. This reduction in the magnetic field allows for the magnetic trapping of well-magnetized electrons, increasing the fraction of trapped electrons relative to the case with only electric trapping.

The typical case of the EoS joins the Boltzmann and CGL [42] scalings as limits of low and high trapped fraction of electrons, respectively. In



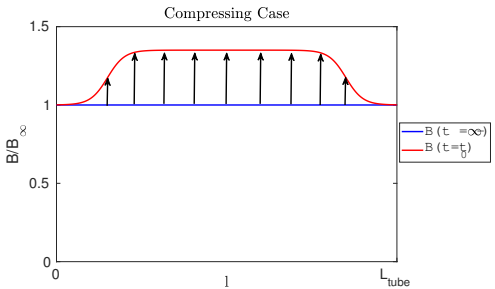


Figure 3.3: How the flux tube evolves from its initial uniform state in a typical reconnection scenario versus the effects of the compression on B. In the compressing scenario, we seed the initial profile of B with several local dips, which can globally trap particles in the initial scenario. As the magnetic field is compressed, the magnetic field at the local minima rises above the upstream field strength, allowing for particles to be locally, but not globally, trapped.

the isothermal Boltzmann limit the temperatures are constant, and in this limit both  $T_{e\parallel}$  and  $T_{e\perp}$  are independent of n. In the CGL limit,  $T_{e\perp}$  scales only with B. As such,  $T_{e\perp}$  is nonincreasing in n/B in the typical case that spans these limits.

Quantities measured by MMS over the course of Event A are shown in Figure 3.4a-c). A particular focus is paid to the region of the exhaust between the density cavity and the density peak, as marked in Fig. 3.4c). Fig. 3.4d) shows that  $T_{e\parallel}$  increases from the cavity to the peak, while  $T_{e\perp}$  decreases slightly, with notable breaks between the Boltzmann and CGL scalings, as would be expected from the scalings of the typical case of the EoS with a strong guide field. The break occurs at  $n=n_{\infty}$ , and is conveniently illustrated by Event A for which the cavity has n lower than its upstream value, while at its the peak n is higher than its upstream value.

The electron distribution function in Fig. 3.4e) observed by MMS within the cavity is relatively isotropic, and all particles are passing due to a negative  $\phi_{\parallel}$ . This is consistent with the negative values of  $\phi_{\parallel}$  also observed in

Fig. 3.1c) along the locations of the density cavities. Meanwhile, moving to the density peak in Fig. 3.4f), the corresponding distribution is significantly elongated in the parallel direction due to a strong, positive  $\phi_{\parallel}$ . The elongation continues to electrons with large  $\mu$  (and becomes slightly stronger) as both electric and magnetic trapping are present in this event.

We now contrast these findings with those of Event B, where the time series measurements of MMS2 are shown in Figs. 3.4g-i), to demonstrate that the reconnection region was embedded in a region where the magnetic field was actively compressing. Looking back to Fig. 3.3 for the case of broad scale compression, the magnetic field strength is increased relative to the upstream value. This significantly alters the dynamics of the electrons as the flux tube convects towards the x-line, as incoming electrons must work against the mirror force to get into the compressed region.

Fig. 3.4j) shows the electron temperatures measured by MMS2 in the region between the density cavity and peak marked in Fig. 3.4i) plotted against the observed values of  $\tilde{n}/\tilde{B}$ . Notably, both  $T_{e\parallel}$  and  $T_{e\perp}$  increase from the cavity to the peak with n/B. As shown above, in the standard case the EoS spans the Boltzmann and CGL limits, which thereby imposes that  $T_{e\perp}$  is nonincreasing in n/B. As such, the profile of  $T_{e\perp}$  that increases with n/B is indicative of an atypical guide-field reconnection event. In the EoS this feature can only be realized for the case of compression where  $n>n_{\infty}$  and  $B>B_{\infty}$ . This scaling continues for the entire region between the cavity and the peak; as such,  $n>n_{\infty}$  and  $B>B_{\infty}$  at every point measured by MMS2 during this event, consistent with broad-scale compression.

A closer look at the electron distribution functions of Event B provides further evidence of the compression. In Fig. 3.4k) we infer a small region in velocity space composed of trapped electrons resulting from a small but positive parallel potential. The trapped-passing boundaries are indicated by the black-lines, and their shape is qualitatively different from those of Event A. This is because for Event B where  $B > B_{\infty}$  the mirror force works

opposite to  $\phi_{\parallel}$  and electrons with sufficiently high values of  $\mu$  will become passing. Fig. 3.4l) provides a perhaps clearer example of the compression, where a larger fraction of the electrons are trapped. In their journeys from the far upstream regions these electrons will have experienced a positive energy gain of  $(B-B_{\infty})\mu$ , so although B may locally be declining the fraction of trapped particles (heated by  $(B-B_{\infty})\mu$ ) increases leading to the observed increase in  $T_{\perp}$  as a function of increasing n/B (which is opposite the CGL predictions).

The case for compression is further supported by a closer look at the trapped-passing boundaries of distributions measured by MMS. In the context of the model, the half-ellipse form of the trapped-passing boundary is uniquely indicative of the case of  $n>n_\infty$  and  $B>B_\infty$ . Figure 3.5 shows electron distribution functions at times marked in Figure 3.6a) with the color range optimized to examine features in the thermal range. The phase space density has a clear reduction at the trapped-passing boundary, owing to a difference in dynamics between the two populations. The coincidence of the trapped-passing boundaries, given by  $\mathcal{E}-e\phi_{\parallel}-\mu B_{\infty}=0$ , and the location and shape of these reductions helps to constrain the upstream conditions [2]. For this closed curve trapped-passing boundary, we must have  $\phi_{\parallel}>0$  and  $B>B_{\infty}$ , again implying both the density and magnetic field strength are enhanced relative to their far upstream values where the passing electrons are sourced.

In this section, we have argued that the data for Event B is indicative of ongoing compression, but how might this be realized in the context of the reconnection event? The locations of both the bowshock and reconnection region relative to the magnetopause are not fixed, and the placement of these regions varies. The increased values of n and B may potentially be explained by a reconnection region that is relatively near the bow shock, where density and magnetic field are compressed, while the upstream populations reside in less compressed regions of the magnetosheath. Fig-

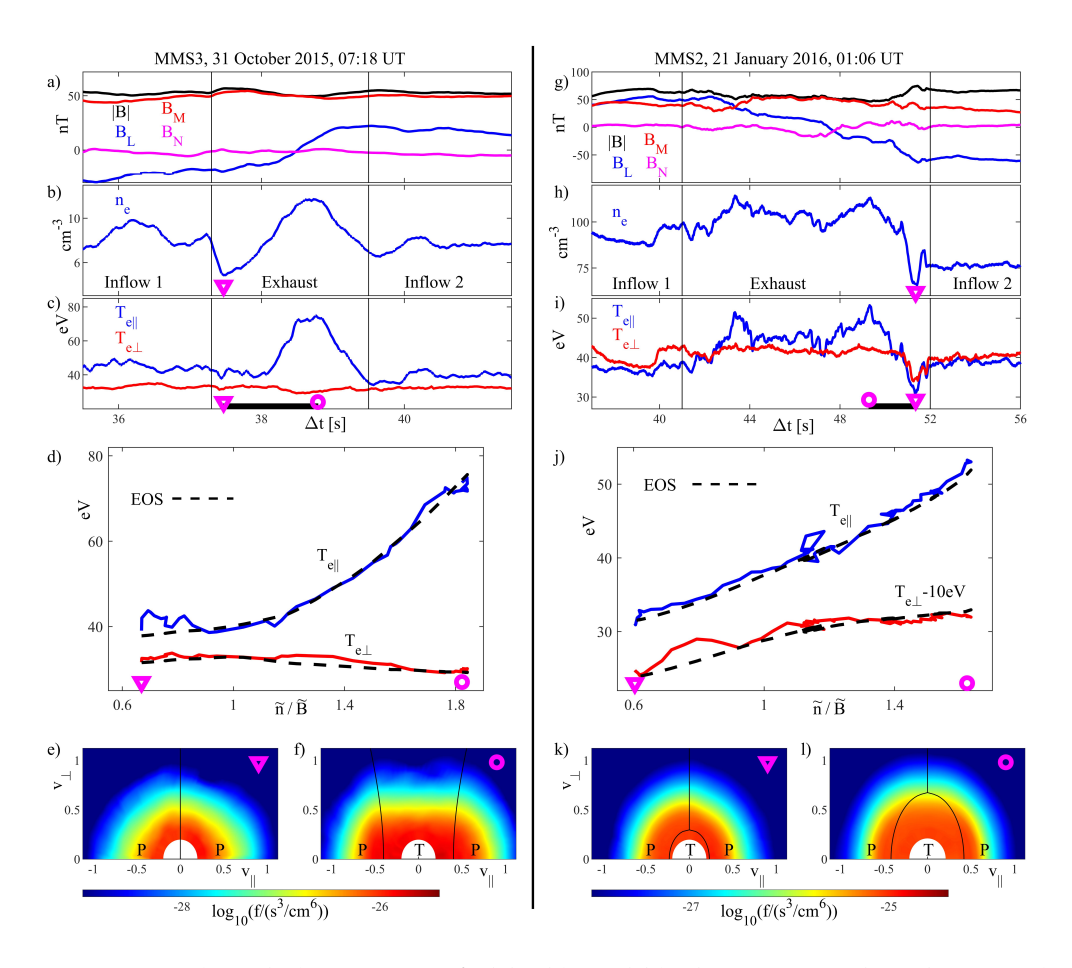


Figure 3.4: a) and g) Magnetic fields, b) and h) electron number density, c) and i) electron temperatures measured by MMS crossing the reconnecting layer. d) and j) show the variation of electron parallel and perpendicular temperatures with  $\tilde{n}/\tilde{B}$  in a region between an electron density cavity (marked by the magenta triangles) and peak (marked by the magenta circles), as well as the predictions of the EoS in the dashed lines. e) and k) show distributions measured in the density cavities, while f) and l) show the distributions at the density peaks. Even in the density cavity, the parallel potential for the 1/21/2016 event remains positive, which accounts for the increasing nature of the  $T_{e\perp}$  curve in j).

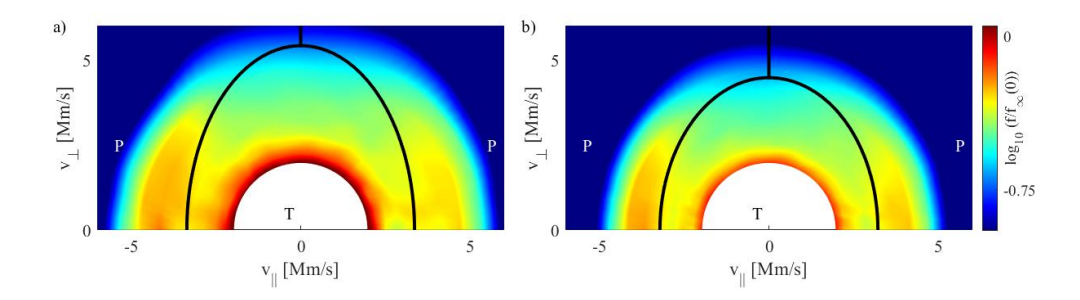


Figure 3.5: MMS2 distributions from a) Inflow 1 and b) Inflow 2, as marked in Fig. 3.6a), with the color scale set to emphasize the discontinuity at the trapped-passing boundary.

ure 3.2 illustrates how this may happen, while comparing to Event A, a case without compression. Event A and Event B differ in the presence of compression and the distance from the x-line MMS passed. In Event B, MMS crossed the reconnection exhaust further downstream of the x-line than the boundaries of most fully-kinetic simulations of magnetic reconnection.

# 3.4 Identifying Asymmetric Upstream Populations

In this section, we apply the EoS to Event B. Similar to the technique used in Ref. [105], we use separate upstream parameters for the two inflows. That study considered strongly asymmetric reconnection, and the dominant contribution to the exhaust a combination of the passing populations of the two inflows, which were identifiable based on regions of phase space. In contrast, in this limit of weak asymmetry that Event B resides in, the potential difference (and mirror force) developed between the high and low density sides is not strong enough to ensure that electron trapping is minimal in the exhausts. In fact, electron trapping is sizeable in the exhaust

	$n_{\infty}$ [cm $^{-3}$ ]	$B_{\infty}$ [nT]	$T_{e\perp\infty}$ [eV]	$T_{e\parallel\infty}$ / $T_{e\perp\infty}$
Inflow 1	47	30	28	0.9
Exhaust	41	29	30	1.0
Inflow 2	40	41	30	0.9

Table 3.1: Upstream parameters corresponding to the three upstream populations.

as required to explain the anisotropic pressures observed. Therefore, we choose to model the exhaust as having its own upstream population rather than an explicit prescription of the two inflows. The parameters determined for  $f_{\infty}$  can be seen in Table 3.1. Notably, the observed density and magnetic field strength stay above the upstream values for the duration of this crossing, as is consistent with the compressing picture presented in Section 3.5. This holds true for the observed temperatures as well, implying that the inflow plasma is heated by compression outside the reconnection region and is thus warmer than the external plasma sourcing the incoming passing electrons.

Figure 3.6b) shows the electron temperatures observed by MMS2 (colored lines) alongside the predictions of the EoS (black lines). The electron temperatures measured by MMS2 are colored according to the upstream population used in the EoS. The predictions of the EoS, which are determined by the inputs of Fig. 3.6a) and Table 3.1, mostly track  $T_{e\parallel}$  and  $T_{e\perp}$  well. In several areas, MMS data are colored as magenta rather than their upstream color. In these locations, there are significant deviations between the observed and predicted temperatures. This is mostly due to perpendicular heating related to local trapping that is not covered in the original model underlying the EoS, which will be further discussed in Section 3.5. This is also reflected in Figs. 3.6d-e), which show distribution functions measured by MMS2 at times marked in Fig. 3.6a) compared to the predictions of the theoretical model. While there are some subtle differences in the model and the data owing to the perpendicular heating,

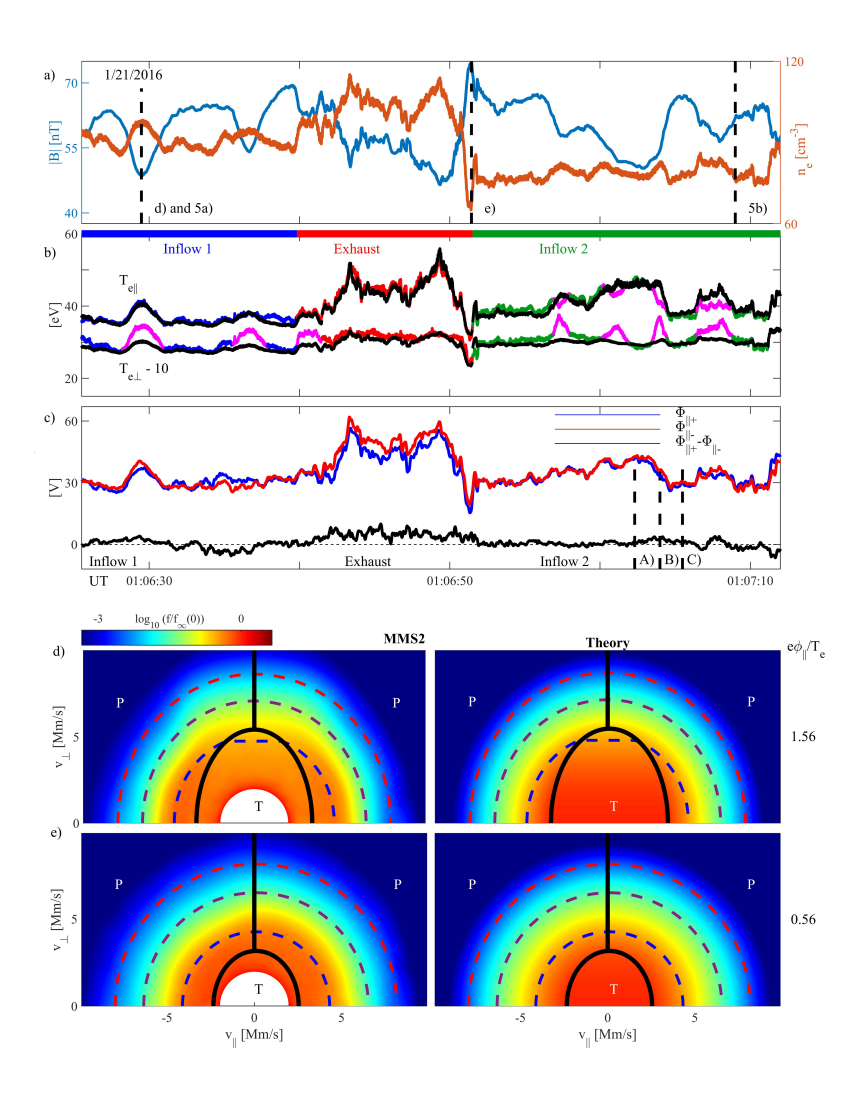


Figure 3.6: MMS2 measurements of a) density and magnetic field strength b)  $T_{e\parallel}$  and  $T_{e\perp}$  for the three upstream regions in color vs the EoS predictions in black. Magenta sections mark significant departures from the EoS, which can be attributed to locally trapped electrons. c)  $\phi_{\parallel\pm}$ , the parallel potential inferred in each direction along the magnetic field in blue and red, and the potential difference between the two in black. d) and e) are MMS2 (left) and the model of the EoS (right) electron distribution functions at the points marked in a), which correspond to the first inflow and the density cavity. Model contours and black trapped-passing boundaries are superposed.

the general form matches well.

The parallel potential is defined by integrating the parallel electric field along magnetic field lines out to the ambient plasma. As such, two different values for the parallel potential,  $\phi_{\parallel+}$  and  $\phi_{\parallel-}$  are obtained based on the direction (parallel or antiparallel to B) chosen for the integration. However, from theory [2], for nearly-symmetric reconnection configurations quasineutrality of the plasma imposes that that  $|\phi_{\parallel+}-\phi_{\parallel-}|$  is small, and the model in Eq. 3.3 simply uses  $\phi_{\parallel}\simeq\phi_{\parallel\pm}$ . Based on the energy shifts of the parallel and antiparallel streaming electrons in the detailed distributions provided by MMS, we can directly test this assumption and infer  $\phi_{\parallel+}$  and  $\phi_{\parallel-}$ . The result of this analysis is shown in Fig. 3.6c), which confirms that  $\phi_{\parallel+}\simeq\phi_{\parallel-}$ . This is borne out by the maximum of  $|\phi_{\parallel+}-\phi_{\parallel-}|$  being about an order of magnitude smaller than  $|\phi_{\parallel+}+\phi_{\parallel-}|$ , and the variation of both within the exhaust is considerably larger than the difference between the two.

Again, given the moderately asymmetric reconnection setup, each inflow has a different upstream distribution, and mixing of the populations occurs in the outflow, which we have treated as a third set of upstream conditions. These regions are clearly discernible as three distinct characteristics in  $\left((n/B)^2, T_{\parallel}\right)$  space which correspond to the two inflows and the mixed exhaust, as seen in Fig. 3.7a). As could be expected, the exhaust characteristic lies between those of the two inflows. This three-pronged characteristic could potentially be used as an identifier for reconnection events with asymmetric inflow populations.

The analysis of Ref. [97] noted the minima in observed electron temperatures within the density cavity at the separatrix (the point marked e) in Fig. 3.6a) with corresponding measured and theoretical distributions in Fig. 3.6e)). Because the observed temperature is lower than the temperature of the plasma surrounding the density cavity, it was suggested that (in the terminology of the present work) a negative  $\phi_{\parallel}$  is the cause of

the apparent cooling. However, cooling by electric fields is not physical, as it is not consistent with the standard Boltzmann response. In fact, the effect of a negative  $\phi_{\parallel}$  is directly illustrated in Event A, where, as evident in Fig. 3.4d), only the electron density (and not  $T_{\parallel}$ ) is sensitive to  $\phi_{\parallel}$  in the range where  $\phi_{\parallel}<0$ . The apparent cooling is in fact not cooling; rather, the present analysis of Event B shows that compared to  $T_{\infty}$  of the far away regions (from which the passing electrons are sourced),  $T_{\parallel}$  within the cavity is also heated by  $\phi_{\parallel}>0$ , but the heating is smaller than that of the immediate vicinity measured by MMS, where the larger values of n necessitate a larger  $\phi_{\parallel}$  under the EoS and thus also larger parallel heating of the electrons. As such, the electrons have been subject to parallel heating along the entire MMS trajectory of Event B, but less so within the density cavity, where reduced values  $\phi_{\parallel}$  are required to maintain quasineutrality. Thus, the apparent cooling of the density cavity provides further support for our interpretation of large scale compression.

While the parallel temperature measurements are quite well characterized by the EoS, in certain regions of both inflows the perpendicular temperature measurements diverge from the EoS. Fig. 3.6b) shows the predictions of the EoS for the perpendicular temperatures observed by MMS. To more clearly separate the populations, different offsets (of 0, 10 and 20 eV) have been applied to the traces. Section 3.5 below we will discuss the cause for the discrepancy between the EoS and the particular regions of enhanced values of  $T_{\perp}$ , as marked by magenta in Fig. 3.6. These regions where the EoS become inaccurate coincide with local dips in B associated with local trapping, introducing new physical effects not considered in the model in Eq. 3.3.

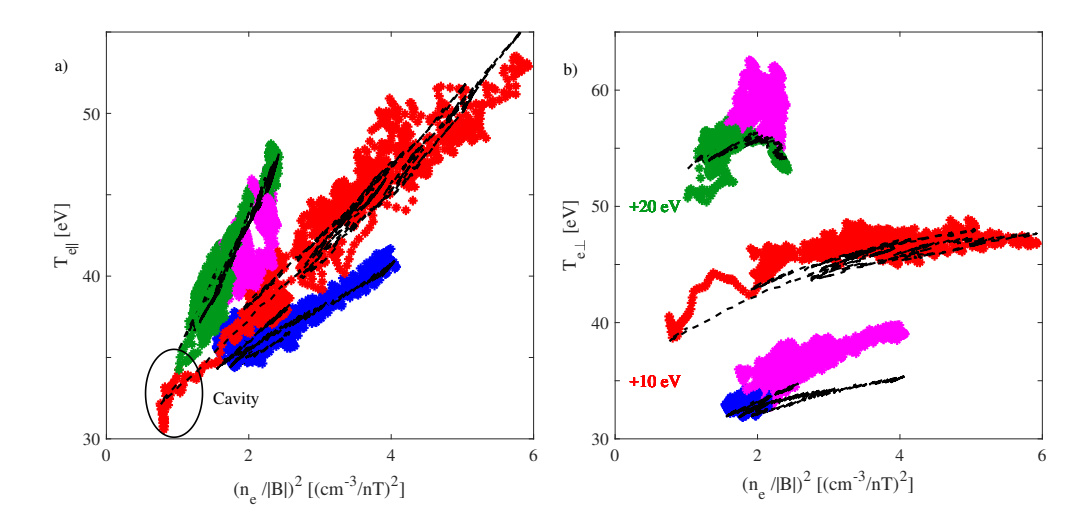


Figure 3.7: a) MMS2 measurements of distinct characteristics in  $(n^2/B^2, T_{e\parallel})$  space for the two inflows and the exhaust. Black dashed lines correspond to the prediction of the EoS for each branch, while starred points are MMS2 measurements. b) The same plots for  $T_{e\perp}$ , with offsets for each exhaust to separate the data. Magenta regions, as indicated in Fig. 3.6b), do not follow the EoS due to heating by local trapping.

### 3.5 Perpendicular Heating of Locally Trapped Electrons

In Section 3.3, it was established that Event B occurred in a region undergoing compression. Further, at the end of Section 3.4, we noted several regions where the EoS significantly underestimate the perpendicular electron temperature. While not immediately obvious, the perpendicular heating can be seen in Figure 3.7 d), which shows the distribution function measured by MMS2 compared with the theoretical model. In the small parallel velocity portions of the passing populations, the phase space density observed by MMS is slightly enhanced relative to the model.

Magnetic field compression can provide a source of perpendicular heating in the form of nonzero  $\int \mu \partial B/\partial t \,dt$  along an electron orbit. The

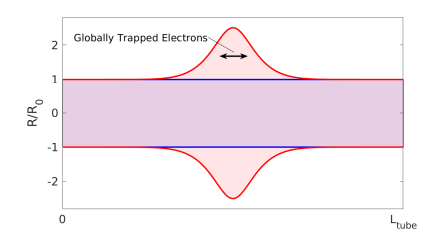
original model is derived in the adiabatic limit of infinitely fast electron thermal speed (and thus zero transit time), causing the integral to go to zero for passing particles. In this limit of fast electron transit, compression of the magnetic field causes well-magnetized electrons coming from the upstream distribution to sacrifice their parallel velocity to maintain their magnetic moments, thereby increasing the transit time. Furthermore, as we discussed above, for  $B>B_{\infty}$  the passing regions include electrons with  $v_{\parallel}=0$  which violate the assumption of a short transit time. In addition, local trapping in local regions of low magnetic fields can cause confinement and further violation of the fast transit-time approximation. We will see that both of these finite transit time effects most strongly apply to electrons with small  $v_{\parallel}$ , necessitating an additional energy shift  $\Delta \mathcal{E}$  in Eq. 3.4 and enhancing the phase space density where  $v_{\parallel} \ll v$ .

To capture the effects of local trapping, we extend the model of Refs. [2, 81] described in Eq. 3.3 to predict electron distributions of the form

$$f(\mathbf{x}, \mathbf{v}) = \begin{cases} f_{\infty}(0, \mu B_{\infty}) & \text{trapped} \\ f_{\infty}(\mathcal{E} - e\phi_{\parallel} - \mu B_{\infty} - \Delta \mathcal{E}, \mu B_{\infty}) & \text{passing} \end{cases}$$
(3.4)

We will show that this expression is consistent with the distributions recorded by MMS for which a detailed analysis allows us to estimate the new term  $\Delta \mathcal{E}$ . It should be noted, however, that there exists no formal dependence of  $\Delta \mathcal{E}$  on n and B, and it is therefore not possible to incorporate the effect of  $\Delta \mathcal{E}$  into an improved generalized version of the EoS.

Figure 3.8 illustrates how local magnetic trapping can enter into a model of a flux tube undergoing broad scale compression. In the typical reconnection case, the flux tube expands as it approaches the reconnection region, and electrons can become magnetically trapped in the expanded regions. These electrons are trapped in a global sense. In the compressing case, the flux tube enters the compression in some initial state, which may



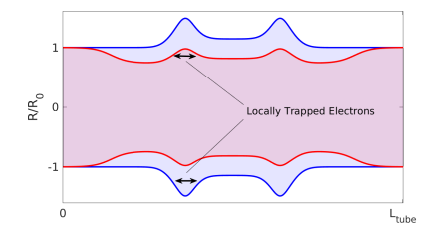


Figure 3.8: Examples of flux tube evolution in a typical reconection scenario and the compressing scenario. In the typical scenario, the flux tube expands as it approaches the x-point, allowing for electrons to become magnetically trapped in the global sense. In the compressing case, we consider the initial flux tube to be perturbed to have some portions expanded, again allowing for magnetic trapping. As compression acts on the flux tube, these regions are compressed relative to the upstream ends of the flux tube, but remain local minima in the magnetic field strength. As such, particles that were trapped in the initially expanded regions may remained locally trapped, experiencing perpendicular energization in the compression process.

have some local expansions in the flux tube in which electrons may be trapped. Once the compression starts, the magnetic field is increased on a broad scale, and the portions of the flux tube in the compressing region are compacted. After the compression, the regions that were once expanded may be more compressed than the upstream ends of the flux tube. This implies that the electrons that began trapped in these regions are no longer magnetically trapped in a global sense; however, if the compression is relatively uniform about the initial trapping regions, the electrons will remain locally trapped and will experience heating by  $\mu \partial B/\partial t$  over the course of the compression.

Remaining agnostic about the exact dynamics of the heating caused from a finite electron travel time, we can surmise the energization that an electron has gone through to reach a certain point in the phase space,  $\Delta \mathcal{E} = \mu \int \partial B/\partial t(\mathbf{x}(t)) \mathrm{d}t$ . An electron that is trapped over the duration of

the compression will experience perpendicular energy gain  $\Delta \mathcal{E} = \mu \Delta B = \mathcal{E}_{\perp} \Delta B/B$ . This can be viewed as a bounding case for an orbit that experiences the full effect of the compression. To infer  $\Delta \mathcal{E}$  from MMS data, we can determine the  $\Delta \mathcal{E}(\mathcal{E},\theta)$ , where  $\theta$  is the electron pitch angle, that makes the new model of Eq. 3.4 match the distributions measured by MMS.

We note that in both the original and the extended model, electrons streaming parallel to the magnetic field lines have their energies altered by only  $e\phi_{\parallel}$ . This means that the distortion from the upstream distribution will be small for particles traveling nearly parallel to the magnetic field lines. As such, the upstream distribution was chosen to match the parallel portion of the measured distribution being offset by  $e\phi_{\parallel}$ , with the lower energies set to match MMS observations and a polynomial fit of degree 2 in velocity for the tail of the logarithmic distribution.

With an explicit form for the upstream distribution, we then numerically invert Eq. 3.4 to solve for  $\Delta \mathcal{E}(\mathcal{E},\theta)$ . Figs. 3.9 a-c) show distribution functions measured by MMS2 at times labeled in Fig. 3.6c), while Figs. 3.9 e-g) show the inferred value of  $\Delta \mathcal{E}/\mathcal{E}$  as a function of pitch angle and energy. The base model distribution with  $\Delta \mathcal{E}=0$  for time C is shown in Fig. 3.9d). The MMS distribution displays a considerable boost in phase space density relative to the base model, which is particularly noticeable for energies above  $169\,\mathrm{eV}$ .

The energization  $\Delta \mathcal{E}$  can be viewed as a function of time as well. Fig. 3.10 shows  $\Delta \mathcal{E}/\mathcal{E}_{\perp}$  as a function of time and pitch angle for four separate energy bins measured by MMS. As expected, the magenta regions of Fig. 3.6b) correspond to times with strong  $\Delta \mathcal{E}/\mathcal{E}_{\perp}$ . The red and black contours represent the pitch angle at which an electron would reflect upon encountering a barrier of  $62\,\mathrm{nT}$  and  $75\,\mathrm{nT}$ , respectively. In other words, electrons inside these contours are locally magnetically trapped if the maximum value of B along the flux tube exceeds the aforementioned value. Notably, the largest values of  $\Delta \mathcal{E}/\mathcal{E}_{\perp}$  are encircled by the red con-

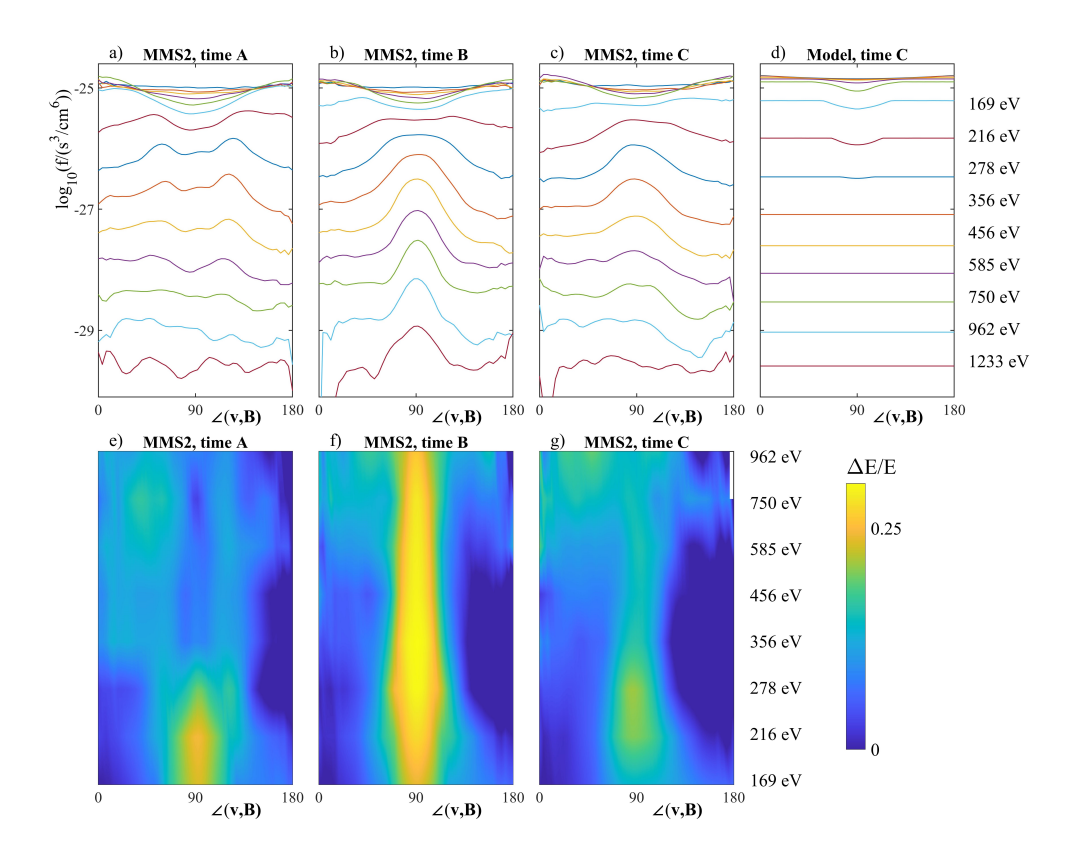


Figure 3.9: a-c) Electron distributions measured by MMS2 at times A, B, and C marked in Fig. 3.6c), respectively. d) Electron distribution function predicted by Eq. 3.4 with  $\Delta \mathcal{E} = 0$  at time C. e-f) Inferred energy gain  $\Delta \mathcal{E}/\mathcal{E}$  as a function of pitch angle and energy for times A-C respectively.

tours, where electrons are most deeply trapped and evidently confined during the full compression process. Furthermore, for the deeply trapped electrons in Inflow 2, the peak value of  $(\mathcal{E}_{\perp} + \Delta \mathcal{E})/\mathcal{E}_{\perp} \approx 1.35$  corresponds almost exactly to  $B/B_{\infty} \approx 1.34$ , the value expected for electrons which have been trapped for the full compression of B. This implies that local trapping in a region undergoing compression is responsible for the regions of strong perpendicular energization observed.

In Fig. 3.10 we observe regions encircled by the red contour (indicative

of low B) but which are not associated with large values of  $\Delta \mathcal{E}$ . An example is the time point marked by A with the corresponding distribution and inferred  $\Delta \mathcal{E}$  displayed in Figs. 3.9a) and e), respectively. The distributions can be explained by the trapped portions of the electron distributions being lost. In fact, distributions with a form similar to those with large  $\Delta \mathcal{E}$  observed in Fig. 3.9f) have been found to cause instabilities [106], which in turn could help scatter and drain the deeply trapped populations. Interestingly, throughout the reconnection exhaust marked in Fig. 3.10 we observed  $\Delta \mathcal{E}/\mathcal{E}_{\perp} < 0.1$ , suggesting that the confinement of the locally trapped populations is lost. As a consequence, for the present event the electron populations which are most significantly heated are observed within the regions of deeply trapped electrons that exist in the inflows outside the reconnection exhaust.

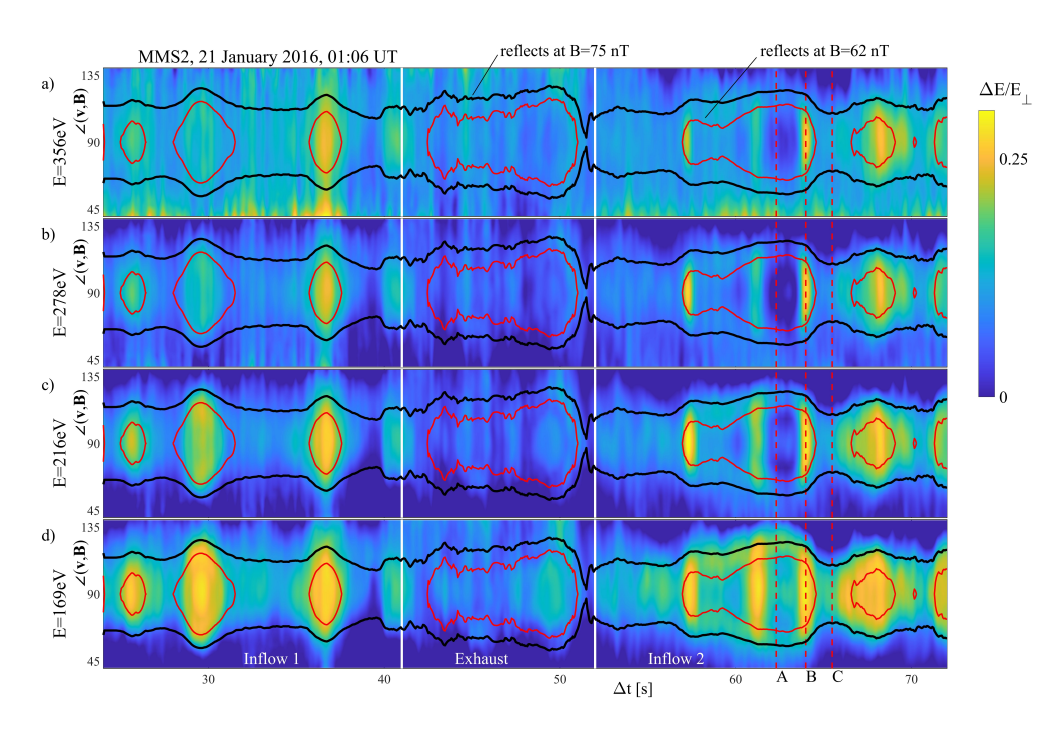


Figure 3.10: a-d) Inferred energization  $\Delta \mathcal{E}/\mathcal{E}_{\perp}$  as a function of pitch angle and time for various energy bins measured by MMS2. The red and black contours represent the pitch angle at which an electron will reflect in a magnetic field of  $62\,\mathrm{nT}$  and  $75\,\mathrm{nT}$ , respectively.

#### 3.6 Discussion and Conclusion

In summary, we have revisited some of the physics governing guide-field reconnection, including the generation of an in-plane electrostatic potential to maintain quasineutrality where the reconnecting electric field is aligned with a guide field. This potential is responsible for the well-known quadrupolar density perturbation in guide-field reconnection. We have also demonstrated the validity of the EoS for guide-field reconnection with  $in\ situ$  MMS observations of magnetic reconnection for regions far from ( $\sim 100\ d_i$ ) the x-line, which is significantly farther downstream than the EoS had previously been validated with MMS [84] and particle-in-cell

(PIC) simulation [41] data. Furthermore, we note that slightly asymmetric reconnection creates distinct characteristics in  $(T_{\parallel},n/B)$  space corresponding to the reconnection exhaust and each inflow region. We suspect the three-pronged form of Fig. 3.7a) to be general to weakly asymmetric guidefield reconnection, and as such, this sort of plot could serve to identify exhaust crossings in MMS data.

Additionally, we have extended the model to include first-order effects of local trapping, which match the observed distribution function and provide an improved understanding of the dynamics that permit perpendicular electron energization in regions of plasma compression. The energy gain by the compression and the original EoS model are both reversible. As such, "heating" may not be the correct word to describe the energy gains from this model, absent collisional effects. The plasma could hypothetically return to the upstream conditions and the energy gain would be lost, but this event shows that the energy gains are still present deep into the exhaust. We note that the EoS has been successfully implemented as an electron fluid closure for hybrid simulations with PIC ions [46] and in two-fluid simulations [43]. For the case of some MMS observations, such a hybrid simulation has better reproduced observation than fully-kinetic PIC simulations at reduced values of  $m_i/m_e$  [84]; this highlights how the EoS closure will be useful to numerical simulation of large scale plasma configurations subject to magnetic reconnection in reproducing important aspects of the reconnection process at far lower computational cost.

As a final note, we point out that the physics described by the EoS can satisfy all three requirements of an electron heating mechanism put forth in Ref. [89] for events with guide fields strong enough to keep electrons magnetized in the reconnection exhaust and  $\beta_e > \sqrt{m_e/m_i} \approx 0.02$  large enough to avoid nonadiabatic parallel dynamics, as required by the model. The heating provided by the model is clearly anisotropic in fa-

vor of  $T_{e\parallel}$ . Furthermore, in combination with roughly steady-state force balance across the exhaust, the model has been shown to predict similar scalings for  $\Delta T_e$  in the exhaust for a variety of guide field regimes [48, 84] as the observed scalings of Ref. [3]. The heating predicted by the EoS in these scalings is primarily regulated by the density and magnetic field strength required in the exhaust for force balance across the layer. So long as the upstream inflows are relatively uniform in the direction of the reconnecting field, the heating should have little dependence on the distance from the x-line. As such, the EoS satisfies the observational constraints of Refs. [3, 89] for the electron heating mechanism for magnetic reconnection in the moderate  $\beta_e$  guide-field regime.

#### 4 A Drift-Kinetic Method for Obtaining Gradients in Plasma Properties from Single-Point Measurements

#### 4.1 Introduction

The properties of the plasma in the Earth's magnetosphere as well as the connection between large scale plasma dynamics on the Sun and the near Earth environment have been studied intensely over the past decades using increasingly sophisticated spacecraft. With a few exceptions, most of these studies have been carried out through the use of a single spacecraft. A significant and fundamental problem to interpreting spacecraft measurements is that the relative speed between large-scale magnetic structures and the spacecraft is generally not known. This often makes it impossible to characterize the length scales of the dynamical plasma structures encountered because it is not possible to distinguish time variation from spatial variation. The problem can be overcome by applying several spacecraft flying in close formation [107, 108]; length scales on the order of the spacecraft separation can then be determined accurately.

The resolution of fine scales is crucial to the understanding of many processes in collisionless plasma physics. Of particular interest, in magnetic reconnection the thickness of the current layer can be on the electron kinetic scale, while various terms in the generalized Ohm's law, which can be written as

$$\mathbf{E} + \mathbf{v} \times \mathbf{B} = \eta \mathbf{j} + \frac{1}{ne} \left( \mathbf{j} \times \mathbf{B} - \nabla \cdot \mathbf{p}_e \right) + \frac{m_e}{ne^2} \frac{d\mathbf{j}}{dt} \quad , \tag{4.1}$$

decouple at different scales; for example,  $\nabla \cdot \mathbf{p}_e$  becomes important for gradient scales on the order of the thermal electron Larmor radius  $\rho_e = m_e v_{th}/eB$  or electron skin depth  $d_e = c/\omega_{pe}$ . Thus, characterizing the terms

down to the kinetic scale would require a tight spacecraft formation to fully resolve, which would also sacrifice overall coverage. Determining local gradients go a long way towards interpreting the overall structure of a current layer.

In this chapter, we develop new methods that allow length scales of plasma structures to be determined at spatial scales as small as the electron Larmor radius  $\rho_e \sim \sqrt{\beta_e} d_e$ , allowing for  $d_e$  scale gradients to be accurately characterized if  $\beta_e$  is not too large. Our methods could be implemented using the full three dimensional electron distribution function, which is now available with sufficiently fast time resolution from the Fast Plasma Investigation (FPI) instrumentation suite of NASA's Magnetospheric Multiscale (MMS) mission [49], and will likely be available to future spacecraft missions. The methods make a connection between the apparent agyrotropy of magnetized distributions and gradients in plasma properties perpendicular to the magnetic field lines.

Agyrotropy is the breaking of the symmetry of a distribution function about the magnetic field line, and it is commonly used as a signature for the demagnetization of electrons near the x-line in magnetic reconnection [109]. In principle, in a well-magnetized plasma, the fast motion of the gyroorbit will cause the distribution to be constant about its nearly circular trajectory; therefore, a departure from gyrotropy is often implied to be the result of the demagnetization of the particle species. For the electrons in reconnection, this would happen in the electron diffusion region. Several measures of agyrotropy (sometimes called nongyrotropy) have been developed [109–111], generally measuring the deviation from a diagonal pressure tensor with entries  $(p_{||}, p_{\perp}, p_{\perp})$  in a magnetic field aligned basis. In these measures, agyrotropy is strong not only in the electron diffusion region, but also along the topological boundaries formed by the separatrices. Thus, in these measures, agyrotropy is not a unique signature of the electron diffusion region. The agyrotropy associated with the separatrices

is based on a transition between two topological regions on the scale of a Larmor radius. While electron distributions measured at the separatrix are strongly agyrotropic in the frame of the reconnection region, taking the drift-kinetic approach of measuring  $f(\mathbf{x}_{gc})$  to be the phase space density of particles with guiding centers at  $\mathbf{x}_{gc} = \mathbf{x} - \boldsymbol{\rho}(\mathbf{v})$  rather than current position at  $\mathbf{x}$  can in many cases lead to gyrotropic distributions. This tells the story of separate well-magnetized plasma populations interpenetrating at the depth of a Larmor radius, sometimes resulting in crescent-type distributions [55].

Recent observational work on magnetic reconnection has emphasized these agyrotropic crescent distributions. For example, Burch et al. [54] found the presence of crescent-shaped distributions, both in the perpendicular plane and a parallel-perpendicular plane. This sort of agyrotropic distribution is thought to be a hallmark of the electron diffusion region. However, as noted above, crescent shaped distributions can also a result of crossing the separatrix, where large density gradients exist in asymmetric reconnection. These highly-agyrotropic distributions can be seen as hallmarks of strong gradients in the reconnection geometry. In this chapter, we will explicitly link the agyrotropy of the electron distribution function with spatial gradients. Section 4.2 contains an analysis of the effects of density gradients on the commonly-used measures of agyrotropy. In Section 4.3, we build up a framework to characterize length scales smaller than the separation distance between spacecraft, then verify it using data from several VPIC fully-kinetic simulations in Section 4.4, demonstrating that this method can accurately characterize gradients in density and pressure on the scale of  $\rho_e$ . The chapter concludes with a discussion in Section 4.5.

# 4.2 Apparent Agyrotropy of Simple Distributions that are Gyrotropic in the Guiding Center Frame

As mentioned in Section 4.1, strongly agyrotropic distributions are often associated with regions where plasma properties vary sharply. Previous work has also noted the relationship between agyrotropy and gradients at the scale of the Larmor radius [112, 113], but has focused primarily on reconnection scenarios rather than simple model equilibria with density gradients. While agyrotropy can arise from several factors in the drift-kinetic limit, here we focus in on a model where the density gradient is the primary contributor. In this section, we compute measures of agyrotropy for a simple guiding center distribution with a spatially varying density. We choose the simplest magnetized guiding center distribution with perpendicular density gradients.

$$\bar{f} = \left(\frac{m}{2\pi T}\right)^{\frac{3}{2}} (n_0 + x\nabla n) e^{-\frac{m|\mathbf{v}|^2}{2T}}$$
 (4.2)

We choose  $\mathbf{B}=B\hat{z}$  and T to be constant for simplicity. We will not have an electric field in this example, but it can be shown that an arbitrary perpendicular electric field will not change the results of the calculation of the agyrotropy parameters, though the intermediate steps will be more complicated and include a velocity shift to the  $\mathbf{E} \times \mathbf{B}$  frame. An electric field of  $\mathbf{E} = T\nabla n/(nqB)\hat{x}$  is important, as it will allow the species to be in fluid and drift-kinetic equilibrium. We note that the distribution of Eq. 2 is binned by the location of the guiding center of the particle rather than the particle's instantaneous position, as a spacecraft will typically measure. As such, to evaluate the local distribution function  $f(\mathbf{x}, \mathbf{v})$ , we must account for the shift of the vector Larmor radius  $\rho$ . We now calculate

$$f = \bar{f}(\mathbf{x} - \boldsymbol{\rho}) = \left(\frac{m}{2\pi T}\right)^{\frac{3}{2}} \left(n_0 + \nabla n \left(x - \frac{mv_y}{qB}\right)\right) e^{-\frac{m|\mathbf{v}|^2}{2T}} \quad . \tag{4.3}$$

Notably, in this toy model f becomes negative for particles with large enough  $v_y$ . This means that particles with larger Larmor radii than the gradient scale will be represented by an unphysical phase space density due to the simplified form of Eq. 2, but this is a negligible contribution for gradient scales that are small relative to the thermal Larmor radius. Having an analytic form of the distribution function allows us to take moments at x=0. It can easily be seen that the density moment gives us  $n=n_0$ . The bulk velocity moment reflects the diamagnetic drift.

$$\mathbf{u} = -\frac{T\nabla n}{nqB}\hat{y} \tag{4.4}$$

With this, the pressure tensor can be straightforwardly calculated as

$$\mathbf{P} = \left(\frac{m}{2\pi T}\right)^{\frac{3}{2}} \int \left(\mathbf{v} - \mathbf{u}\right) \left(\mathbf{v} - \mathbf{u}\right) \left(n_0 - \frac{mv_y}{qB} \nabla n\right) e^{-\frac{m|\mathbf{v}|^2}{2T}} d^3 v \tag{4.5}$$

$$= n_0 T \left( \mathbf{I} - mT \left( \frac{\nabla n}{n_0 qB} \right)^2 \hat{y} \hat{y} \right) . \tag{4.6}$$

Simple symmetry arguments show that off-diagonal elements are zero; however, the tensor is still not gyrotropic, as the perpendicular pressures are not identical. If we define  $L_{\nabla} = |n_0/\nabla n|$  and  $\rho_{th} = |mv_{th}/qB|$ , we can define  $\xi = \rho_{th}/L_{\nabla}$  as the ratio between the gradient scale and the Larmor scale, and define all of our agyrotropy measures in terms of this parameter.

We will calculate  $A\mathcal{O}_e/2$  [109],  $D_{ng}$  [110], and  $\sqrt{Q}$  [111]. All of these parameters measure agyrotropy associated with this gradient, and gyrotropic distributions will return a value of 0.  $A\mathcal{O}_e/2$  and  $\sqrt{Q}$  take the value of 1 for a maximally agyrotropic distribution, though  $D_{ng}$  has a

different normalization that is dependent on  $T_{||}/T_{\perp}$ .

$$A\mathcal{O}_e/2 = \frac{\xi^2}{2 + \xi^2} \tag{4.7}$$

$$D_{ng} = \frac{\sqrt{2}\xi^2}{3 + \xi^2} \tag{4.8}$$

$$D_{ng} = \frac{\sqrt{2}\xi^2}{3+\xi^2}$$

$$\sqrt{Q} = \frac{\xi^2}{\sqrt{(2-\xi^2)(6-\xi^2)}}$$
(4.8)

 $\sqrt{Q}$  clearly has issues for  $\xi > 1$ , but that is a result of the nonphysical behavior of this model distribution in that regime (as can easily be seen in Eq. 4.6). All three measures reduce to zero in the gradient-free limit. A plot of  $A\mathcal{O}_e/2$  and  $\sqrt{Q}$  can be seen in Fig. 4.1.  $\sqrt{Q}$  is less sensitive to small gradients than the other two measures, but all three measures are increasing functions of the strength of the density gradient, even though the guiding center distribution is perfectly isotropic. This allows for the possibility of determining unknown gradients through a measure of the agyrotropy of a distribution function, though more factors will be accounted for in the treatment of the following section.

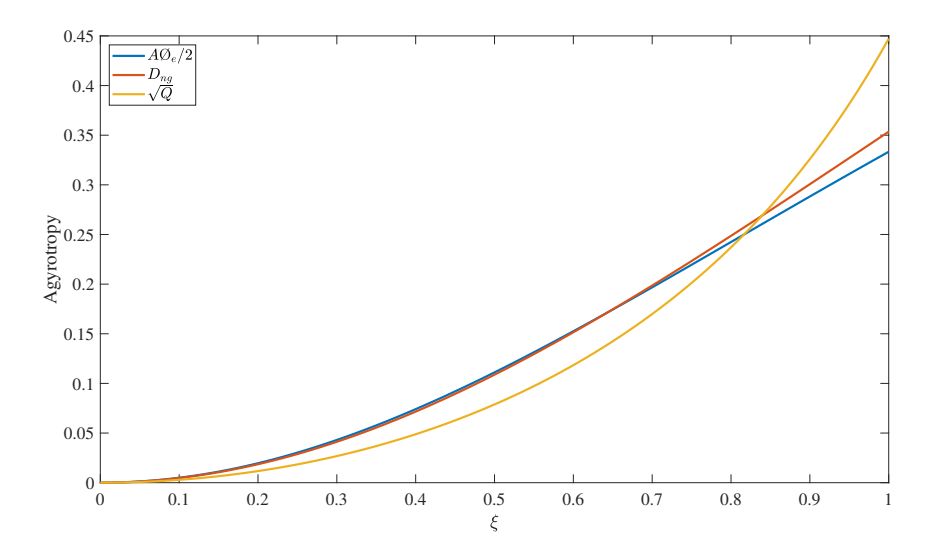


Figure 4.1:  $A\mathcal{O}_e/2$  and  $\sqrt{Q}$  plotted against the ratio of the Larmor scale to the gradient scale,  $\xi$ , for the relevant range.

# 4.3 Theoretical Basis for Length Scale Characterization

In the previous section, we considered a simple example and showed that agyrotropy develops as a result of gradients in the distribution function. In this section, we will consider more general geometries and rigorously show how gradient scales can be inferred through measurements of the distribution function. Before deriving the model in detail, we first provide a heuristic description of how the plasma length scales can be obtained from electron distributions measured by a single spacecraft. Fig. 4.2 illustrates a model geometry of a spacecraft sampling the electron distribution f. We assume that there is a gradient in f pointing in the negative x direction. With B in the negative x-direction it follows that the flux of electrons observed in the positive x-direction will be enhanced while the flux received from the negative x-direction is reduced. Furthermore, considering the

separation of the respective guiding centers  $(2\rho_e)$  in Fig. 4.2, it is clear that the relative difference in these fluxes must be given by  $2\rho_e\nabla f/f$ , where  $\rho_e$  is the electron Larmor radius for the energy considered. This anisotropy of particle flux is the origin of the diamagnetic drift.

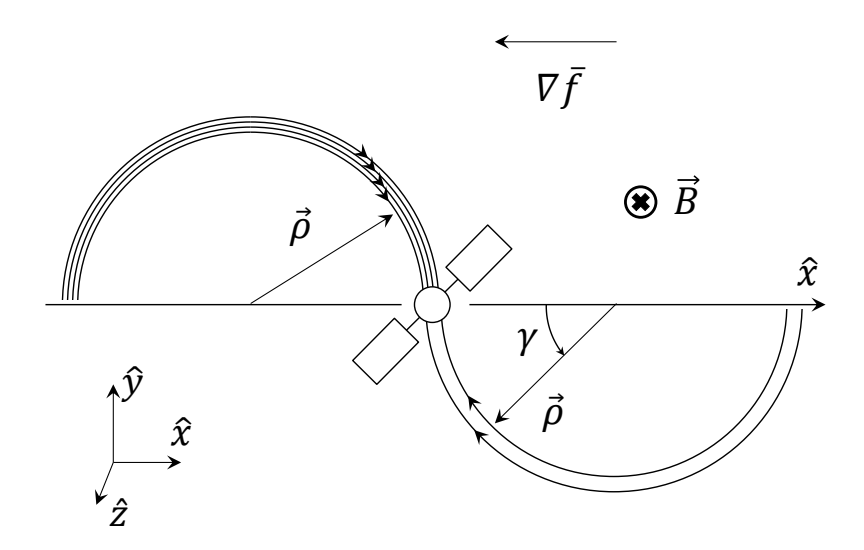


Figure 4.2: Illustration of how a single spacecraft sampling the electron distribution can be applied for characterizing the gradient in the gyrotropic electron distribution function  $\nabla \bar{f}$ .

The approach outlined with the heuristic arguments above is made concrete in this chapter. We can rigorously derive expressions for perpendicular distribution function gradients starting from the kinetic Vlasov equation governing collisionless plasma. Although we are primarily interested in properties of the electron distribution, we will derive expressions for a general species in the drift-kinetic limit. By inserting the appropriate mass, charge, and distibution, the electron equations are easily recovered. We begin by noting, as is discussed in great detail in the book by Hazeltine and Meiss [114], that in the drift-kinetic limit the Vlasov equation imposes that the first-order expectation of the variation from gyrotropy  $\tilde{f}$  can be

expressed as:

$$\tilde{f}(\mathbf{x}, U, \mu, \gamma, t) = \boldsymbol{\rho} \cdot \left[ q \frac{\partial \mathbf{A}}{\partial t} \frac{\partial \bar{f}}{\partial U} - q \left( \mathbf{b} \times \mathbf{v}_D \right) \frac{\partial \bar{f}}{\partial \mu} - \boldsymbol{\nabla} \bar{f} \right] 
+ \frac{v_{\parallel} \mu}{\Omega_s} \frac{\partial \bar{f}}{\partial \mu} \left( \hat{\boldsymbol{\rho}} \hat{\mathbf{v}}_{\perp} : \boldsymbol{\nabla} \mathbf{b} - \frac{1}{2} \mathbf{b} \cdot \boldsymbol{\nabla} \times \mathbf{b} \right) \quad . \quad (4.10)$$

Here  $\bar{f}=\bar{f}(\mathbf{x},U,\mu,t)$  is the gyro-averaged distribution, U is total particle energy (kinetic plus an electrostatic potential),  $\Omega_s=qB/m$  is the signed cyclotron frequency,  $\mu$  is the (first adiabatic invariant) magnetic moment,  $\gamma$  is the gyrophase such that  $\boldsymbol{\rho}=\mathbf{b}\times\mathbf{v}/\Omega_s=\rho(\mathbf{e}_{\perp 1}\sin\gamma+\mathbf{e}_{\perp 2}\cos\gamma)$ , with  $(\mathbf{b},\mathbf{e}_{\perp 1},\mathbf{e}_{\perp 2})$  forming a right-handed local coordinate system, and

$$\mathbf{v}_{D} = \frac{\mathbf{E} \times \mathbf{B}}{B^{2}} + \frac{1}{\Omega_{s}} \mathbf{b} \times \left( \frac{\mu}{m} \mathbf{\nabla} B + v_{\parallel}^{2} (\mathbf{b} \cdot \mathbf{\nabla}) \mathbf{b} + v_{\parallel} \frac{\partial \mathbf{b}}{\partial t} \right)$$
(4.11)

is the drift velocity expected for a particle at each location in phase space. We are most interested in the gradient information that can be recovered from an individual spacecraft that bins the distribution as a function of velocity rather than the adiabatic invariants. Thus, we note that the change in coordinates to  $(v_\parallel,v_\perp)$  space provides a mixing between coordinate and velocity spaces,

$$\nabla_{U,\mu} = \nabla_{v_{\parallel},v_{\perp}} - \nabla \mu \frac{\partial}{\partial \mu} - \nabla U \frac{\partial}{\partial U} \quad . \tag{4.12}$$

Importantly, this eliminates any contribution to  $\tilde{f}$  from the  $\nabla B$  drift and alters the inductive electric field in Eq. 4.10 to be the full electric field.

By multiplying each side of Eq. 4.10 by the vector Larmor radius  $\rho$  and integrating over the gyrophase  $\gamma$ , we find the perpendicular component of the gradient of  $\bar{f}$ :

$$\nabla_{\!\!\perp} \bar{f} = -q \mathbf{E}_{\perp} \frac{\partial \bar{f}}{\partial \mathcal{E}} - q \left( \mathbf{b} \times \mathbf{v}_D \right) \frac{\partial \bar{f}}{\partial \mu} - \frac{1}{\pi \rho^2} \int_0^{2\pi} \boldsymbol{\rho} f \, \mathrm{d}\gamma \tag{4.13}$$

Notably, the terms not dotted into the gyroradius in Eq. 4.10 integrate out to zero. It can also be shown that the  $\mathbf{E} \times \mathbf{B}$  drift term in Eq. 4.10 combines with the  $\mathbf{E}_{\perp}$  term to form  $e\mathbf{E}_{\perp}\partial\bar{f}/\partial\mathcal{E}_{\perp}$  in an  $(\mathcal{E}_{\perp},\mathcal{E}_{\parallel})$  basis:

$$\nabla_{\perp} \bar{f} = -q \mathbf{E}_{\perp} \frac{\partial \bar{f}}{\partial \mathcal{E}_{\perp}} + \left( m v_{\parallel}^{2} (\mathbf{b} \cdot \nabla) \mathbf{b} + m v_{\parallel} \frac{\partial \mathbf{b}}{\partial t} \right) \left( \frac{\partial \bar{f}}{\partial \mathcal{E}_{\perp}} - \frac{\partial \bar{f}}{\partial \mathcal{E}_{\parallel}} \right) - \frac{1}{\pi \rho^{2}} \int_{0}^{2\pi} \boldsymbol{\rho} f d\gamma. \quad (4.14)$$

While this expression fully describes  $\nabla_{\perp}\bar{f}$ , this is not generally a quantity that is useful to compare to, and the velocity space derivatives must be evaluated judiciously on a spacecraft such as MMS, where there are a finite number of logarithmically-binned energies to evaluate derivatives on. If the goal is still to estimate  $\nabla_{\perp}\bar{f}$ , we provide an estimate based on the assumption of a drifting two temperature Maxwellian distribution, where this assumption is only used for the following equation:

$$\nabla_{\perp} \ln \bar{f} = \frac{q \mathbf{E}_{\perp}}{T_{\perp}} + \frac{T_{\perp} - T_{\parallel}}{T_{\perp} T_{\parallel}} \left( 2 \mathcal{E}_{\parallel} \left[ (\mathbf{b} \cdot \nabla) \mathbf{b} \right] + m v_{\parallel} \frac{\partial \mathbf{b}}{\partial t} \right) - \frac{\int_{0}^{2\pi} \rho f d\gamma}{\pi \rho^{2} \bar{f}}$$
(4.15)

This form can make a justification for dropping all drift terms except  $q\mathbf{E}_{\perp}/T_{\perp}$  (corresponding to the  $\mathbf{E}\times\mathbf{B}$  drift) on the basis of dependence on temperature anisotropy, which will generally be small (as will be the magnitude of the associated drifts). This can be of importance to spacecraft data, as direct measurement of these factors is not generally possible at the single-spacecraft level. While this form contains an abundance of information, it lacks a strong basis for comparison with our intuition on the fluid description of plasma. To this end, we can now take moments of  $\nabla_{\!\perp} \bar{f}$  to find the perpendicular gradients of fluid quantities. In particular, we define

$$\mathcal{M}_{k,l} = \int v_{\perp}^k v_{\parallel}^l \bar{f} \mathrm{d}^3 v = \int v_{\perp}^{k+1} v_{\parallel}^l \bar{f} \mathrm{d} v_{\parallel} \mathrm{d} v_{\perp} \mathrm{d} \gamma \quad . \tag{4.16}$$

It can be shown that the  $\nabla_{\perp}$  operator commutes with the moment operator on  $\bar{f}$ , and thus  $\nabla_{\perp}\mathcal{M}_{k,l} = \int v_{\perp}^k v_{\parallel}^l \nabla_{\perp} \bar{f} \mathrm{d}^3 v$ . Evaluating these integrals, we find:

$$\nabla_{\perp} \mathcal{M}_{k,l} = -2\Omega_{s} \mathbf{b} \times \int \mathbf{v}_{\perp} v_{\parallel}^{l} v_{\perp}^{k-2} f \mathrm{d}^{3} v$$

$$+ \frac{2\pi q \mathbf{E}_{\perp}}{m} \left[ \delta_{k0} \int v_{\parallel}^{l} \bar{f}_{\parallel} \mathrm{d} v_{\parallel} + k \int v_{\parallel}^{l} v_{\perp}^{k-1} \bar{f} \mathrm{d} v_{\perp} \mathrm{d} v_{\parallel} \right]$$

$$+ (\mathbf{b} \cdot \nabla) \mathbf{b} \left[ (l+1) \mathcal{M}_{k,l} - 2\pi \left( \delta_{k0} \int v_{\parallel}^{l+2} \bar{f}_{\parallel} \mathrm{d} v_{\parallel} + k \int v_{\parallel}^{l+2} v_{\perp}^{k-1} \bar{f} \mathrm{d} v_{\perp} \mathrm{d} v_{\parallel} \right) \right]$$

$$+ \frac{\partial \mathbf{b}}{\partial t} \left[ l \mathcal{M}_{k,l-1} - 2\pi \left( \delta_{k0} \int v_{\parallel}^{l+1} \bar{f}_{\parallel} \mathrm{d} v_{\parallel} + k \int v_{\parallel}^{l+1} v_{\perp}^{k-1} \bar{f} \mathrm{d} v_{\perp} \mathrm{d} v_{\parallel} \right) \right] , \quad (4.17)$$

where  $\delta_{k0}$  is the Kronecker delta and we have used the shorthand  $\bar{f}_{\parallel}$  to identify  $\bar{f}(v_{\perp}=0)$ . We note that the drift terms not including  $\bar{f}_{\parallel}$  have resulted from integration by parts in  $v_{\perp}$  in Eq. 4.14. The  $\bar{f}_{\parallel}$  terms no longer have  $v_{\perp}$  coefficients, and are thus integrals of a full derivative in  $v_{\perp}$ , resulting in the values at the bounds of the integral. If we define

$$\mathcal{M}_{-2,l} = 2\pi \int v_{\parallel}^l \bar{f}_{\parallel} \mathrm{d}v_{\parallel} \tag{4.18}$$

$$\mathcal{M}_{-1,l} = 2\pi \int v_{\parallel}^{l} \bar{f} dv_{\parallel} dv_{\perp}, \tag{4.19}$$

where  $\mathcal{M}_{-1,l}$  follows the definition of Eq. 4.16, but  $\mathcal{M}_{-2,l}$  does not (as a result of the aforementioned integration of a full derivative), this can be written slightly more concisely as:

$$\nabla_{\perp} \mathcal{M}_{kl} = -2\Omega_s \mathbf{b} \times \int \mathbf{v}_{\perp} v_{\parallel}^l v_{\perp}^{k-2} f d^3 v + \frac{q \mathbf{E}_{\perp}}{m} (k + \delta_{k0}) \mathcal{M}_{k-2,l}$$

$$+ (\mathbf{b} \cdot \nabla) \mathbf{b} \left[ (l+1) \mathcal{M}_{kl} - (k + \delta_{k0}) \mathcal{M}_{k-2,l+2} \right]$$

$$+ \frac{\partial \mathbf{b}}{\partial t} \left[ l \mathcal{M}_{k,l-1} - (k + \delta_{k0}) \mathcal{M}_{k-2,l+1} \right] . \quad (4.20)$$

Of particular interest are gradients in density and pressure. In this gyrotropic definition of  $\bar{f}$ , we note that

$$n = \mathcal{M}_{0.0} \tag{4.21}$$

$$p_{\perp} = \frac{m}{2} \mathcal{M}_{2,0} \tag{4.22}$$

By evaluating Eq. 4.20, we then find that

$$\nabla_{\perp} n = \frac{2\pi q \mathbf{E}_{\perp}}{m} \int \bar{f}_{\parallel} dv_{\parallel} + (\mathbf{b} \cdot \nabla) \mathbf{b} \left( n - 2\pi \int v_{\parallel}^{2} \bar{f}_{\parallel} dv_{\parallel} \right) - \frac{\partial \mathbf{b}}{\partial t} \left( 2\pi \int v_{\parallel} \bar{f}_{\parallel} dv_{\parallel} \right) - 2 \int \frac{\boldsymbol{\rho} f}{\rho^{2}} d^{3}v \quad (4.23)$$

$$\nabla_{\!\perp} p_{\perp} = nq \left( \mathbf{E}_{\perp} + \mathbf{u}_{s} \times \mathbf{B} \right) - mnu_{\parallel} \frac{\partial \mathbf{b}}{\partial t} + (\mathbf{b} \cdot \nabla) \mathbf{b} \left( p_{\perp} - p_{\parallel} - mnu_{\parallel}^{2} \right). \tag{4.24}$$

These equations present the best estimate of the gradients, but several terms are not locally measured by a single spacecraft. We can see that in the absence of the  $\partial b/\partial t$  and  $(b\cdot \nabla)b$  terms (which are not readily available to single spacecraft observation), the perpendicular pressure gradient term becomes equivalent to the statement that the nonideal electric field is entirely attributable to the diamagnetic drift. This is somewhat unfortunate, as it means that using only the measurements readily available to a single spacecraft, this model does not allow for Ohm's Law terms that can account for reconnection. As such, in this framework, not much can be learned from a single spacecraft about non-ideal dynamics within electron diffusion regions. However, if one desires to estimate pressure gradients for reasons other than determining the breaking of the frozen-in law, this method should provide a good estimate for most magnetized plasma environments that do not simultaneously experience strong curvature and temperature anisotropy. Notably, anisotropy is measurable at

the single-spacecraft level, and strong curvature will be accompanied by sharp shifts in the time series measurement of b, so regions where dropping the curvature term may cause significant error should be identifiable. We also note that it may be possible to estimate  $\partial \mathbf{b}/\partial t$  and  $(\mathbf{b}\cdot\nabla)\mathbf{b}$  by matching their contributions to Eq. 4.24 to the remaining terms in Eq. 4.1, or a multi-spacecraft reconstruction of the local magnetic geometry.

# 4.4 PIC Verification of Length Scale Characterization

In order to verify the drift-kinetic model's ability to characterize density and pressure gradients in a plasma, we calculate the gradients derived from the model on particle data obtained from a series of fully-kinetic VPIC [66] particle-in-cell simulations. While these simulations are two dimensional, mathematically our methods should apply equally well for fully three dimensional reconnection scenarios. The simulations are performed in a modified Harris sheet configuration [115] at  $m_i/m_e = 400$ with a variety of background density asymmetries representing the low density magnetosphere and high density magnetosheath (herein denoted as  $n_1/n_2$ ). The runs correspond to the setup of a suite of simulations described in Chapter 3 of Ref. [116] and are antiparallel. This means that the electrons will not be magnetized everywhere, but this is a small region of the simulations, and demagnetized electrons are soon remagnetized. As such, the results of Section 4.3 should hold over most of the simulation domain. These simulations use periodic boundary conditions in the *x*-direction and conducting/reflecting boundaries in the *z*-direction, have a domain size of  $6720 \times 3360 \text{ cells} = 80 d_i \times 40 d_i \text{ based on the higher}$ upstream density  $n_1$ , and employ the reduced value of  $\omega_{pe}/\omega_{ce}=1.5$ , with  $\beta_1 = 3$ . In total, each run contains  $\sim 18$  billion numerical particles.

We evaluate gradients in two ways: via an implementation of the drift-

kinetic method (Eqs. 4.23 and 4.24) directly on particle data and via direct finite difference calculation of spatial gradients of the density and pressure profiles. The PIC distribution functions are created from particles within a box of approximately  $2\,d_e\times 6\,d_e$  (containing on average  $\sim 80,000$  electron particles), with a measurement centered every  $1\,d_e$  in the N direction. We note that there is still a considerable amount of noise in our density gradient measurements at this domain size, but we do some smoothing to present the picture of the full domain. We present the data in a normalized form that represents the inverse gradient length scale in terms of the electron inertial length to indicate the fine scale structure encountered in the reconnection geometry. The results for density gradients can be seen in Figure 4.3 while gradients in perpendicular pressure are compared in Figure 4.4. General agreement in both form and magnitude is noted.

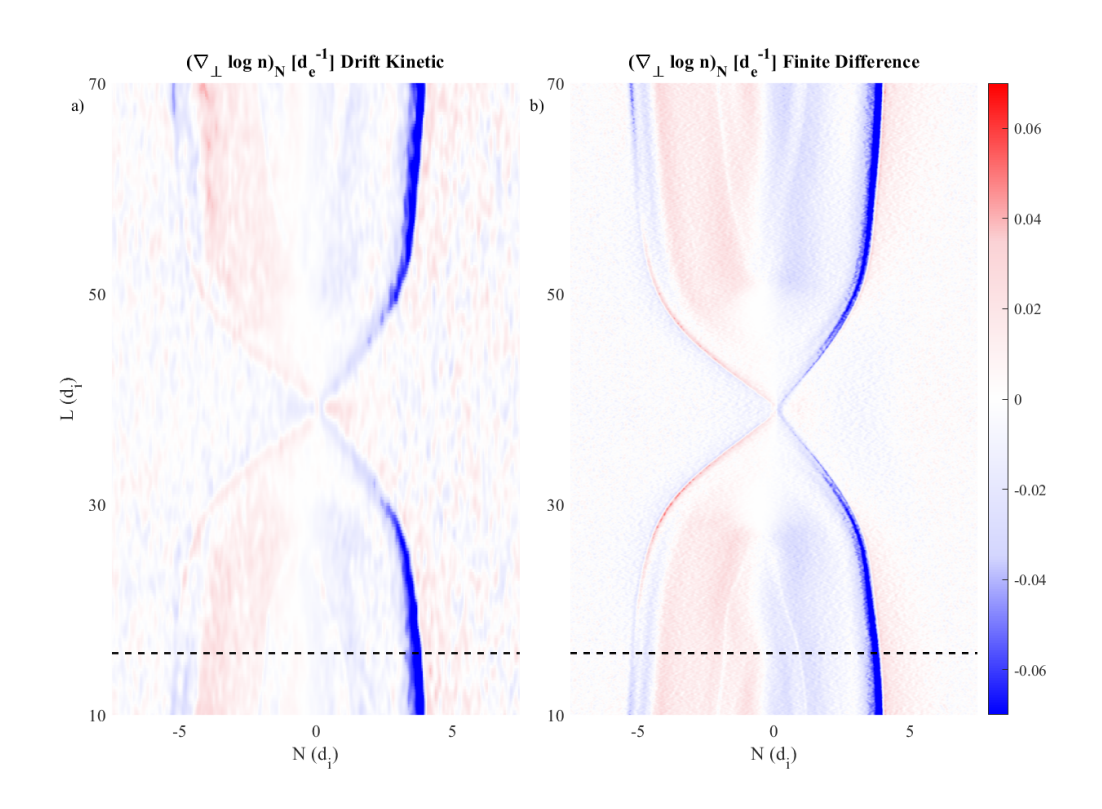


Figure 4.3: Normalized components of  $\nabla_{\perp} \log n$  for a simulation of antiparallel reconnection with  $n_1/n_2=1.4$  through Eq. 4.23 and a direct finite difference method. The dashed line represents the cut taken in Figure 4.5a).

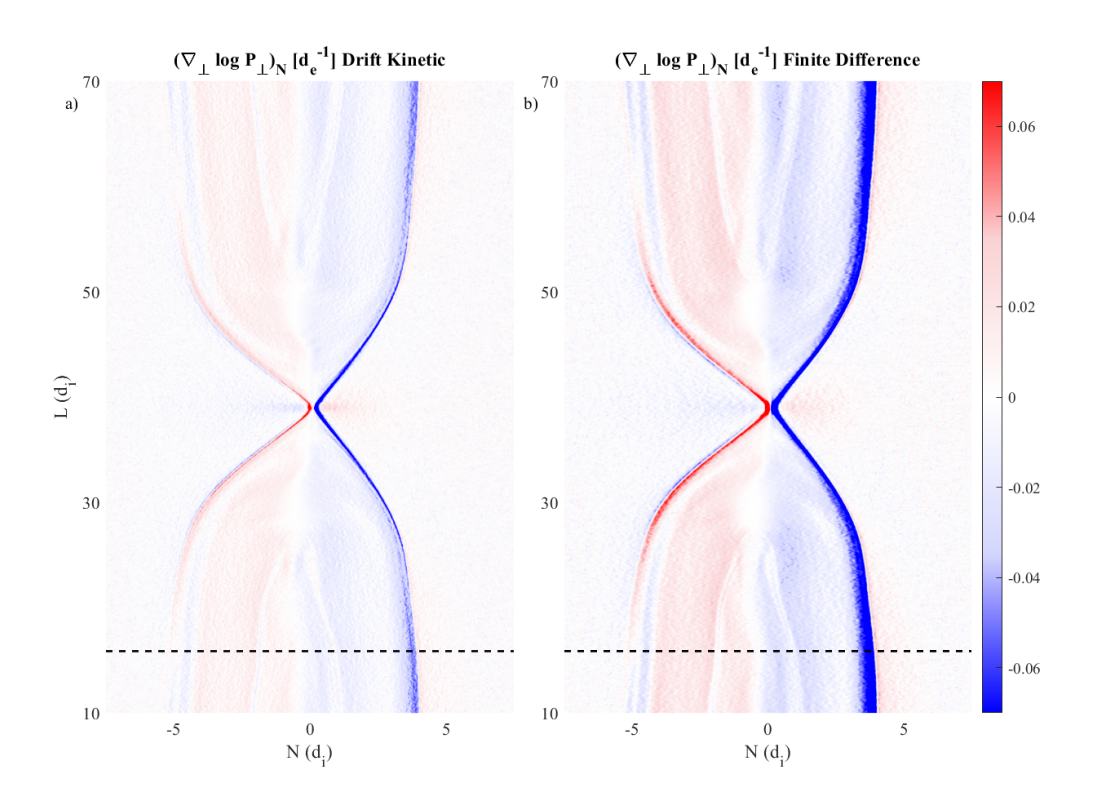
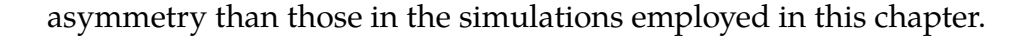


Figure 4.4: Normalized components of  $\nabla_{\perp} \log p_{\perp}$  for a simulation of antiparallel reconnection with  $n_1/n_2=1.4$  through Eq. 4.24 and a direct finite difference method. The color scale is slightly saturated to emphasize the quality of the low amplitude match. The dashed line represents the cut taken in Fig. 4.5a).

It should be noted that there are some limits to the validity of this model. Most importantly, in strongly asymmetric reconnection with low guide field, strong electric fields tend to develop with a width on the order of the electron Larmor radius on the low density separatrix. In these conditions, the drift-kinetic assumptions are violated, and our framework significantly overestimates the gradients. The model should be valid if  $\rho_e \cdot \nabla v_{EB} \ll v_{the}$ , and if gradient scales are larger than the electron Larmor radius. The fields at the separatrix in strongly asymmetric reconnection produce  $v_{EB} \sim v_{the}$  with a width on the order of a few electron Larmor radii, and this is not easily overcome in this model framework, but elsewhere, the model assumptions are generally satisfied. Figure 4.5 shows a comparison of  $\nabla_{\!\perp} n$  calculated by the two methods for a variety of upstream density asymmetry values in antiparallel reconnection. For the antiparallel run with density asymmetry of 16 presented, our model is observed to provide an accurate estimate of the density gradient at the separatrices, and accuracy is expected only to improve for configurations including a guide magnetic field.

We do note that these simulations do not fully encompass the parameters of magnetospheric reconnection. In particular,  $\beta_1=3.0$  is rather high, leading to weaker electric fields at the separatrix and an effectively higher thermal speed. This helps to keep the model within its limits. In realistic magnetopause conditions, a range of upstream  $\beta$ , as well as temperature and density asymmetries must be considered. Testing the model in a separate simulation designed to match the event of Ref. [54] (the simulation used in Ref. [55]) that has lower  $\beta_1$  that includes temperature asymmetry, the drift-kinetic model overestimates the gradients at the separatrices by a factor of 2-3. Combined with the results of the simulations shown, this implies that the method should be viable for the majority of magnetospheric conditions, though gradient scales can only be trusted to an order of magnitude in cases with some combination of lower  $\beta$  and more intense



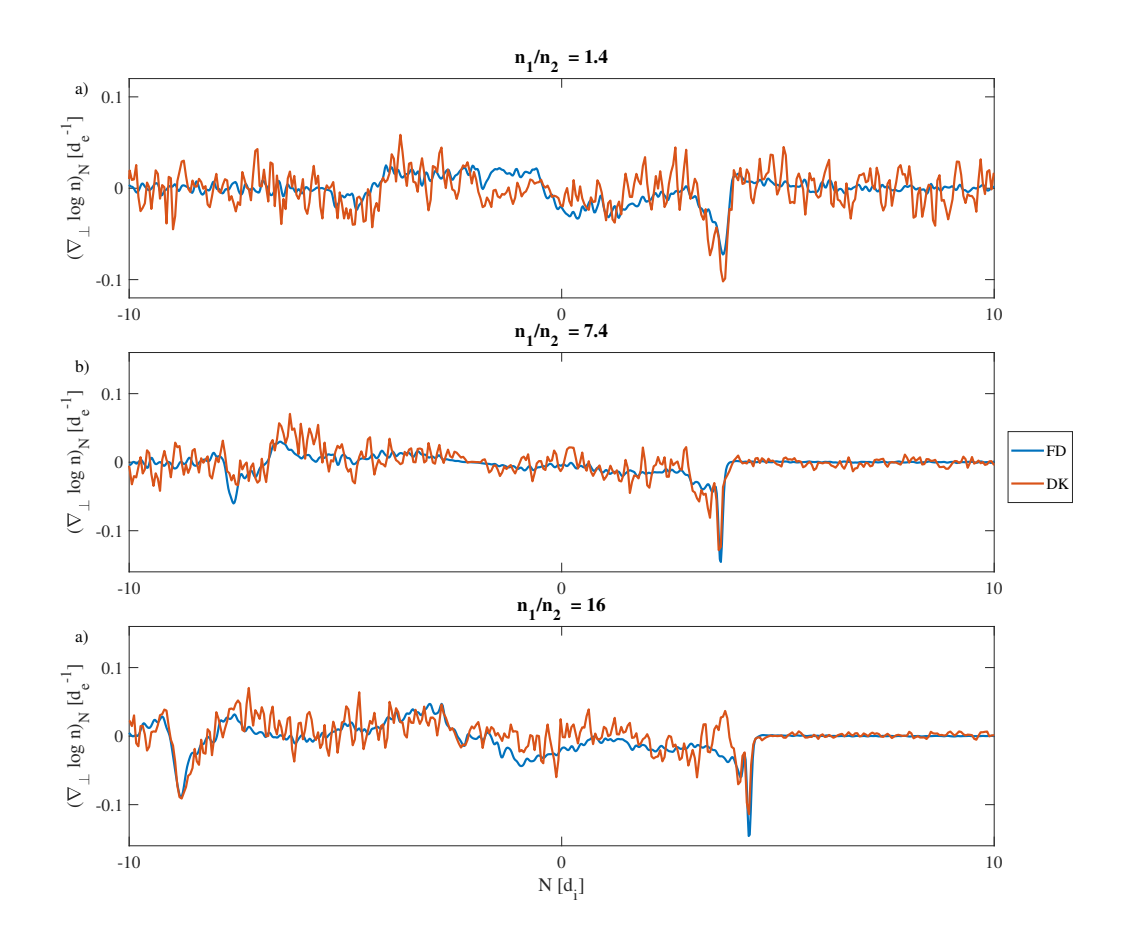


Figure 4.5: Cuts of normalized N components of  $\nabla_{\perp} \log n$  for simulations of antiparallel reconnection with  $n_1/n_2 = 1.4, 7.8$ , and 16 through Eq.4.23 and a direct finite difference method.

#### 4.5 Discussion and Conclusion

In this chapter, we have derived and demonstrated a novel method for inferring plasma gradients from the distribution function measurements of a single spacecraft, linking variations measured within a gyro orbit in velocity space with spatial gradients of a well-magnetized distribution function. This model successfully replicates pressure and density gradients in PIC simulations, and can in principle be applied to MMS data. The PIC verification shows that the gradient estimates can be quite noisy, though they clearly approximate the correct gradients. This may be a challenge when implementing the technique on spacecraft data. Furthermore, it should be noted that this technique requires the electrons to stay well-magnetized to be accurate. As such, in the absence of a strong guide field, this technique is likely not useful immediately at the x-line, though it can be useful in determining the reconnection geometry away from the x-line.

This model also has implications for the way we think of agyrotropy in distribution functions. Using the drift-kinetic method, we have shown that apparent agyrotropy in the electron distribution function can correspond to spatial gradients in a distribution function that is gyrotropic when spatially sorted to match guiding centers. In this sense, a well-magnetized distribution can be agyrotropic in the standard models of agyrotropy [109, 111]. Agyrotropy is often used as a measure of demagnetization, but without accounting for spatial gradients in the plasma properties, this is not inherently true. In particular, strong gradients often exist around the separatrices in asymmetric reconnection. While the agyrotropy measure may be high at the separatrix, this does not generally imply that the electrons are demagnetized.

The results of this Chapter were published in Ref. [117]. A more intuitive (but subtly incorrect) alternative derivation of the drift-kinetic gradient method can be found in Appendix C.

In this thesis, we have delved into several topics related to magnetic reconnection and the Magnetospheric Multiscale mission. These topics have all focused on anisotropic distribution functions resulting from the collisionless kinetic physics of well-magnetized electrons, with drift-kinetics being the primary theoretical basis used. Chapters 2 and 3 focused on applications of an existing anisotropic model [41, 81], in which the diagonal pressure tensor component parallel to the magnetic field decouples from those perpendicular to the magnetic field, to MMS data with some extensions. Chapter 4, rather than looking at differences in dynamics along the magnetic field relative to those perpendicular to the magnetic field, investigated agyrotropy, the loss of symmetry in the perpendicular plane, and connected it to gradients in fluid plasma properties.

In Chapter 2, we noted that a valid fluid model for electrons in collisionless space plasmas is desirable for understanding the structure and evolution of magnetic reconnection geometries. Additionally, such a fluid model would be useful for the simulation of systems too large to be tractable in a fully kinetic model. Using MMS spacecraft observations, we provided direct confirmation of the EoS for the electron pressure tensor during guide field reconnection and demonstrated that the closure can be applied in efficient numerical simulation, yielding new physical insight to the electron heating problem. Furthermore, we applied the EoS to derive a scaling of electron heating in the exhaust comparable to the available observational data.

In Chapter 3, we applied the anisotropic electron heating predictions of the EoS to reconnection in the Earth's magnetosheath. The model is applicable to open systems where electrons are streaming along magnetic field lines into the reconnection region, sourced by fixed external reservoirs of plasma ambient to the reconnection region. While Chapter 2 showed the EoS hold in the region near the X-line, we found that for an event observed far downstream ( $\sim 100\,d_i$ ) from the X-line both inflows and the exhaust follow the predictions of the EoS and correspond to three separate upstream sets of parameters. Furthermore, the model underlying the EoS was extended to include additional perpendicular heating terms relevant to the considered event undergoing active magnetic compression with local electron trapping. The agreement between the spacecraft observations and the EoS emphasizes the roles of the ambient plasma sources and the dynamics of trapped and passing electrons in setting and controlling the anisotropic electron heating at large scale in naturally occurring plasma configurations.

In Chapter 4, we derived a new drift-kinetic method for estimating gradients in the plasma properties through a velocity space distribution at a single point. The gradients are intrinsically related to agyrotropic features of the distribution function. This method predicts the gradients in the magnetized distribution function and can predict gradients of arbitrary moments of the gyrotropic background distribution function. The method allows for estimates on density and pressure gradients on the scale of a Larmor radius, proving to resolve smaller scales than any method currently available to spacecraft. The model was verified with a set of fully kinetic VPIC particle-in-cell simulations.

Several topics discussed herein deserve further attention. For instance, in Chapter 2, a prediction was made for the scaling of exhaust electron heating in guide field reconnection with several parameters. We have merely derived the scaling and showed it to be comparable to general predictions for such heating in the magnetosphere, but made no effort to see how this heating actually depends on the parameters in the scaling in comprehensive simulations or observations of naturally-occurring reconnection. A series of 2D (mainly for computational cost considerations) kinetic simulations scanning  $\beta_{e\infty}$ ,  $B_g/B_r$ , and  $T_i/T_e$  could test this predic-

tion rather easily. It would also be interesting to delve further into guide field reconnection events observed by MMS and characterize the scaling of the naturally occurring events.

Chapters 2 and 3 showed that the EoS of Ref. [41] holds for some events, and it can potentially identify asymmetric upstream populations. A more detailed statistical examination of MMS reconnection events would be interesting to see how universally these anisotropic equations of state hold in magnetospheric reconnection. Furthermore, Chapter 3 introduced corrections to the model to account for magnetic field compression and local electron trapping. By examining a broader range of MMS events we could say something more about how often the compressing case is observed and whether it is intrinsically tied to being far downstream of the X-line.

Chapter 4 introduced a drift-kinetic model for predicting spatial gradients in the electron distribution function based on agyrotropic variations in velocity space. The model was derived with the application of MMS data in mind, but this has not been successfully applied yet. A careful implementation of the drift-kinetic method on MMS data could provide useful context to the interpretation of events, though noise could be a considerable issue without a thoughtful method to account for it. With the drift-kinetic method, gradients can be measured down to the scale of the electron gyroradius, which is generally smaller than the separation between spacecraft. Beyond the increased resolution, having a gradient measure at the location of each of the four spacecraft rather than a single measure at the center of the tetrahedral formation can provide additional information about the geometry of events, including an estimate in the second-order variation of fluid properties.

With implementation issues resolved, the method has great potential to provide insight into magnetospheric plasma physics in a variety of ways. This is not limited to magnetic reconnection, as the method is general to collisonless plasmas wherein the species of interest remains well-magnetized. This means that for spacecraft like MMS, the method can be used along the majority of the formation's orbit, including regions of the solar wind and Earth's magnetosphere. Those interested in processes occurring in those regions could benefit from the drift-kinetic method.

### A MMS Data Interpretation and Coordinate Systems

#### A.1 LMN Coordinates

Current sheets in magnetospheric reconnection are not consistently aligned in the same direction. As such, a coordinate transformation to locally align the current sheet with typical simulation coordinates is useful. In this way, MMS events may be more easily mapped to computational simulations.

MMS records its vector and tensor measurements in two coordinate systems— geocentric solar ecliptic (GSE) and geocentric solar magnetospheric (GSM). Both coordinates align the X direction along the Earth-Sun vector. GSE coordinates align the Z axis perpendicular to the ecliptic plane (the plane of Earth's orbit), with North positive. The GSM coordinate system aligns its Z axis with the projection of Earth's dipole axis on the plane perpendicular to the X axis. Both systems define Y as the unit vector that makes XYZ a right-handed orthonormal basis.

Generally, data in this thesis comes from the data dumped in GSE coordinates. To analyze data, we will often rotate to a local right-handed LMN basis that we will use to compare to 2.5D kinetic simulations. The L vector should be the transverse direction (the direction of the reversing magnetic field, equivalent to x used in most of our simulations). N represents the normal direction, along which the primary gradient in the magnetic field is aligned, or the z direction in the kinetic simulations. M constitutes the out-of-plane direction in the 2D slab picture of reconnection, equivalent to the y direction in the simulations, and the direction along which the guide field would align.

Traditionally, the N vector can be determined through a minimum variance analysis of the magnetic field [118]. This means that  $\mathbf{N}$  is chosen to be the unit vector such that  $\mathbf{B} \cdot \mathbf{N}$  has the smallest variance over a

layer crossing. More recently, L has been identified by the maximally varying component of B [119]. The process of finding the transformation to the local LMN system can be sensitive to small variations under typical magnetospheric conditions, as the smallest two eigenvalues of the variance of B are often not well separated, leading to degeneracy in the MN-plane. Newer methods that incorporate gradients in B measured by multiple spacecraft are more stable, but still have uncertainties on the order of  $5^{\circ} - 10^{\circ}$ , which may be significant in interpreting data [120]. As such, some adjustments may be made to the LMN coordinate system to better match the context of the data measured.

In this thesis, the LMN coordinates have entered explicitly only in Figures 2.1b) and 3.4a) and g) through components of the magnetic field. In these cases, we used LMN bases found by previous authors in Refs. [80, 97] and did not need to adjust them in any way. The LMN basis is crucial in determining the guide field of the event. This is important, as it showed we were in a guide-field regime in both Chapters 2 and 3, and it allows for simulations to properly match the event parameters.

# A.2 Converting MMS Distributions to Field-Aligned Coordinates

Breaking down vector quantities into field-aligned parallel and perpendicular components is straightforward. All that needs to be done is to project onto the field-aligned basis. The field-aligned basis can be specified as  $(\hat{\mathbf{b}}, \hat{\perp}_1, \hat{\perp}_2)$ , with  $\hat{\mathbf{b}} = \mathbf{B}/|\mathbf{B}|$ ,  $\hat{\perp}_1 = \hat{\mathbf{r}} \times \hat{\mathbf{b}}/|\hat{\mathbf{r}} \times \hat{\mathbf{b}}|$ , and  $\hat{\perp}_2 = \hat{\mathbf{b}} \times \hat{\perp}_1$  for some unit vector  $\hat{\mathbf{r}} \neq \hat{\mathbf{b}}$ . To avoid degeneracy in the perpendicular plane,  $\hat{\mathbf{r}}$  should be chosen to align minimally with  $\hat{\mathbf{b}}$  over the course of an event. In the context of dayside reconnection, this role is generally well-served by the Earth-Sun direction vector  $\hat{\mathbf{X}}$ .

Rotating the distribution function data into field aligned coordinates is

a little more difficult. The data is stored as  $f_{GSE}(\mathcal{E}, \Theta, \Phi)$ , where  $\Theta$  and  $\Phi$  are the azimuthal and polar angles of the spherical transformation of the GSE coordinates. We want to transform this to  $f(\mathcal{E}, \theta, \gamma)$ , where  $\theta$  is the pitch angle and  $\gamma$  is the gyrophase. To do this, we create a new grid on which the distribution function will be interpolated and utilize the transform  $\mathbf{g}(\theta, \gamma) = (\Theta, \Phi)$  through the relation  $f(\mathcal{E}, \theta, \gamma) = f_{GSE}(\mathcal{E}, \mathbf{g}(\theta, \gamma))$ . All that is left is to find the form of  $\mathbf{g}(\theta, \gamma)$ . Analytic determination of  $\mathbf{g}(\theta, \gamma)$  is messy, but it is simple to due numerically through the intermediate step of finding  $\hat{\mathbf{x}}(\theta, \gamma)$  for the full grid of interpolation points. These unit vector coordinates are then easily converted back to the GSE  $(\Theta, \Phi)$  angles for data interpolation, where at each time there is a transform defined (by  $\hat{\mathbf{b}}$  at the time of the measurement) to be used on each energy.

In this way, we obtain a field-aligned distribution function. Every MMS-measured distribution presented in this thesis has been gyroaveraged over  $\gamma$ , as agyrotropy is generally small. Most of the distributions are plotted in the  $v_\parallel, v_\perp$  plane, where  $(v_\parallel, v_\perp) = \sqrt{2\mathcal{E}/m}(\cos\theta, \sin\theta)$ . This is only a matter of choosing plotting points, as distributions measured by MMS are already in velocity space density rather than energy-angle space density.

## B Deriving the Boltzmann and CGL Limits

The two limits of the standard case of the equations of state of Ref. [41] are the Boltzmann and CGL limits, corresponding to the cases of no electron trapping and full electron trapping, respectively. In this section, I will derive the scalings of each limit.

The Boltzmann limit is that of a collisionless plasma working against an electric field. We begin with the Vlasov equation governing collisionless plasma distribution functions,

$$\frac{\partial f}{\partial t} + (\mathbf{v} \cdot \mathbf{\nabla}) f + \frac{q}{m} (\mathbf{E} + \mathbf{v} \times \mathbf{B}) \cdot \frac{\partial f}{\partial \mathbf{v}} = 0 \quad . \tag{B.1}$$

We reduce to the simple unmagnetized case with no magnetic field and search for a steady-state solution. This requires that

$$(\mathbf{v} \cdot \mathbf{\nabla}) f - \frac{q}{m} \mathbf{\nabla} \Phi \cdot \frac{\partial f}{\partial \mathbf{v}} = 0 \quad . \tag{B.2}$$

This is a Hamiltonian system with  $U=mv^2/2+q\Phi$  conserved along trajectories. If the distribution function at a location  $x_0$  where  $\Phi$  is chosen to be zero depends only on kinetic energy  $\mathcal{E}=mv^2/2$ , i.e. is isotropic, by Liouville's theorem we have that

$$f(\mathbf{x}, \mathcal{E}) = f(\mathbf{x}_0, \mathcal{E} + q\Phi)$$
 (B.3)

If the initial distribution is Maxwellian, we have

$$f(\mathbf{x}, \mathcal{E}) = n_0 \left(\frac{m}{2\pi T}\right)^{3/2} e^{-\frac{\mathcal{E} + q\Phi}{T}} = e^{-\frac{q\Phi}{T}} f(x_0, \mathcal{E})$$
 (B.4)

Importantly, this implies that the distribution is only modified by a scalar multiple determined by position, and the velocity space structure remains unchanged. This means that the density varies according to the potential

(fewer particles will inhabit the regions where their potential energy is higher), but the temperature does not. As such, the Boltzmann limit is an isothermal limit. In the magnetized sense, this translates to being isothermal along field lines, as can be seen by the passing solution described in Eq. 1.15.

The CGL limit is a doubly-adiabatic limit of particles trapped in a flux tube. The trapped particles will conserve their first two adiabatic invariants, the magnetic moment  $\mu=mv_\perp^2/2B$  and the second adiabatic invariant  $J=\oint v_\parallel \mathrm{d}l$  associated with the bounce motion action integral. We will do a simple analysis of the scaling of parallel and perpendicular temperatures with density and magnetic field strength given the conservation laws governing a uniform, closed flux tube.

First, we argue that the perpendicular temperature scales as  $T_{\perp} \sim \mu B$  and the parallel temperature scales as  $T_{\parallel} \sim mJ^2/L^2$ , where L is the length of the bounce orbit (in the case of the closed uniform flux tube, this is the length of the tube).  $\mu$ , J, and m are conserved along orbits, so we find that

$$T_{\perp} \sim B$$
 (B.5)

$$T_{\parallel} \sim L^{-2}$$
 . (B.6)

This is fine for the perpendicular temperature, but not particularly enlightening for the parallel temperature without characterizing the orbit length with respect to other parameters. We consider a flux tube of length L, cross sectional area A, and density n. Conservation of flux (as defined by the flux tube) implies that BA is constant. Conservation of the total number of particles in the flux tube implies that LAn is also constant. Combining these two observations, Ln/B is also constant. As such  $L \sim B/n$ , giving the final scaling for the parallel temperature

$$T_{\parallel} \sim \left(\frac{n}{B}\right)^2$$
 (B.7)

These scalings exhibit a strong degree of anisotropy. By combining Equations B.5 and B.7, we see that the temperature anisotropy scales as

$$\frac{T_{\parallel}}{T_{\perp}} \sim \frac{n^2}{B^3} \quad , \tag{B.8}$$

which has strong dependence on both density and magnetic field strength.

## Intuitive Derivation of Gradients of

## Magnetized Distributions

While the derivation in Chapter 4 is the correct one, a more intuitive derivation can reproduce similar results. First, we define a gyrotropic distribution to be one with the property

$$f(\mathbf{x}, \mathbf{v}, t) = \bar{f}(\mathbf{x} - \boldsymbol{\rho}, \mathbf{v} - \mathbf{v}_{\mathbf{D}}, t). \tag{C.1}$$

Then, we approximate the full distribution function by a first-order Taylor expansion of  $\bar{f}$  in position and velocity space.

$$f(\mathbf{x}, \mathbf{v}, t) \approx \bar{f}(\mathbf{x}, \mathbf{v}, t) - \boldsymbol{\rho} \cdot \boldsymbol{\nabla} \bar{f} \bigg|_{\mathbf{x}, \mathbf{v}, t} - \mathbf{v}_{\mathbf{D}} \cdot \frac{\partial \bar{f}}{\partial \mathbf{v}} \bigg|_{\mathbf{x}, \mathbf{v}, t}$$
 (C.2)

By multiplying Eq. C.2 by  $\rho$ , integrating over the gyrophase, and solving for the gradient term, we find

$$\nabla_{\perp} \bar{f} = \frac{\mathbf{b} \times \mathbf{v_D}}{\rho} \frac{\partial \bar{f}}{\partial v_{\perp}} - \int \frac{\rho f}{\pi \rho^2} d\gamma$$
 (C.3)

In the same coordinate system, Eq. 4.13 would be written as

$$\nabla_{\perp} \bar{f} = \frac{e \mathbf{E}_{\perp}}{m v_{||}} \frac{\partial \bar{f}}{\partial v_{||}} + \frac{\mathbf{b} \times \mathbf{v}_{\mathbf{D}}}{\rho} \left( \frac{\partial \bar{f}}{\partial v_{\perp}} - \frac{v_{\perp}}{v_{||}} \frac{\partial \bar{f}}{\partial v_{||}} \right) - \int \frac{\boldsymbol{\rho} f}{\pi \rho^{2}} d\gamma, \tag{C.4}$$

where the  $\mathbf{E}_{\perp}$  term cancels with the  $\mathbf{E} \times \mathbf{B}$  drift term's dependence on the parallel velocity, making Eq. C.3 match Eq. C.4 when the only drift is the  $\mathbf{E} \times \mathbf{B}$  drift. The difference in the results of the two derivation then lies in the inclusion of the  $\nabla B$  drift in the Taylor method, and the extra term proportional to  $\partial \bar{f}/\partial v_{||}$  for the  $\partial \mathbf{b}/\partial t$  and curvature drifts. If we exclude the curvature drift in this analysis (its terms have a singularity), we can approximate gradients of moments of the distribution function as well.

The result will differ from Eq. 4.20 by  $(l+1)\mathcal{M}_{k,l}(\mathbf{b}\cdot\mathbf{\nabla})\mathbf{b} + l\mathcal{M}_{k,l-1}\partial\mathbf{b}/\partial t$ .

As such, this simplified approach gives a reasonable heuristic understanding of what the drift kinetic equations are doing, but without some insight into the subtleties of the drift kinetic limit.

- [1] E. G. Zweibel and M. Yamada, "Magnetic Reconnection in Astrophysical and Laboratory Plasmas," *Annual Review of Astronomy and Astrophysics*, vol. 47, no. 1, pp. 291–332, 2009. [Online]. Available: http://www.annualreviews.org/doi/10.1146/annurev-astro-082708-101726
- [2] J. Egedal, A. Le, and W. Daughton, "A review of pressure anisotropy caused by electron trapping in collisionless plasma, and its implications for magnetic reconnection," *Physics of Plasmas*, vol. 20, no. 6, 6 2013.
- [3] T. D. Phan, M. A. Shay, J. T. Gosling, M. Fujimoto, J. F. Drake, G. Paschmann, M. Oieroset, J. P. Eastwood, V. Angelopoulos, J. T. Gosling, M. Oieroset, M. Fujimoto, J. F. Drake, and V. Angelopoulos, "Electron bulk heating in magnetic reconnection at Earth's magnetopause: Dependence on the inflow Alfvén speed and magnetic shear," *Geophysical Research Letters*, vol. 40, no. 17, pp. 4475–4480, 1 2013.
- [4] E. Priest and T. Forbes, *Magnetic Reconnection*. New York: Cambridge University Press, 2000.
- [5] J. A. Wesson, "Sawtooth reconnection," *Nuclear Fusion*, vol. 30, no. 12, pp. 2545–2549, 12 1990.
- [6] B. Zhang and H. Yan, "The internal-collision-induced magnetic reconnection and turbulence (ICMART) model of gamma-ray bursts," *Astrophysical Journal*, vol. 726, no. 2, 2011.
- [7] J. Dungey, "Conditions for the occurence of electrical discharges in astrophysical systems," *Philos. Mag.*, vol. 44, no. 354, pp. 725–738, 1953.

- [8] J. Birn, J. F. Drake, M. A. Shay, B. N. Rogers, R. E. Denton, M. Hesse, M. Kuznetsova, Z. W. Ma, A. Bhattacharjee, A. Otto, and P. L. Pritchett, "Geospace Environmental Modeling ({GEM}) Magnetic Reconnection Challenge," J. Geophys. Res., vol. 106, no. A3, pp. 3715–3719, 3 2001.
- [9] A. Y. Aydemir, "Nonlinear studies of M=1 modes in high-temperature plasmas," *Physics of Fluids B-Plasma Physics*, vol. 4, no. 11, pp. 3469–3472, 11 1992.
- [10] J. Egedal, J. Ng, A. Le, W. Daughton, B. Wetherton, J. Dorelli, D. Gershman, and A. Rager, "Pressure Tensor Elements Breaking the Frozen-In Law During Reconnection in Earth's Magnetotail," *Phys. Rev. Lett.*, vol. 123, no. 225101, pp. 1–5, 2019.
- [11] M. Hesse, "Dissipation in magnetic reconnection with a guide magnetic field," *Phys. Plasmas*, vol. 13, no. 12, p. 122107, 12 2006.
- [12] A. Bhattacharjee, K. Germaschewski, and C. S. Ng, "Current singularities: Drivers of impulsive reconnection," *Phys. Plasmas*, vol. 12, no. 4, p. 42305, 4 2005.
- [13] J. Egedal, A. Le, W. Daughton, B. Wetherton, P. A. Cassak, J. Burch, B. Lavraud, J. Dorelli, D. J. Gershman, and L. Avanov, "Spacecraft Observations of Oblique Electron Beams Breaking the Frozen-In Law During Asymmetric Reconnection," *Physical Review Letters*, vol. 120, no. 5, p. 055101, 2018. [Online]. Available: https://link.aps.org/doi/10.1103/PhysRevLett.120.055101
- [14] P. A. Sweet, "The production of high energy particles in solar flares," *Nuovo Cimento Suppl.*, vol. 8, p. 188, 1 1958.
- [15] E. N. Parker, "Sweet's mechanism for merging magnetic fields in conducting fluids," *J. Geophys. Res.*, vol. 62, no. 4, pp. 509–520, 1957.
- [16] H. E. Petschek, "Magnetic Field Annihilation," in *The Physics of Solar Flares, Proceedings of the AAS-NASA Symposium held 28-30 October, 1963 at the Goddard Space Flight Center*, W. N. Hess, Ed. Greenbelt, MD: National Aeronautics and Space Administration, Science and Technical Information Division, 1964, p. 425.

- [17] M. Hesse, J. Birn, and M. Kuznetsova, "Collisionless magnetic reconnection: Electron processes and transport modeling," *Journal of Geophysical Research: Space Physics*, vol. 106, pp. 3721–3735, 2001.
- [18] P. Pritchett, "Geospace Environment Modeling magnetic reconnection challenge: Simulations with a full particle electromagnetic code," *J. Geophys. Res.*, vol. 106, no. A3, pp. 3783–3798, 3 2001.
- [19] M. A. Shay, J. F. Drake, B. N. Rogers, and R. E. Denton, "Alfvénic collisionless magnetic reconnection and the Hall term," *Journal of Geophysical Research : Space Physics*, vol. 106, no. A3, pp. 3759–3772, 3 2001. [Online]. Available: http://doi.wiley.com/10. 1029/1999JA001007
- [20] M. M. Kuznetsova, M. Hesse, and D. Winske, "Collisionless reconnection supported by nongyrotropic pressure effects in hybrid and particle simulations," *Journal of Geophysical Research : Space Physics*, vol. 106, pp. 3799–3810, 2001.
- [21] Z. W. Ma and A. Bhattacharjee, "Hall magnetohydrodynamic reconnection: The Geospace Environment Modeling challenge," *Journal of Geophysical Research: Space Physics*, vol. 106, no. A3, pp. 3773–3782, 2001.
- [22] J. Birn and M. Hesse, "Geospace Environment Modeling (GEM) magnetic reconnection challenge: Resistive tearing, anisotropic pressure and Hall effects," *Journal of Geophysical Research: Space Physics*, vol. 106, no. A3, pp. 3737–3750, 2001.
- [23] A. Otto, "Geospace Environment Modeling (GEM) magnetic reconnection challenge: MHD and Hall MHD-constant and current dependent resistivity models," *Journal of Geophysical Research: Space Physics*, vol. 106, no. A3, pp. 3751–3757, 2001.

- [24] B. Lavraud, Y. C. Zhang, Y. Vernisse, D. J. Gershman, J. Dorelli, P. A. Cassak, J. Dargent, C. Pollock, B. Giles, N. Aunai, M. Argall, L. Avanov, A. Barrie, J. Burch, M. Chandler, L. J. J. Chen, G. Clark, I. Cohen, V. Coffey, J. P. Eastwood, J. Egedal, S. Eriksson, R. Ergun, C. J. Farrugia, S. A. Fuselier, V. Genot, D. Graham, E. Grigorenko, H. Hasegawa, C. Jacquey, I. Kacem, Y. Khotyaintsev, E. Macdonald, W. Magnes, A. Marchaudon, B. Mauk, T. E. Moore, T. Mukai, R. Nakamura, W. Paterson, E. Penou, T. D. Phan, A. Rager, A. Retino, Z. J. Rong, C. T. Russell, Y. Saito, J. A. A. Sauvaud, S. J. Schwartz, C. Shen, S. Smith, R. Strangeway, S. Toledo-Redondo, R. Torbert, D. L. Turner, S. Wang, S. Yokota, V. Génot, D. Graham, E. Grigorenko, H. Hasegawa, C. Jacquey, I. Kacem, Y. Khotyaintsev, E. Macdonald, W. Magnes, A. Marchaudon, B. Mauk, T. E. Moore, T. Mukai, R. Nakamura, W. Paterson, E. Penou, T. D. Phan, A. Rager, A. Retino, Z. J. Rong, C. T. Russell, Y. Saito, J. A. A. Sauvaud, S. J. Schwartz, C. Shen, S. Smith, R. Strangeway, S. Toledo-Redondo, R. Torbert, D. L. Turner, S. Wang, and S. Yokota, "Currents and associated electron scattering and bouncing near the diffusion region at Earth's magnetopause," Geophysical Research Letters, vol. 43, no. 7, pp. 3042–3050, 4 2016.
- [25] T. Nagai, I. Shinohara, M. Fujimoto, M. Hoshino, Y. Saito, S. Machida, and T. Mukai, "Geotail observations of the Hall current system: Evidence of magnetic reconnection in the magnetotail," *J. Geophys. Res.*, vol. 106, no. A11, pp. 25929–25949, 11 2001.
- [26] A. Runov, R. Nakamura, W. Baumjohann, R. A. Treumann, T. L. Zhang, M. Volwerk, Z. Voros, A. Balogh, K. H. Glassmeier, B. Klecker, H. Reme, and L. Kistler, "Current sheet structure near magnetic X-line observed by Cluster," *Geophy. Res. Lett.*, vol. 30, no. 11, 6 2003.

- [27] R. Nakamura, A. Varsani, K. J. Genestreti, O. Le Contel, T. Nakamura, W. Baumjohann, T. Nagai, A. Artemyev, J. Birn, V. A. Sergeev, S. Apatenkov, R. E. Ergun, S. A. Fuselier, D. J. Gershman, B. J. Giles, Y. V. Khotyaintsev, P. A. Lindqvist, W. Magnes, B. Mauk, A. Petrukovich, C. T. Russell, J. Stawarz, R. J. Strangeway, B. Anderson, J. L. Burch, K. R. Bromund, I. Cohen, D. Fischer, A. Jaynes, L. Kepko, G. Le, F. Plaschke, G. Reeves, H. J. Singer, J. A. Slavin, R. B. Torbert, and D. L. Turner, "Multiscale Currents Observed by MMS in the Flow Braking Region," *Journal of Geophysical Research: Space Physics*, vol. 123, no. 2, pp. 1260–1278, 2018.
- [28] M. Øieroset, T. Phan, M. Fujimoto, R. P. Lin, and R. P. Lepping, "In situ detection of collisionless reconnection in the Earth's magnetotail," *Nature*, vol. 412, no. 6845, pp. 414–417, 7 2001.
- [29] N. F. Loureiro, A. A. Schekochihin, and S. C. Cowley, "Instability of current sheets and formation of plasmoid chains," *Physics of Plasmas*, vol. 14, 2007.
- [30] L. Comisso, M. Lingam, Y. M. Huang, and A. Bhattacharjee, "General theory of the plasmoid instability," *Physics of Plasmas*, vol. 23, no. 10, 2016.
- [31] W. Daughton, V. Roytershteyn, B. J. Albright, H. Karimabadi, L. Yin, and K. J. Bowers, "Transition from collisional to kinetic regimes in large-scale reconnection layers," *Phys. Rev. Lett.*, vol. 103, no. 6, p. 65004, 8 2009.
- [32] A. Le, J. Egedal, W. Daughton, V. Roytershteyn, H. Karimabadi, and C. Forest, "Transition in electron physics of magnetic reconnection in weakly collisional plasma," *Journal of Plasma Physics*, vol. 81, no. 1, 2015.
- [33] J. Liouville, "Note sur la Théorie de la Variation des constantes arbitraires." *Journal de mathématiques pures et appliquées*, vol. 3, no. 1, pp. 342–349, 1838.
- [34] J. Egedal, W. Daughton, J. F. Drake, N. Katz, and A. Le, "Formation of a localized acceleration potential during magnetic reconnection with a guide field," *Physics of Plasmas*, vol. 16, no. 050701, 2009.

- [35] J. Egedal and A. Fasoli, "Single-particle dynamics in collisionless magnetic reconnection," *Phys. Rev. Lett.*, vol. 86, no. 22, pp. 5047–5050, 5 2001.
- [36] J. Egedal, "A drift kinetic approach to stationary collisionless magnetic reconnection in an open cusp plasma," *Phys. Plasmas*, vol. 9, no. 4, pp. 1095–1103, 4 2002.
- [37] J. Egedal, A. Le, N. Katz, L. J. Chen, B. Lefebvre, W. Daughton, and A. Fazakerley, "Cluster observations of bidirectional beams caused by electron trapping during antiparallel reconnection," *J. Geophys. Res.*, vol. 115, p. A03214, 3 2010.
- [38] J. Egedal, A. Fasoli, M. Porkolab, and D. Tarkowski, "Plasma generation and confinement in a toroidal magnetic cusp," *Review of Scientific Instruments*, vol. 71, no. 9, pp. 3351–3361, 9 2000.
- [39] J. Egedal, "The orbit averaged particle source from neutral beam injection in tokamaks," *Nuclear Fusion*, vol. 45, 2005.
- [40] P. K. Montag and J. Egedal, "Pressure and Density Scaling in the High-Energy Trapping Distribution During Reconnection," in *APS Division of Plasma Physics Meeting Abstracts*, San Jose, CA, 2016, p. BP10.071.
- [41] A. Le, J. Egedal, W. Daughton, W. Fox, and N. Katz, "Equations of State for Collisionless Guide-Field Reconnection," *Phys. Rev. Lett.*, vol. 102, no. 085001, 2 2009.
- [42] G. F. Chew, M. L. Goldberger, and F. E. Low, "The Boltzmann equation and the one-fluid hydromagnetic equations in the absence of particle collisions," *Proc. R. Soc. London, Ser. A*, vol. 236, no. 1204, pp. 112–118, 1956.
- [43] O. Ohia, J. Egedal, V. S. Lukin, W. Daughton, and A. Le, "Demonstration of Anisotropic Fluid Closure Capturing the Kinetic Structure of Magnetic Reconnection," *Phys. Rev. Lett.*, vol. 109, no. 11, 9 2012.
- [44] V. S. Lukin and M. G. Linton, "Three-dimensional magnetic reconnection through a moving magnetic null," *Nonlinear Processes in Geophysics*, vol. 18, no. 6, pp. 871–882, 2011.

- [45] A. Le, J. Egedal, O. Ohia, W. Daughton, H. Karimabadi, and V. S. Lukin, "Regimes of the electron diffusion region in magnetic reconnection," *Physical Review Letters*, vol. 110, no. 13, 3 2013.
- [46] A. Le, W. Daughton, H. Karimabadi, and J. Egedal, "Hybrid simulations of magnetic reconnection with kinetic ions and fluid electron pressure anisotropy," *Phys. Plasmas*, vol. 23, no. 3, p. 032114 (7 pp.), 3 2016.
- [47] H. Karimabadi, V. Roytershteyn, H. X. Vu, Y. A. Omelchenko, J. Scudder, W. Daughton, A. Dimmock, K. Nykyri, M. Wan, D. Sibeck, M. Tatineni, A. Majumdar, B. Loring, and B. Geveci, "The link between shocks, turbulence, and magnetic reconnection in collisionless plasmas," *Physics of Plasmas*, vol. 21, no. 6, 2014.
- [48] O. Ohia, J. Egedal, V. S. Lukin, W. Daughton, and A. Le, "Scaling laws for magnetic reconnection, set by regulation of the electron pressure anisotropy to the firehose threshold," *Geophy. Res. Lett.*, vol. 42, no. 24, 12 2015.

- C. Pollock, T. Moore, A. Jacques, J. Burch, U. Gliese, Y. Saito, T. Omoto, L. Avanov, A. Barrie, V. Coffey, J. Dorelli, D. Gershman, B. Giles, T. Rosnack, C. Salo, S. Yokota, M. Adrian, C. Aoustin, C. Auletti, S. Aung, V. Bigio, N. Cao, M. Chandler, D. Chornav, K. Christian, G. Clark, G. Collinson, T. Corris, A. De Los Santos, R. Devlin, T. Diaz, T. Dickerson, C. Dickson, A. Diekmann, F. Diggs, C. Duncan, A. Figueroa-Vinas, C. Firman, M. Freeman, N. Galassi, K. Garcia, G. Goodhart, D. Guererro, J. Hageman, J. Hanley, E. Hemminger, M. Holland, M. Hutchins, T. James, W. Jones, S. Kreisler, J. Kujawski, V. Lavu, J. Lobell, E. LeCompte, A. Lukemire, E. MacDonald, A. Mariano, T. Mukai, K. Narayanan, Q. Nguyan, M. Onizuka, W. Paterson, S. Persyn, B. Piepgrass, F. Cheney, A. Rager, T. Raghuram, A. Ramil, L. Reichenthal, H. Rodriguez, J. Rouzaud, A. Rucker, Y. Saito, M. Samara, J. A. Sauvaud, D. Schuster, M. Shappirio, K. Shelton, D. Sher, D. Smith, K. Smith, S. Smith, D. Steinfeld, R. Szymkiewicz, K. Tanimoto, J. Taylor, C. Tucker, K. Tull, A. Uhl, J. Vloet, P. Walpole, S. Weidner, D. White, G. Winkert, P. S. Yeh, and M. Zeuch, "Fast Plasma Investigation for Magnetospheric Multiscale," Space Science *Reviews*, vol. 199, no. 1-4, pp. 331–406, 3 2016. [Online]. Available: http://dx.doi.org/10.1007/s11214-016-0245-4
- [50] R. B. Torbert, C. T. Russell, W. Magnes, R. E. Ergun, P. A. Lindqvist, O. LeContel, H. Vaith, J. Macri, S. Myers, D. Rau, J. Needell, B. King, M. Granoff, M. Chutter, I. Dors, G. Olsson, Y. V. Khotyaintsev, A. Eriksson, C. A. Kletzing, S. Bounds, B. Anderson, W. Baumjohann, M. Steller, K. Bromund, G. Le, R. Nakamura, R. J. Strangeway, H. K. Leinweber, S. Tucker, J. Westfall, D. Fischer, F. Plaschke, J. Porter, and K. Lappalainen, "The FIELDS Instrument Suite on MMS: Scientific Objectives, Measurements, and Data Products," Space Science Reviews, vol. 199, no. 1-4, pp. 105–135, 2016. [Online]. Available: http://dx.doi.org/10.1007/s11214-014-0109-8

- [51] D. T. Young, J. L. Burch, R. G. Gomez, A. De Los Santos, G. P. Miller, P. Wilson, N. Paschalidis, S. A. Fuselier, K. Pickens, E. Hertzberg, C. J. Pollock, J. Scherrer, P. B. Wood, E. T. Donald, D. Aaron, J. Furman, D. George, R. S. Gurnee, R. S. Hourani, A. Jacques, T. Johnson, T. Orr, K. S. Pan, S. Persyn, S. Pope, J. Roberts, M. R. Stokes, K. J. Trattner, and J. M. Webster, "Hot Plasma Composition Analyzer for the Magnetospheric Multiscale Mission," *Space Science Reviews*, vol. 199, no. 1-4, pp. 407–470, 2016. [Online]. Available: http://dx.doi.org/10.1007/s11214-014-0119-6
- [52] B. H. Mauk, J. B. Blake, D. N. Baker, J. H. Clemmons, G. D. Reeves, H. E. Spence, S. E. Jaskulek, C. E. Schlemm, L. E. Brown, S. A. Cooper, J. V. Craft, J. F. Fennell, R. S. Gurnee, C. M. Hammock, J. R. Hayes, P. A. Hill, G. C. Ho, J. C. Hutcheson, A. D. Jacques, S. Kerem, D. G. Mitchell, K. S. Nelson, N. P. Paschalidis, E. Rossano, M. R. Stokes, and J. H. Westlake, "The Energetic Particle Detector (EPD) Investigation and the Energetic Ion Spectrometer (EIS) for the Magnetospheric Multiscale (MMS) Mission," Space Science Reviews, vol. 199, no. 1-4, pp. 471–514, 2016.
- [53] J. M. Webster, J. L. Burch, P. H. Reiff, A. G. Daou, K. J. Genestreti, D. B. Graham, R. B. Torbert, R. E. Ergun, S. Y. Sazykin, A. Marshall, R. C. Allen, L. J. Chen, S. Wang, T. D. Phan, B. L. Giles, T. E. Moore, S. A. Fuselier, G. Cozzani, C. T. Russell, S. Eriksson, A. C. Rager, J. M. Broll, K. Goodrich, and F. Wilder, "Magnetospheric Multiscale Dayside Reconnection Electron Diffusion Region Events," *Journal of Geophysical Research: Space Physics*, vol. 123, no. 6, pp. 4858–4878, 2018.

- [54] J. L. Burch, R. B. Torbert, T. D. Phan, L.-J. J. Chen, T. E. Moore, R. E. Ergun, J. P. Eastwood, D. J. Gershman, P. A. Cassak, M. R. Argall, S. Wang, M. Hesse, C. J. Pollock, B. L. Giles, R. Nakamura, B. H. Mauk, S. A. Fuselier, C. T. Russell, R. J. Strangeway, J. F. Drake, M. A. Shay, Y. V. Khotyaintsev, P. A. Lindqvist, G. Marklund, F. D. Wilder, D. T. Young, K. Torkar, J. Goldstein, J. C. Dorelli, L. A. Avanov, M. Oka, D. N. Baker, A. N. Jaynes, K. A. Goodrich, I. J. Cohen, D. L. Turner, J. F. Fennell, J. B. Blake, J. Clemmons, M. Goldman, D. Newman, S. M. Petrinec, K. J. Trattner, B. Lavraud, P. H. Reiff, W. Baumjohann, W. Magnes, M. Steller, W. Lewis, Y. Saito, V. Coffey, and M. Chandler, "Electron-scale measurements of magnetic reconnection in space," Science, vol. 352, no. 6290, 6 2016.
- [55] J. Egedal, A. Le, W. Daughton, B. Wetherton, P. A. Cassak, L. J. Chen, B. Lavraud, R. B. Torbert, J. Dorelli, D. J. Gershman, and L. A. Avanov, "Spacecraft Observations and Analytic Theory of Crescent-Shaped Electron Distributions in Asymmetric Magnetic Reconnection," *Physical Review Letters*, vol. 117, no. 18, 2016.
- [56] R. B. Torbert, J. L. Burch, B. L. Giles, D. Gershman, C. J. Pollock, J. Dorelli, L. Avanov, M. R. Argall, J. Shuster, R. J. Strangeway, C. T. Russell, R. E. Ergun, F. D. Wilder, K. Goodrich, H. A. Faith, C. J. Farrugia, P. A. Lindqvist, T. Phan, Y. Khotyaintsev, T. E. Moore, G. Marklund, W. Daughton, W. Magnes, C. A. Kletzing, and S. Bounds, "Estimates of terms in Ohm's law during an encounter with an electron diffusion region," *Geophysical Research Letters*, 2016.
- [57] F. D. Wilder, R. E. Ergun, S. Eriksson, T. D. Phan, J. L. Burch, N. Ahmadi, K. A. Goodrich, D. L. Newman, K. J. Trattner, R. B. Torbert, B. L. Giles, R. J. Strangeway, W. Magnes, P. A. Lindqvist, and Y. V. Khotyaintsev, "Multipoint Measurements of the Electron Jet of Symmetric Magnetic Reconnection with a Moderate Guide Field," *Physical Review Letters*, vol. 118, no. 26, pp. 1–5, 2017.

- [58] R. Bandyopadhyay, A. Chasapis, R. Chhiber, T. N. Parashar, B. A. Maruca, W. H. Matthaeus, S. J. Schwartz, S. Eriksson, O. Le Contel, H. Breuillard, J. L. Burch, T. E. Moore, C. J. Pollock, B. L. Giles, W. R. Paterson, J. Dorelli, D. J. Gershman, R. B. Torbert, C. T. Russell, and R. J. Strangeway, "Solar Wind Turbulence Studies Using MMS Fast Plasma Investigation Data," *The Astrophysical Journal*, vol. 866, no. 2, p. 81, 2018. [Online]. Available: http://dx.doi.org/10.3847/1538-4357/aade93
- [59] Y. Narita, R. Nakamura, W. Baumjohann, K.-H. Glassmeier, U. Motschmann, B. Giles, W. Magnes, D. Fischer, R. B. Torbert, C. T. Russell, R. J. Strangeway, J. L. Burch, Y. Nariyuki, S. Saito, and S. P. Gary, "on Electron-Scale Whistler Turbulence in the Solar Wind," *The Astrophysical Journal*, vol. 827, no. 1, p. L8, 2016. [Online]. Available: http://dx.doi.org/10.3847/2041-8205/827/1/L8
- [60] L. J. Chen, S. Wang, L. B. Wilson, S. Schwartz, N. Bessho, T. Moore, D. Gershman, B. Giles, D. Malaspina, F. D. Wilder, R. E. Ergun, M. Hesse, H. Lai, C. Russell, R. Strangeway, R. B. Torbert, F. A. Vinas, J. Burch, S. Lee, C. Pollock, J. Dorelli, W. Paterson, N. Ahmadi, K. Goodrich, B. Lavraud, O. Le Contel, Y. V. Khotyaintsev, P. A. Lindqvist, S. Boardsen, H. Wei, A. Le, and L. Avanov, "Electron Bulk Acceleration and Thermalization at Earth's Quasiperpendicular Bow Shock," *Physical Review Letters*, vol. 120, no. 22, p. 225101, 2018. [Online]. Available: https://doi.org/10.1103/PhysRevLett.120.225101
- [61] M. Hoshino, T. Mukai, T. Terasawa, and I. Shinohara, "Suprathermal electron acceleration in magnetic reconnection," *J. Geophys. Res.*, vol. 106, no. A11, pp. 25 979–25 997, 11 2001.
- [62] J. F. Drake, M. Swisdak, H. Che, and M. A. Shay, "Electron acceleration from contracting magnetic islands during reconnection," *Nature*, vol. 443, no. 5, pp. 553–556, 2006.
- [63] P. Montag, J. Egedal, E. Lichko, and B. Wetherton, "Impact of compressibility and a guide field on Fermi acceleration during magnetic island coalescence," *Physics of Plasmas*, vol. 24, no. 062906 (2017);, 2017. [Online]. Available: http://dx.doi.org/10.1063/1. 4985302http://aip.scitation.org/toc/php/24/6

- [64] A. Zeiler, D. Biskamp, J. F. Drake, B. N. Rogers, M. A. Shay, and M. Scholer, "Three-dimensional particle simulations of collisionless magnetic reconnection," *J. Geophys. Res.*, vol. 107, no. A9, 9 2002.
- [65] W. Daughton, J. Scudder, and H. Karimabadi, "Fully kinetic simulations of undriven magnetic reconnection with open boundary conditions," *Phys. Plasmas*, vol. 13, no. 7, p. 72101, 7 2006.
- [66] K. J. Bowers, B. J. Albright, L. Yin, W. Daughton, V. Roytershteyn, B. Bergen, and T. J. T. Kwan, "Advances in petascale kinetic plasma simulation with VPIC and Roadrunner," *Journal of Physics: Conference Series*, vol. 180, no. 1, p. 012055 (10 pp.), 2009.
- [67] G. W. Hammett and F. W. Perkins, "Fluid moment models for Landau damping with application to the ion-temperature-gradient instability," *Physical Review Letters*, vol. 64, no. 25, pp. 3019–3022, 1990.
- [68] G. W. Hammett, W. Dorland, and F. W. Perkins, "Fluid models of phase mixing, landau damping, and nonlinear gyrokinetic dynamics," *Physics of Fluids B*, vol. 4, no. 7, pp. 2052–2061, 1992.
- [69] P. B. Snyder, G. W. Hammett, and W. Dorland, "Landau fluid models of collisionless magnetohydrodynamics," *Physics of Plasmas*, vol. 4, no. 11, pp. 3974–3985, 1997.
- [70] P. B. Snyder and G. W. Hammett, "A Landau fluid model for electromagnetic plasma microturbulence," *Physics of Plasmas*, vol. 8, no. 7, pp. 3199–3216, 2001.
- [71] E. D. Held, J. D. Callen, C. C. Hegna, C. R. Sovinec, T. A. Gianakon, and S. E. Kruger, "Nonlocal closures for plasma fluid simulations," *Physics of Plasmas*, vol. 11, no. 5, 2004.
- [72] Y. Sarazin, G. Dif-Pradalier, D. Zarzoso, X. Garbet, P. Ghendrih, and V. Grandgirard, "Entropy production and collisionless fluid closure," *Plasma Physics and Controlled Fusion*, vol. 51, no. 115003, 2009.
- [73] M. Perin, C. Chandre, P. J. Morrison, and E. Tassi, "Hamiltonian closures for fluid models with four moments by dimensional analysis," 2015.

- [74] C. C. Hegna and J. D. Callen, "A closure scheme for modeling rf modifications to the fluid equations," *Physics of Plasmas*, vol. 16, no. 112501, 2009.
- [75] T. Chust and G. Belmont, "Closure of fluid equations in collisionless magnetoplasmas," *Physics of Plasmas*, vol. 13, no. 012506, 2006.
- [76] L. Wang, A. H. Hakim, A. Bhattacharjee, and K. Germaschewski, "Comparison of multi-fluid moment models with particle-in-cell simulations of collisionless magnetic reconnection," *Physics of Plasmas*, vol. 22, no. 012108, 2015.
- [77] J. Ng, A. Hakim, A. Bhattacharjee, A. Stanier, and W. Daughton, "Simulations of anti-parallel reconnection using a nonlocal heat flux closure," *Physics of Plasmas*, vol. 24, no. 082112, 2017.
- [78] M. M. Kuznetsova, M. Hesse, and D. Winske, "Kinetic quasi-viscous and bulk flow inertia effects in collisionless magnetotail reconnection," *Journal of Geophysical Research: Space Physics*, vol. 103, no. A1, pp. 199–213, 1998.
- [79] S. I. Braginskii, "Transport Processes in a Plasma," in *Review of Plasma Physics*, M. A. Leontovich, Ed. Consultants Bureau, New York, 1965, vol. 1, ch. 3, pp. 205–311.
- [80] M. Øieroset, T. D. Phan, C. Haggerty, M. A. Shay, J. P. Eastwood, D. J. Gershman, J. F. Drake, M. Fujimoto, R. E. Ergun, F. S. Mozer, M. Oka, R. B. Torbert, J. L. Burch, S. Wang, L. J. Chen, M. Swisdak, C. Pollock, J. C. Dorelli, S. A. Fuselier, B. Lavraud, B. L. Giles, T. E. Moore, Y. Saito, L. A. Avanov, W. Paterson, R. J. Strangeway, C. T. Russell, Y. Khotyaintsev, P. A. Lindqvist, and K. Malakit, "MMS observations of large guide field symmetric reconnection between colliding reconnection jets at the center of a magnetic flux rope at the magnetopause," *Geophysical Research Letters*, vol. 43, no. 11, pp. 5536–5544, 2016.
- [81] J. Egedal, W. Fox, N. Katz, M. Porkolab, K. Reim, and E. Zhang, "Laboratory observations of spontaneous magnetic reconnection," *Phys. Rev. Lett.*, vol. 98, no. 015003, 1 2007.

- [82] A. Le, J. Egedal, and W. Daughton, "Two-stage bulk electron heating in the diffusion region of anti-parallel symmetric reconnection," *Physics of Plasmas*, vol. 23, no. 10, 2016.
- [83] A. Le, J. Egedal, W. Fox, N. Katz, A. Vrublevskis, W. Daughton, and J. F. Drake, "Equations of state in collisionless magnetic reconnection," *Physics of Plasmas*, vol. 17, no. 055703, p. 55703, 5 2010.
- [84] B. A. Wetherton, J. Egedal, A. Lê, and W. Daughton, "Validation of Anisotropic Electron Fluid Closure Through In Situ Spacecraft Observations of Magnetic Reconnection," Geophysical Research Letters, no. May, pp. 1–7, 2019.
- [85] S. Masuda, T. Kosugi, H. Hara, and Y. Ogawaray, "A loop top hard X-reay source i a compact solar-flare as evidence for magnetic reconnection," *Nature*, vol. 371, no. 6497, pp. 495–497, 10 1994.
- [86] T. Nagai, M. Fujimoto, Y. Saito, S. Machida, T. Terasawa, R. Nakamura, T. Yamamoto, T. Mukai, A. Nishida, and S. Kokubun, "Structure and dynamics of magnetic reconnection for substorm onsets with Geotail observations," *Journal of Geophysical Research: Space Physics*, vol. 103, no. 97, pp. 4419–4440, 1998.
- [87] T. D. Phan and G. Paschmann, "Low-latitude dayside magnetopause and boundary layer for high magnetic shear .1. Structure and motion," *J. Geophys. Res.*, vol. 101, no. A4, pp. 7801–7815, 4 1996.
- [88] H. C. Ku and D. G. Sibeck, "Internal structure of flux transfer events produced by the onset of merging at a single X line," *J. Geophys. Res.*, vol. 102, no. A2, pp. 2243–2260, 2 1997.
- [89] M. A. Shay, C. C. Haggerty, T. D. Phan, J. F. Drake, P. A. Cassak, P. Wu, M. Oieroset, M. Swisdak, and K. Malakit, "Electron heating during magnetic reconnection: A simulation scaling study," *Physics* of *Plasmas*, vol. 21, no. 12, 2014.
- [90] A. Ishizawa, R. Horiuchi, and H. Ohtani, "Two-scale structure of the current layer controlled by meandering motion during steady-state collisionless driven reconnection," *Physics of Plasmas*, vol. 11, no. 7, pp. 3579–3585, 2004.

- [91] R. Horiuchi and H. Ohtani, "Formation of non-Maxwellian distribution and its role in collisionless driven reconnection," *Communications in Computational Physics*, vol. 4, no. 3, pp. 496–505, 2008.
- [92] J. Egedal, M. Øieroset, W. Fox, and R. P. Lin, "In situ discovery of an electrostatic potential, trapping electrons and mediating fast reconnection in the earth's magnetotail," *Physical Review Letters*, vol. 94, no. 2, pp. 1–4, 1 2005.
- [93] J. Egedal, W. Fox, N. Katz, M. Porkolab, M. Øieroset, R. P. Lin, W. Daughton, and D. J. F., "Evidence and Theory for Trapped Electrons in Guide Field Magnetotail Reconnection," J. Geophys. Res., vol. 113, no. 6, p. A12207, 3 2008.
- [94] L. J. Chen, N. Bessho, B. Lefebvre, H. Vaith, A. Fazakerley, A. Bhattacharjee, P. A. Puhl-Quinn, A. Runov, Y. Khotyaintsev, A. Vaivads, E. Georgescu, and R. Torbert, "Evidence of an extended electron current sheet and its neighboring magnetic island during magnetotail reconnection," *J. Geophys. Res.*, vol. 113, no. A12, 12 2008.
- [95] J. Egedal, W. Daughton, A. Le, and A. L. Borg, "Double layer electric fields aiding the production of energetic flat-top distributions and superthermal electrons within magnetic reconnection exhausts," *Physics of Plasmas*, vol. 22, 2015.
- [96] D. B. Graham, Y. V. Khotyaintsev, C. Norgren, A. Vaivads, M. André, P. A. Lindqvist, G. T. Marklund, R. E. Ergun, W. R. Paterson, D. J. Gershman, B. L. Giles, C. J. Pollock, J. C. Dorelli, L. A. Avanov, B. Lavraud, Y. Saito, W. Magnes, C. T. Russell, R. J. Strangeway, R. B. Torbert, and J. L. Burch, "Electron currents and heating in the ion diffusion region of asymmetric reconnection," *Geophysical Research Letters*, vol. 43, no. 10, pp. 4691–4700, 2016. [Online]. Available: http://dx.doi.org/10.1002/2016GL068613

- [97] J. P. Eastwood, R. Mistry, T. D. Phan, S. J. Schwartz, R. E. Ergun, J. F. Drake, M. Øieroset, J. E. Stawarz, M. V. Goldman, C. Haggerty, M. A. Shay, J. L. Burch, D. J. Gershman, B. L. Giles, P. A. Lindqvist, R. B. Torbert, R. J. Strangeway, and C. T. Russell, "Guide field reconnection: exhaust structure and heating," Geophysical Research Letters, vol. 45, pp. 1–9, 2018. [Online]. Available: http://doi.wiley.com/10.1029/2018GL077670
- [98] Y. E. Litvinenko, "Particle acceleration in reconnecting current sheets with a nonzero magnetic field," *Astrophys. J.*, vol. 462, no. 2, Part 1, pp. 997–1004, 5 1996.
- [99] P. K. Browning and G. E. Vekstein, "Particle acceleration at an X-type reconnection site with a parallel magnetic field," *J. Geophys. Res.*, vol. 106, no. A9, pp. 18 677–18 692, 9 2001.
- [100] R. G. Kleva, J. F. Drake, and F. L. Waelbroeck, "Fast reconnection in high-temperature plasmas," *Phys. Plasmas*, vol. 2, no. 1, pp. 23–34, 1 1995.
- [101] J. Egedal, W. Daughton, J. F. Drake, N. Katz, and A. Le, "Formation of a localized acceleration potential during magnetic reconnection with a guide field," *Phys. Plasmas*, vol. 16, no. 5, 5 2009.
- [102] W. Fox, F. Sciortino, V. A. Stechow, J. Jara-Almonte, J. Yoo, H. Ji, and M. Yamada, "Experimental Verification of the Role of Electron Pressure in Fast Magnetic Reconnection with a Guide Field," *Physical Review Letters*, vol. 118, no. 12, pp. 1–5, 2017.
- [103] B. N. Rogers, R. E. Denton, J. F. Drake, and M. A. Shay, "Role of dispersive waves in collisionless magnetic reconnection," *Phys. Rev. Lett.*, vol. 8719, no. 19, p. 195004, 11 2001.
- [104] M. Øieroset, T. D. Phan, J. F. Drake, J. P. Eastwood, S. A. Fuselier, R. J. Strangeway, C. Haggerty, M. A. Shay, M. Oka, S. Wang, L. J. Chen, I. Kacem, B. Lavraud, V. Angelopoulos, J. L. Burch, R. B. Torbert, R. E. Ergun, Y. Khotyaintsev, P. A. Lindqvist, D. J. Gershman, B. L. Giles, C. Pollock, T. E. Moore, C. T. Russell, Y. Saito, L. A. Avanov, and W. Paterson, "Reconnection With Magnetic Flux Pileup at the Interface of Converging Jets at the Magnetopause," *Geophysical Research Letters*, vol. 46, no. 4, pp. 1937–1946, 2019.

- [105] J. Egedal, A. Le, P. L. Pritchett, and W. Daughton, "Electron dynamics in two-dimensional asymmetric anti-parallel reconnection," *Phys. Plasmas*, vol. 18, no. 10, 10 2011.
- [106] J. Yoo, S. Wang, E. Yerger, J. Jara-Almonte, H. Ji, M. Yamada, L. J. Chen, W. Fox, A. Goodman, and A. Alt, "Whistler wave generation by electron temperature anisotropy during magnetic reconnection at the magnetopause," *Physics of Plasmas*, vol. 26, no. 5, pp. 1–10, 2019.
- [107] M. W. Dunlop, D. J. Southwood, K. H. Glassmeier, and F. M. Neubauer, "Analysis of multipoint magnetometer data," *Advances in Space Research*, vol. 8, no. 9-10, pp. 273–277, 1988.
- [108] G. Chanteur and C. C. Harvey, "Spatial Interpolation for Four Space-craft: Application to Magnetic Gradients," *ISSI Scientific Reports Series*, vol. 1, pp. 371–394, 1998.
- [109] J. D. Scudder and W. S. Daughton, "Illuminating electron diffusion regions of collisionless magnetic reconnection using electron agyrotropy," *Journal of Geophysical Research: Space Physics*, vol. 113, no. 6, pp. 1–16, 2008.
- [110] N. Aunai, M. Hesse, and M. Kuznetsova, "Electron nongyrotropy in the context of collisionless magnetic reconnection," *Physics of Plasmas*, vol. 20, no. 9, 2013.
- [111] M. Swisdak, "Quantifying gyrotropy in magnetic reconnection," *Geophysical Research Letters*, vol. 43, no. 1, pp. 43–49, 2016.
- [112] J. D. Scudder, R. D. Holdaway, W. S. Daughton, H. Karimabadi, V. Roytershteyn, C. T. Russell, and J. Y. Lopez, "First resolved observations of the demagnetized electron-diffusion region of an astrophysical magnetic-reconnection site," *Physical Review Letters*, vol. 108, no. 22, pp. 1–5, 2012.
- [113] J. D. Scudder, H. Karimabadi, W. Daughton, and V. Roytershteyn, "Frozen flux violation, electron demagnetization and magnetic reconnection," *Physics of Plasmas*, vol. 22, no. 10, 2015. [Online]. Available: http://dx.doi.org/10.1063/1.4932332

- [114] R. D. Hazeltine and J. D. Meiss, *Plasma Confinement*. Addison-Wesley, 1992.
- [115] V. Roytershteyn, W. Daughton, H. Karimabadi, and F. S. Mozer, "Influence of the lower-hybrid drift instability on magnetic reconnection in asymmetric configurations," *Phys. Rev. Lett.*, vol. 108, no. 18, p. 185001, 2012.
- [116] P. K. Montag, "Modeling the Formation of Current Sheets in Symmetric and Asymmetric Reconnection," Ph.D. dissertation, Massachusetts Institute of Technology, 2018.
- [117] B. A. Wetherton, J. Egedal, P. K. Montag, A. Lê, and W. S. Daughton, "A Drift-Kinetic Method for Obtaining Gradients in Plasma Properties From Single-Point Distribution Function Data," *Journal of Geophysical Research : Space Physics*, vol. 125, no. 8, pp. 1–10, 2020.
- [118] B. U. Ã. Sonnerup and L. J. Cahill, "Magnetopause structure and attitude from Explorer 12 observations," *Journal of Geophysical Research*, vol. 72, no. 1, p. 171, 1967.
- [119] B. U. Ã. Sonnerup and M. Scheible, "Minimum and maximum variance analysis," *Analysis methods for multi-spacecraft data*, vol. 001, pp. 185–220, 1998. [Online]. Available: http://www.issibern.ch/forads/sr-001-08.pdf%0Ahttp://ankaa.unibe.ch/forads/sr-001-08.pdf
- [120] R. E. Denton, B. U. A. Sonnerup, C. T. Russell, H. Hasegawa, T. D. Phan, R. J. Strangeway, B. L. Giles, R. E. Ergun, P. A. Lindqvist, R. B. Torbert, J. L. Burch, and S. K. Vines, "Determining L-M-N Current Sheet Coordinates at the Magnetopause From Magnetospheric Multiscale Data," *Journal of Geophysical Research: Space Physics*, vol. 123, no. 3, pp. 2274–2295, 2018. [Online]. Available: http://doi.wiley.com/10.1002/2017JA024619